The Importance of Controlling Composition to Tailor the Properties of Magnetic Thin Films

ANDREAS FRISK

Dissertation presented at Uppsala University to be publicly examined in Polhemsalen, Ångströmlaboratoriet, Lägerhyddsvägen 1, Uppsala, Friday, 9 December 2016 at 09:15 for the degree of Doctor of Philosophy. The examination will be conducted in English. Faculty examiner: Professor Sarah Thompson (University of York, Department of Physics).

Abstract
Frisk, A. 2016. The Importance of Controlling Composition to Tailor the Properties of Magnetic Thin Films. *Digital Comprehensive Summaries of Uppsala Dissertations from the Faculty of Science and Technology* 1445. 126 pp. Uppsala: Acta Universitatis Upsaliensis. ISBN 978-91-554-9735-4.

Many physical properties, for example structural or magnetic, of a material are directly dependent on elemental composition. Tailoring of properties through highly accurate composition control is possible in thin films. This work exemplifies such tailoring.

A short review is given of the current status for research in the area of permanent magnets, focusing on rare earth element free alternatives, where FeNi in the $L1_0$ phase is a possible candidate. Epitaxial FeNi $L1_0$ thin films were successfully synthesized by magnetron sputtering deposition of monoatomic layers of Fe and Ni on HF-etched Si(001) substrates with Cu or $Cu_{100-x}Ni_x$/Cu buffers. The in-plane lattice parameter a_{CuNi} of the $Cu_{100-x}Ni_x$ buffer layer was tuned by the Ni content. Through matching of a_{FeNi} to a_{CuNi}, the strain state $(c/a)_{FeNi}$ was controlled, where c is the out-of-plane lattice parameter. The 001 reflection indicative of chemical order, as measured by resonant x-ray diffraction, was in most cases split in two peaks due to a composition modulation of Fe and Ni. This chemical disorder contributed to that the uniaxial magnetocrystalline anisotropy energy, $K_U \approx 0.35$ MJ/m^3, was smaller than predicted. In later experiments the composition modulation could partly be compensated for. Remaining discrepancies with respect to predicted K_U values were attributed to additional disorder induced by surface roughness of the buffer layer.

The interface sharpness between Fe and Ni was explored by producing epitaxial symmetric multilayers with individual layer thicknesses $n = 4\text{-}48$ monolayers (ML). For n ≤ 8 ML the films had pure fcc structure, with antiferromagnetic Fe layers. For n ≥ 8 ML the Fe layers relaxed to bcc structure.

A combinatorial sputter chamber, which has the capability to deposit samples with composition and thickness gradients, was assembled. A model for simulation of composition and thickness across large substrates, for the conditions in this chamber, is presented. The model is verified by comparison to experimental data. Some challenges inherent in combinatorial sputtering are discussed, and two experimental studies employing the technique are presented as examples. These investigated magnetic and structural properties of Tb-Co films, with 7-95 at.% Tb, and of amorphous and crystalline ternary gradient Co-Fe-Zr films, respectively.

Keywords: FeNi, $L1_0$, X-ray diffraction, magnetic anisotropy, magnetron sputtering, thin film, permanent magnets, combinatorial materials science, amorphous materials, magnetic properties of thin films, chemical order

Andreas Frisk, Department of Physics and Astronomy, Materials Physics, 516, Uppsala University, SE-751 20 Uppsala, Sweden.

Till morfar för att du uppmuntrade min nyfikenhet

List of papers

This thesis is based on the following papers, which are referred to in the text by their Roman numerals.

I **Resonant x-ray diffraction revealing chemical disorder in sputtered L1$_0$ FeNi on Si(001)**
Andreas Frisk, Bengt Lindgren, Spiridon D Pappas, Erik Johansson and Gabriella Andersson
Journal of Physics: Condensed Matter, **28**, 406002, 2016

II **Strain Engineering for Controlled Growth of Thin-Film FeNi L1$_0$**
Andreas Frisk, Thomas P.A. Hase, Erik Johansson, Peter Svedlindh and Gabriella Andersson
Submitted manuscript

III **Composition, structure and magnetic properties of very thin sputtered Fe/Ni multilayers deposited on epitaxial Cu/Si(001)**
Andreas Frisk, Hasan Ali, Peter Svedlindh, Klaus Leifer, Gabriella Andersson and Tomas Nyberg
Manuscript, (October 30, 2016)

IV **Tailoring anisotropy and domain structure in amorphous TbCo thin films through combinatorial methods**
Andreas Frisk, Fridrik Magnus, Sebastian George, Unnar B Arnalds and Gabriella Andersson
Journal of Physics D: Applied Physics, **49**, 035005, 2016

V **Magnetic and structural characterization of CoFeZr thin films grown by combinatorial sputtering**
Andreas Frisk, Martina Ahlberg, Giuseppe Muscas, Sebastian George, Robert Johansson, Wantana Klysubun, Petra Jönsson and Gabriella Andersson
Manuscript, (October 28, 2016)

Reprints were made with permission from the publishers.

My contributions to the papers

    I. Did all the growth, characterization, analysis and writing. Others have contributed with discussion, ideas and helped with the beamtime measurements.

    II. Did all the growth, analysis and much of the writing. Did all characterization, except for SQUID measurements.

    III. Did all growth and XRD measurements, all analysis of XRD, XPS and magnetic data. Participated in XPS measurements, did the writing.

    IV. Did all growth. Performed all RBS, XRD and VSM measurements and analysis. Did large parts of the writing.

    V. Did all growth. Performed all RBS and XRD measurements and analysis, did most of the MOKE measurements. Did part of the writing.

Papers not included in this thesis

- **Polymeric Smart Coating Strategy for Titanium Implants**
  Ida Berts, Dmitri Ossipov, Giovanna Fragneto, **Andreas Frisk**, Adrian R. Rennie
  Advanced Engineering Materials, **16**, 11, 1340–1350, 2014

- **Synthesis and mechanical properties of Fe-Nb-B thin-film metallic glasses**
  J.H. Yao, C. Hostert, D. Music, **A. Frisk**, M. Björck, J.M. Schneider
  Scripta Materialia, **67**, 2, 181–184, 2012

Contents

1. Introduction

In the age of anthropocene, where humanity must battle climate change caused by itself, clean energy, meaning energy produced from renewable sources, is of utmost importance. The cleanest and most efficient way, that we know of today, to distribute and use energy is in the form of electricity. That is why we are forced to move towards an even more electrified society compared with today's, with the consequence that the utilization of electrical machines will definitely grow in the future. When converting mechanical energy into electrical energy, and back, generators and electrical motors are the machines to use. Therefore the efficiency of these machines, both in terms of usage but also in terms of required resources for manufacturing are very important. In these machines the connection from mechanical force to electricity is through a magnetic field. Traditionally, these magnetic fields have been produced through induction in coils. There are two main problems with this solution: first, the machines become large both in the measure of volume but also in mass and the second is that they can not produce much torque. A way of solving this is to produce the magnetic field by permanent magnets (PM). Although the mass of a PM machine is smaller compared to induction machines, the delivered/generated power per mass is still a parameter which is favourable to maximize. Two good examples of this are electric vehicles and wind power generation. An electric car, be it a hybrid or a fully electric model, will have heavy batteries. Minimizing the total mass is important for the car to be energy efficient but also to have a long range. For wind power plants the obvious thing is that the lighter the generator at the top of the power plant is, the easier it will be to design, install etcetera. But also, especially for offshore power plants, a PM based generator can be made gear-less, which apart from decreasing the weight, also requires less maintenance, which of course is difficult to perform offshore.

The highest (per mass) performing permanent magnetic materials (PMM) of today are iron-neodymium-boron (Fe-Nd-B) and samarium-cobalt (Sm-Co) based. To increase the properties of FeNdB at higher temperatures it is usually doped with dysprosium (Dy) or terbium (Tb). Nd, Sm, Dy and Tb are rare earth elements (REE). REEPM motors and generators have much better performance compared to both induction and ferrite based PM versions, both when it comes to torque but also in delivered/generated power per mass [1]. These REEs are therefore very important from a technological, economical and also an environmental point of view. Before going into the physics of this thesis work, I will discuss REE in those terms in the next section.

1.1 Geopolitics

Even though REEs are very common in the Earth's crust they are very diluted and mining them is therefore usually not profitable. Instead, they are often extracted as by-products when mining something else, e.g. Fe. [2, 3] There are not many mines in the world where they appear in such high concentrations that extraction is motivated. Most of these mines are located in China, which some some say China has taken advantage of to gain political influence. Already in 1992, Deng Xiaoping said "There is oil in the Middle East and rare earths in China" [4]. Another concern with the REE mining is their by-products. Monazite, one of the minerals containing REEs, is often found together with e.g. Thorium which is radioactive. This makes the actual mining difficult and it also causes pollution of the environment. These by-products must be deposited somewhere, and the resulting piles will be enriched with toxic and radioactive materials. If the deposition piles are not contained properly the toxics can be released into the surroundings [2, 5]. Up till the 1990s the dominating mine for REEs was MolyCorp's Mountain Pass mine in the US [3], but due to the costs of abiding by environmental legislation, it became less profitable. Simultaneously, many Chinese mines opened which sold the minerals very cheap. The effect was that non-Chinese mines, including the Mountain Pass mine, could not compete and had to close down. The secondary consequence was that basically all REEs were supplied from China [3]. A third consequence was that REEs became very cheap, which made people at this time ignorant about their criticality. But these events took place at the same time as the demand for REEs increased, as the development in electronics and other high-tech products required more and more REEs. Also the switch to more sustainable energy generation and transports, to counter the global warming, increased (and still continues to increase) the demand for strong PMs [1]. Eventually, the Chinese government wanted to control the inner market for REEs and the environmental pollution had become a problem they could not ignore. To better control the market and secure enough domestic supply, e.g. to be able to fulfil their plans of wind power generator production, in 2005 they imposed export quotas on REEs, which were subsequently decreased year by year.

These paths of development came to a clash in 2011. The decreased export quotas and the high demand made the prices skyrocket, e.g. the price for Dy outside of China increased by 4900 % [5], see fig. 1.1. For Japan the restriction in imports was devastating since they are a big producer of REE-containing electronics, but have no domestic supply of REEs. The consequences of these export restrictions were that governments and also companies of western countries, including Japan, realized their dependence on the Chinese government. An example of government concern was that some military equipment contains REEs, e.g. guidance systems for missiles [4], and a dependence in the production of this equipment could be problematic in case of an armed con-

flict. The issue can also be explained in a less political way, without taking part for any side: when it comes to companies, the problematics can be viewed strictly as a cost issue, see fig. 1.1. A company wants the prices on raw materials to not only be cheap but also predictable and stable, and they want to know that there is enough supply so they can continue their business undisturbed. Even if the fact that 90 % of the REEs is supplied from China was not an issue, another non-political point which would be problematic is that the predicted need for REE-based electrical machines, due to the need for the transfer to sustainable energy is much larger than the total production of REEs today [5].
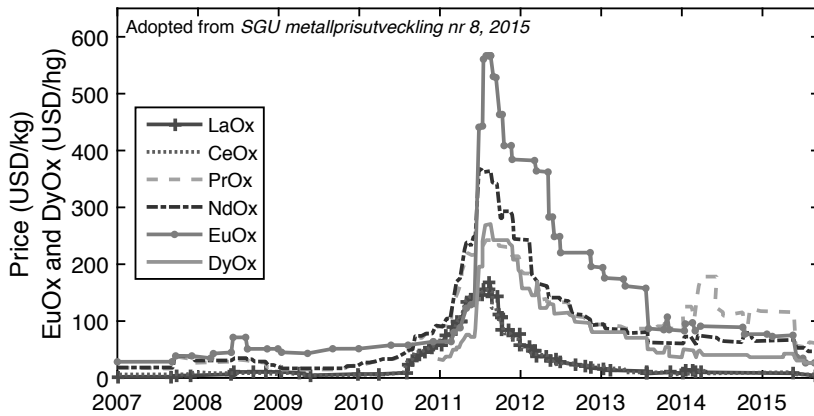
Figure 1.1. Price development of some relevant REE materials during 2007-2015. This plot shows the price fluctuations which triggered the interest for REE free PMMs. Values are from SGU metallprisutveckling nr 8 2015 [6].

These realizations and the price developments spurred many actions across the world. For example, after the crisis of 2011, it once again became profitable to open mines such as the Mountain Pass, and a feverish search for new mines and deposits was started all over the world. One of the responses from western governments was a complaint, concerning Chinas export quotas, filed to the world trade organization (WTO) in 2012. Eventually, WTO ruled against China and today (2016) they have adapted to this ruling and replaced the quotas with a licensing system [7]. Due to all these actions, such as new mines, increased production, more transparency of the Chinese REE market etcetera, the prices have decreased (see fig. 1.1) and they are now stabilized at levels just slightly above the prices before 2011. A good summary of the situation was given in the US Department of Energy's Critical Materials Reports from 2010 and 2011 [5, 8]. These reports did not only explain the current situation, but also predicted the future need of REEs and possible strategies to counter these needs. To handle the uncertainty in supply and the dependence on another state, one of the strategies was to start extensive research programs

to find new REE free materials. The same strategy was adopted not only in the US but also in Japan, EU and by different companies. These programs can roughly be divided into three categories.

Programs belonging to the first category try to decrease the need for the most scarce of the REEs, i.e. Dy and Tb. Can FeNdB be fabricated more efficiently so that smaller amounts are needed? Two main realizations about FeNdB are that the coercivity depends on the grain size, and that many of the properties depend on what happens at the grain boundaries. Therefore, research has focused on minimizing the grain size, with single-domain sized grains as the ideal. In addition trying to understand and perform grain boundary engineering has improved the properties. One example is that, instead of alloying the bulk magnet with Dy, it has been found that it is Dy in the grain boundaries that gives the enhanced properties at elevated temperatures. Thereby less Dy per volume of PMM is required if Dy is diffused along the grain boundaries after the bulk has been cracked into small grains.

The second category originates in the realization that the utilization of REEs is very skewed, e.g. from one unit of REE ore (typically the mineral Bastnäsite), approximately 55 % is Cerium (Ce), 30 % is Lantanum, and about 10 % is Nd. But Ce does not have any major area of application like Nd, meaning that there are large supplies of Ce, as a by-product of Nd mining [3]. Often REEs can be substituted for each other while still keeping similar properties. Why not use this surplus of Ce and e.g. substitute Nd for Ce? CeFeB has magnetic properties which are not as good as NdFeB but they are still better than the ferrites [9]. This and similar substituted materials with intermediate properties could be used for less demanding products and they would also be cheaper.

The third category concerns REE-free PMMs. The realization was soon made that finding a new PMM without REEs which possesses properties better than SmCo and FeNdB is very unlikely due to the magnetic nature of the 4f elements (all REEs except Y and Sc have 4f electrons) which have the strongest moments and anisotropies of all elements. But there is a gap in both performance and price between the ferrite based PMs and the REE PMs. This is apparent in fig. 4.1 where the ferrites are in the lower left corner while the REE PMs are in the upper right. If this gap could be filled, much could be gained both in terms of economy but also for the environment. Therefore a multitude of different new material systems and also some old have been studied in various research groups [10]. A selection will be presented briefly in chapter 4.

1.2 Scope of this thesis

This thesis is divided into two parts. Apart for using the same experimental techniques for deposition and analysis, the common factor between the two

parts is the importance of composition for the properties of the synthesized materials.

Part I originates in a research program initiated by ABB AB which falls into the third category presented above. The goal here was to assess the overall situation of PMM and to investigate one REE-free PM replacement material system in depth. The material system chosen was FeNi with the $L1_0$ structure, and the work has mostly concerned synthesis of this phase in thin film form. An important sub-part of this work has been to characterize this phase which is rather complicated and the main results concern the composition modulations we have measured. Papers I, II and III belong to this first Part.

Part II concerns combinatorial sputtering, and the building of a new sputter system, of which I was one of the main responsible persons. The combinatorial technique will be presented and discussed. A model to simulate composition gradients in deposited thin films will be given. Papers IV and V belong to this second part and concern studies of magnetic amorphous thin film materials which have been deposited with composition gradients. Amorphous materials have properties that can be rather different from crystalline materials, and opposite to the hard magnetic materials discussed in Part I they are often magnetically soft.

Sputtering was used for all experimental work in this thesis and since also some magnetic measurement techniques were common for both parts, these experimental techniques will be described first.

2. Sputtering

Pure thin film fabrication requires equipment that may be operated at ultra high vacuum (UHV) 7.5×10^{-10} to 7.5×10^{-13} torr ($=1 \times 10^{-7}$ to 1×10^{-10} Pa)[1] to minimize the amount of contamination. Thin film fabrication in such equipment usually relies on physical vapour deposition (PVD) techniques. Two examples of PVD are sputtering and evaporation. Sputtering is considered easier to use and more versatile compared to evaporation since it has more parameters to control the deposition process and a better ability to adjust the composition in the deposited film. Although the actual sputtering process is operated at medium vacuum conditions, (25 to 7.5×10^{-4} torr) the purity can be maintained in a UHV chamber by using pure sputtering gases. But still for purity reasons the sputtering gas pressure should be minimized if possible.

The basic process in sputtering is the ejection of atoms from a target material. This is accomplished by bombardment of the material with ions, which transfer their momentum and energy to the target atoms which may then be ejected if the transferred energy is larger than the binding energy of the target material. The ions are normally produced in a plasma. The sputter process is well studied and explained at length in several text books, see e.g. [11], so the description here will be simplified and does not try to be comprehensive. Practically sputtering is carried out in the following way. An inert non-reactive gas, usually Argon, is supplied to the vacuum chamber in a controlled manner while still pumping. The gas flow through the chamber must be large enough to increase the chamber pressure so that sputtering is facilitated. A negative voltage is applied at the target, which is then the cathode, and the anode is the rest of the chamber which is grounded. There is always a small amount of ions in the gas, which will be accelerated towards the target. When the ions collide with the target, secondary electrons are ejected. The electrons are accelerated away from the target and they may ionize neutral atoms through collisions. These new ions and electrons will also be accelerated in the electric field causing further collisions. If more than one ion is created for each original ion then a plasma or glow-discharge has been created. Once the plasma is created it is self sustaining if equal amounts of ions are created and consumed. The ions in the plasma will gain momentum and energy from the electric field and impinge on the target where they will eject target atoms if they transfer enough energy. The number of ejected target atoms per incident ion is referred

---

[1]By tradition in our group we have used torr in our sputter systems and I will continue to do so in this thesis.

to as the sputtering yield. The sputtered target atoms are neutral and will travel in a straight path until they collide with either the chamber wall or an Ar atom. If a substrate is placed in the path of these atoms they will impinge on the surface. If these adatoms do not have energy to evaporate they will stick to the substrate surface, and a film is deposited.
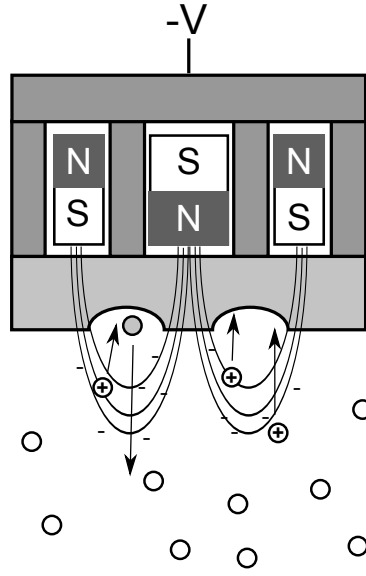
Figure 2.1. Schematic cross section of a magnetron. The negative voltage $-V$ is applied at the Cu cooling block which is in electric contact with the target. The uncoloured Ar atoms are ionized in the plasma and accelerated towards the target where they sputter atoms from the target. The race track is schematically shown as two grooves in the target. The plasma density is largest close to the race track.

The process just described is called direct current (DC) sputtering. It is also possible to perform radio-frequency (RF) sputtering where an alternating voltage is applied at the target. RF-sputtering is useful for non-conductive materials. For poor conductive materials pulsed-DC sputtering can be used, where the potential is applied in pulses which can help remove the negative charge build-up. It is also possible to perform reactive sputtering where reactive gases (O_2, N_2 etc) are introduced in the chamber together with the sputtering gas. This process is more complicated and will not be further described here since it has not been used. Only metallic targets were used in the work presented in this thesis, and therefore only DC magnetron sputtering was needed. Magnetron sputtering uses a magnetic field over the target surface, fig. 2.1. Due to the Lorentz force the electrons will travel in spirals close to the target surface, which increases the electron density here. The consequence is an increased ionization rate which facilitates a sustainable plasma at lower pressure and also gives higher deposition rates compared to normal DC-sputtering. The magnetic field is produced by magnets placed behind the target. The geome-

try is such that the stray field forms loops over the target surface, see fig. 2.1. The biggest drawback of magnetron sputtering is the poor target utilization. The sputtering will mainly take place where the plasma has the highest density which is where the stray field has largest flux and is parallel to the target surface. For the conventional geometry this will be along a circular path on the target. Along this path the erosion will be highest and it is usually referred to as the race-track, see figs. 2.1 and 2.2. A target will be consumed when the race-track depth equals the thickness. For targets of magnetic materials the penetration of the stray field will be diminished, they must therefore be very thin to be able to sustain the plasma at normal pressures. The targets will be heated by the sputtering process and to avoid melting and demagnetization of the magnets, water cooling is used. The entire unit of target, magnets, water cooling block, water and electrical connections is called a magnetron.
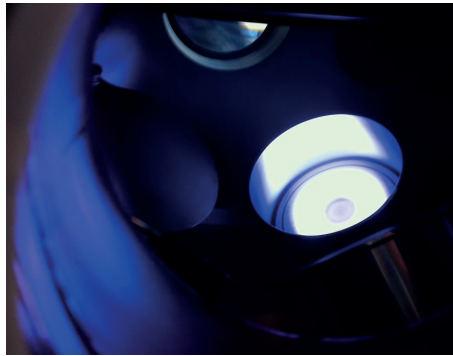
Figure 2.2. Image of a magnetron with the plasma ignited, where the donut shaped form of the plasma situated above the race track can be seen.

The deposition rate is dependent on several factors and it can be tuned. Lets first consider the sputter yield. The yield depends on the incident angle of the ion, the energy of the ion, the masses of the ion and target atoms and the surface binding energy of the target atoms. The yield can be simulated by e.g. the SRIM software [12, 13] and in the normal operation range (10 eV–1000 eV) for the materials discussed here it is monotonically increasing with energy. The incident ion energy is determined by the applied voltage by which the ions are accelerated. The flux of sputtered atoms will scale with the yield times the number of incident ions which is proportional to the current. In this voltage region the sputter erosion rate and thereby the deposition rate is considered to be linearly dependent on the delivered power which is the variable normally used for tuning the rate. Experimentally this linear relationship between power and deposition rate is normally observed and my calibrations using a proportionality factor and offset for each element and magnetron has always worked well.

The sputtered atoms will have a distribution of emission angles from the target normal. This means only a fraction of all atoms will impinge on the sub-

strate. The normal direction has the highest probability and the angular distribution has approximately a cosine dependence relative to the surface normal, $\cos\varphi$ [11]. For evaporation it has been found that a n:th power cosine distribution is a more accurate description if the flux is highly directed, see fig. 2.3. Such directionality is similar to beaming effects (entrance effects) when gas exits a tube in the molecular flow regime.
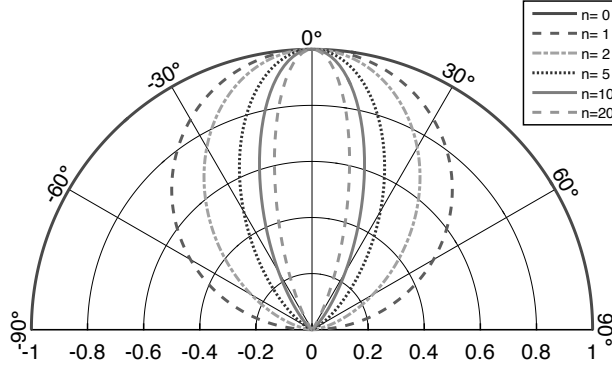

Figure 2.3. A cosine distribution $\cos^n\varphi$ for different values of the exponent n. The lobe of the vapour cloud is more narrow for larger values.

But even if all atoms initially travelled straight towards the substrate not all atoms would reach the substrate. The mean free path λ_{MFP} of the atoms has to be considered. The mean free path is the mean distance an atom travels before it collides with another atom or molecule. It depends on the size of the atom and the pressure, and for a gas of one type of atoms it is

$$\lambda_{\mathrm{MFP}} = \frac{1}{\sqrt{2}\pi d_0^2 n} = \frac{k_B T}{\sqrt{2}\pi d_0^2 P} \tag{2.1}$$

where d_0 is the molecular diameter and n is the density of the gas which has been rewritten in terms of pressure P and temperature T by the ideal gas law, and k_B is the Boltzmann constant [14]. Using a molecular diameter of about 5 Å for air at room temperature [11] and atmospheric pressure gives $\lambda_{\mathrm{MFP}} \approx$ 400 Å, and the molecules are colliding all the time. For a UHV chamber at base pressure of 1×10^{-9} torr$(= 1.33 \times 10^{-7}\,\mathrm{Pa})$ with the same assumption of molecular diameter, λ_{MFP} will be in the kilometre range, i.e. much much larger than the chamber, and collision with chamber walls is the main interaction. This illustrates both the cleanliness of UHV conditions and also shows the different properties a "gas" has in vacuum compared to atmospheric pressures. At the deposition pressure of about 2 mtorr$(= 0.27\,\mathrm{Pa})$ then $\lambda_{\mathrm{MFP}} \approx 1.5$ cm. But for sputtered atoms smaller diameters can be used and for e.g. Fe atoms in Ar $\lambda_{\mathrm{MFP}} \approx 7$ cm. For a target to substrate distance of 17.5 cm this means a

sputtered atom will collide about 2-3 times before it impinges on the substrate. In each collision it will change direction and some atoms will not reach the substrate which will decrease the deposition rate. Higher pressure will give more collisions and decrease the rate even more.

This effect of gas phase collisions has been simulated by Särhammar *et al.* [15, 16] and they show that there is a strong pressure dependence on the deposition rate distribution of sputtered atoms. The effect of gas phase collisions will give depositions everywhere in the chamber. A lower pressure gives more linear paths while the other extreme is an almost diffusion-like spread for very high pressures. The effect of the scattering is that the magnetron will create a vapour cloud which has some directionality.

In each collision an atom loses energy, and if it collides enough times the energy is in the range of the temperature $k_B T = 0.02$ eV and it is said to be thermalized. A higher pressure will give more thermalized atoms and the deposited atoms will have a fairly well defined energy. At lower pressure the energy will be smeared out from the maximum energy ~ 100 eV down to thermalization energy. Once the sputtered atoms have reached the sample surface their energy will enable them to move around on the sample surface. Energetic bombardment from ions can also give more energy to the adatoms on the surface. The energy of the adatoms will determine the structure in the resulting film, since if these adatoms have enough energy they can move to the minimum energy position, and where this is depends on for example the crystal structure.

Alloy thin films can be created by co-sputtering from several sources simultaneously. The composition of such a film will depend on the individual deposition rates of all the sources used.

3. Magnetic characterization

Three main mehtods for magnetic characterization have been used throughout this thesis: Superconducting Quantum Interference Device (SQUID) magnetometry, Vibrating Sample Magnetometry (VSM) and Magneto Optic Kerr Effect (MOKE).

SQUID
This is a method where the magnetization response from the entire volume of the sample is measured. The response in the magnetic moment is measured by two superconducting coils while another coil applies a field. The superconducting coils are connected to a Josephson junction and can in this way measure very small currents and hence very accurately determine the magnetic moment in absolute terms. To obtain superconductivity, the apparatus must be cooled to cryogenic temperatures which is both a big drawback for the technique but also an advantage since temperature scans can be performed, and also high fields can be applied. Another drawback of the technique is that samples must be cut in small $\approx 4 \times 4 \, \text{mm}^2$ pieces.

VSM
This technique is similar to SQUID magnetometry in the sense that it also measures the moment of the entire volume of the sample by the induced field in a pick-up coil [17]. Therefore the sample needs to be cut into small pieces for accurate measurements. There are different versions, both cooled and room temperature VSM. The cooled version can reach higher applied fields. The sample is vibrated in the applied field and the response in the pick-up coil is measured. Usually a lock-in-amplifier is used and by some mathematics involving the vibrational motion the magnetic moment is calculated. Compared to SQUID the accuracy is not as good since the induced voltage in the coils is measured using standard techniques.

MOKE
MOKE measures the rotation of the polarization of a laser beam reflected on the surface of the sample [18]. This rotation is proportional to the magnetization of the material and by applying a magnetic field over the sample the response in magnetization can be measured. MOKE comes in mainly three versions: Longitudinal where the field is applied parallel to the sample surface and parallel to the plane of incidence (of the laser), Transverse where the field is applied parallel to the surface but perpendicular to the plane of incidence,

and Polar where the field is applied perpendicular to the sample surface and parallel to the plane of incidence. Longitudinal and Transverse MOKE measure the in-plane magnetization while Polar measures the out-of-plane magnetization. The work in this thesis has only used Longitudinal and Polar MOKE. The biggest drawback of the technique is that the moment is only measured in relative terms and can not be compared between measurements. Usually the samples are measured to saturation and the moments are normalized to the saturation value. Therefore this technique is used for determining the shape of hysteresis loops and values of the coercivity. The advantages are that the technique is simple, it is relatively cheap (in comparison to SQUID) and can be adapted for various measurements, such as with varying temperature, or dynamic measurements on short time scales.

Part I:
FeNi with the L1$_0$ structure

4. Introduction to permanent magnets

As explained in the introduction permanent magnets are important for our modern society. In this chapter I will start by explaining the requirements on a permanent magnetic material (PMM) and the current status of the research on many different PMMs, before I present FeNi $L1_0$ which is the material I have studied experimentally.

4.1 Properties of permanent magnetic materials

The performance of permanent magnetic materials (PMM) in applications depend on both the intrinsic and extrinsic properties. The main intrinsic properties of a PMM are the saturation magnetization (M_S), the uniaxial anisotropy energy (K_U) and the Curie temperature (T_C). These determine the upper limits for the extrinsic properties and in real engineering materials the ideal intrinsic values are rarely reached. The most relevant extrinsic properties are the coercivity (H_C), the remanent magnetization (M_R) and, most important of all, the maximum energy product ($|BH|_{\max}$). Ideally $|BH|_{\max} = \mu_0 M_S^2/4$ which means that, of the intrinsic properties it is the saturation magnetization which should be maximized. But in reality, there can be no energy product if there is no coercivity, and the values of M_R and H_C are the limiting parameters. By the Stoner-Wohlfarth model of an ideal single particle the coercivity is given by the anisotropy energy and can be quantified by the anisotropy field $H_A = 2K_U/\mu_0 M_S$. According to Brown's theorem [19] this is the upper limit for H_C but in measurement on real materials the predicted maximum value of H_A is never reached, which is referred to as Brown's paradox. The situation is the same for M_R which never reaches the upper limit set by M_S. This is due to the microstructure: a real material is always composed of grains, with grain boundaries etcetera. These can act as either pinning or nucleation centres for magnetic domain walls. Still, in an initial stage when trying to find new high performance PMM, the parameters to look for are the intrinsic. Later the coercivity must be engineered through the microstructure. All of these parameters depend in some way on M_S, and therefore there is no point in looking into materials with large H_C if there is no saturation magnetization. The energy product can never be large in such a case.

Another important point which has to be taken into account is that the purpose for a PM is to produce external magnetic flux i.e. a stray field. An empirical measure of how well a magnet can do this is the magnetic hardness

parameter [20] which is defined as $\kappa = \sqrt{K_1/(\mu_0 M_S^2)}$. If $\kappa > 1$ the magnet can be shaped into any form and still produce a stray field, and such a material is called a hard magnetic material. If $\kappa < 1$ the shape of the magnet will matter. For certain geometries magnetic domains will form and the flux loop will close inside the material with no external stray field, and such materials are classified as semi-hard magnetic materials [20]. The first magnetic materials, such as steel magnets, had $\kappa < 1$ which is the reason why they were shaped in the form of horseshoes, since this geometry allowed for an external flux. Semi-hard magnetic materials can still be useful for certain PM applications if the constraints on the shape of the material are not too strict. For $\kappa < 0.1$ the material is a soft magnetic material and is not suitable as a PM.

As mentioned in the introduction chapter the highest (per mass) performing PMMs of today are Fe-Nd-B and Sm-Co based-PMs, where Sm-Co has better temperature stability but lower saturation magnetization. $Fe_{14}Nd_2B$ is usually doped with dysprosium (Dy) or terbium (Tb), which increases the coercivity at higher temperatures. But these are not the only PMM available. In table 4.1 a summary is given of the properties of many materials, whereof some will be mentioned in this thesis.
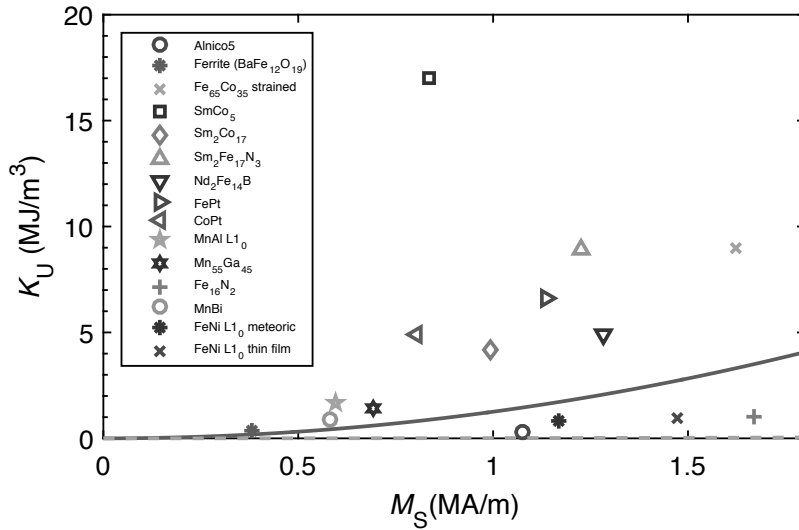

Figure 4.1. M_S vs K_U for selected materials. $\kappa = 1$ is drawn as the solid line. Materials above are hard magnets, materials in-between this line and $\kappa = 0.1$ (dashed line, almost coinciding with the horizontal axis) are semi-hard, and below $\kappa = 0.1$ soft magnetic materials. Values are taken from table 4.1.

Table 4.1. *Properties of PMM discussed in this thesis.*

Material	$\|BH\|_{\max}$ kJ m^{-3}	$\mu_0 M_S$ T	K_U MJ m^{-3}	T_C K	κ	ref.
$Fe_{14}Nd_2B$	512	1.61	4.9	588	1.54	[21]
$Fe_{14}(Nd_{1-x}Dy_x)_2B$ [f]	299	1.24[d]	-	493[f]	-	[22]
$SmCo_5$	231*	1.05	17.0	1020	4.40	[20],*[21]
Sm_2Co_{17}	294	1.25	4.2	1190	1.89	[21]
$Sm_2Fe_{17}N_3$	473*	1.54	8.9	694	2.17	[20],*[21]
$(Nd_{0.8}Ce_{0.2})_2Fe_{12}Co_2B$	127	-	-	695	-	[23]
$(Nd_{0.5}Ce_{0.5})_2Fe_{13}CoB$	116	-	-	590	-	[23]
Alnico5	46*	1.35	0.32	1240	0.45	[20],*[19]
Alnico9	83.6*	1.25	0.26	1260	0.45	[20],*[24]
$BaFe_{12}O_{19}$ (ferrite)	45	0.48	0.33	740	1.35	[21]
$SrFe_{12}O_{19}$ (ferrite)	34	0.48	0.35	746	1.4	[19]
$Fe_{16}N_2$	877[a]	2.10	1.0	810	0.53	[20]
$(Fe_{35}Co_{65})$ teor. strained	828[a]	2.04	9	-	1.65[b]	[25]
$(Fe_{0.35}Co_{0.65})_{16}C$	726[a]	1.91	1.92	-	0.81[b]	[26]
FePt	407[a]	1.43	6.6	750	2.02	[19]
FePd	379[a]	1.38	1.8	749	1.10	[19]
CoPt	203[a]	1.01	4.9	840	2.47	[19]
MnAl L1$_0$	112[a]	0.75	1.7	650	1.95	[19]
MnAl L1$_0$ exp.	95	0.39	-	-	-	[27]
$Mn_{55}Ga_{45}$ L1$_0$	130[c]	0.87	1.4	610	1.52[b]	[28]
$Mn_{55}Al_{34}Ga_{11}$ L1$_0$	140[a]	0.84	1.49	-	1.63[b]	[29]
MnBi B8$_1$	56*	0.73	0.9	633	1.46	[20],*[30]
FeNi L1$_0$ calculated	555[a]	1.67	0.77	916	0.6[b]	[31]
FeNi L1$_0$ neutron bombardment	503[a]	1.59	1.3	> 820	0.8	[20], [32]
FeNi L1$_0$ meteoric (43 at.%Ni)	318[c]	1.47	0.84	-	0.7[b]	[33]
FeNi L1$_0$ thin film	<676[c]	1.85	0.93	-	0.6[b]	[34]
$Sm_2Fe_{17}N_3$/$Fe_{65}Co_{35}$	1000[c]	2.24[c]	-	-	-	[35]
$Fe_{14}Nd_2B$/$Fe_{67}Co_{33}$ thin film	486	1.61[d]	-	-	-	[36]
$SmCo_5$/Fe, thin film	400	1.8[d]	-	-	-	[37]
$HfCo_7$/$Fe_{65}Co_{35}$ nanoparticles	161.5[c]	0.91[d]	-	-	-	[38]

[a] optimistic estimate calculated by $\|BH\|_{\max} = \mu_0 M_S^2/4$ from column 3. This only applies if $\kappa > 1$ and the material can be formed as a cylinder

[b] calculated by $\kappa = \sqrt{K_1/(\mu_0 M_S^2)}$ from column 3 and 4

[c] estimated by authors

[d] remanent magnetization

[f] Note that few values are published for Fe-Nd-Dy-B alloys of specific compositions. These values are for the highest temperature grade of a commercial magnet from www.arnoldmagnetics.com, Dy content is 12 wt.%. The temperature given is the maximum working temperature.

* value from ref *

4.2 Status of PMM research

This chapter presents a short summary of the most important points about the current research by other groups in improvement of REE PM and also in the area of REE free PM materials.

4.2.1 Approaches to improvement of REE PM

Sm based materials

The Sm-Co PM materials have the advantage of a very large uniaxial anisotropy and a large Curie temperature, but they have two major drawbacks. Firstly, Sm is a REE which should be avoided although the price is not as high as for Nd, which might make it a reasonable compromise. Secondly, it contains Co, which is a conflict metal and the conflicts in eastern Kongo have partly been fueled by mining of cobalt.[1] Pure Co is also toxic if ingested in excess amounts and irritating to the skin, and usage should therefore be avoided. The reason the FeNdB magnets were developed in the 1980s was because of the increasing prices on Co and the uncertainty in the supply due to the conflicts. $SmCo_5$ has the highest anisotropy of all PM materials, and a high Curie temperature, but a small saturation magnetization which results in a small energy product. Sm_2Co_{17} contains less Sm, which gives it a higher M_S but lower K_U and T_C. There is not much development on Sm-Co alloys but in recent years instead the samarium-iron nitrides have gained new interest. These contain less REE and no Co. $Sm_2Fe_{17}N_3$ rivals the properties of FeNdB, see table 4.1 [21, 39, 40, 41]. But so far, bulk fabrication has failed since nitrogen tends to diffuse during heat treatment. To achieve a useful magnet the material must be sintered, but then it loses the nitrogen. Recently some research has been done on different fabrication processes such as spark plasma sintering [42, 43].

FeNdB grain boundary engineering

It has been empirically known that reducing the grain size increases the coercivity but the reason for this was only recently explained by Sepehri-Amin *et al.* [44]. To increase the coercivity the grain size should be as small as possible, ideally on the order of single domain particles, to prevent domain nucleation inside the grains. Instead, the nucleation and pinning should occur at the grain boundaries. Smaller grains give smaller dipole fields and this prevents nucleation in neighbouring grains. A fabrication procedure to decrease the grain size has been developed and is now in use [45]. It uses a combination of the two processes called Hydrogen-disproportionation-desorption-recombination (HDDR) and Hydrogen decrepitation (HD) [46]. There is a subtle difference between the processes but both use annealing in H_2. What

---

[1]It should not be confused with the mineral Coltan, one of the major conflict minerals, which contains Niobium and Tantalum but no Cobalt.

the combination of the two does is, in short, to crack the material into sub micrometer grains surrounded by a Nd-rich phase.

Most of the research is now into what happens at the grain boundaries, what phases exists there, are there oxides, which elements etc. Concurrently with this, different ways to engineer the properties of the grain boundaries are explored. This is done mainly by grain boundary diffusion, and different elements such as Cu, Al or Ga are tested instead of Dy or Tb. Their non magnetic properties should decouple the grains and increase the coercivity. Some of the processes have reached very far and some are already introduced in the production lines. Hirosawa [47] gives a review of the progress and status in the area.

FeNdB REE substitution

The groups at Ames Laboratory in Iowa have shown that Ce substitution of Nd in FeNdB gives decreases in M_S, H_C and $|BH|_{max}$ but when simultaneously substituting Fe for Co they regain the properties. It turns out that for 20 at.% Ce substitution and optimal Co substitution, $(Nd_{0.8}Ce_{0.2})_2Fe_{12}Co_2B$, the properties even at elevated temperatures are higher compared to a 5.2 wt.% Dy substitution $(Nd_{0.8}Dy_{0.2})_{10}Fe_{84}B_6$. This would greatly reduce the cost since Dy is eliminated but also Nd is replaced for the more abundant Ce. If more Ce is substituted at 50 at.% with another optimal Co composition resulting in $(Nd_{0.5}Ce_{0.5})_2Fe_{13}CoB$, the properties are slightly lowered but they are still comparable to Dy substituted FeNdB [9].

4.2.2 Exchange spring coupled nanomaterials

If a hard magnetic material could be combined with a soft magnetic material in a nanocomposite, a phenomenon called exchange coupling can occur [35, 48]. The hysteresis loop of an exchange coupled material will have the coercivity of the hard magnetic material and the remanent magnetization of the soft magnetic material. The advantage of this is that both large coercivity and high remanent magnetization are usually difficult to achieve simultaneously, while there are many materials with either a high H_C but low M_R or vice versa. By combining two materials which individually are not very good PMs, a material with very good properties in total can be achieved. According to Skomski [49] the optimal geometry is one where spherical inclusions of a soft magnetic phase are embedded in a hard magnetic phase. The geometry should fulfil the requirement that the thickness of the soft material should not be larger than two times the magnetic domain wall thickness of the hard material. Ideally the volume ratio of the soft phase should be up to 80 %. This gives potential for reducing the total REE content if a REE PM is chosen as a hard phase. The highest theoretical predicted value of any magnet is $|BH|_{max} \approx 1\,MJ\,m^{-3}$ for a exchange-coupled multilayer of $Fe_2Sm_{17}N_3/Fe_{65}Co_{35}$ which has only 5 wt % REE material [35].

This is a large field of research since there are many available materials and therefore numerous combinations, including REE free hard phases. The challenges are how to achieve the different phases and how they should not react with each other and form new phases. This should be done while still fulfilling the geometrical constraints. In thin film multilayer form such materials have been fabricated, and the record is held for $Fe_2Nd_{14}B/Fe_{67}Co_{33}$ with $|BH|_{max} \approx 480\,kJ\,m^{-3}$ [36] and for $SmCo_5/Fe$ with $|BH|_{max} \approx 400\,kJ\,m^{-3}$ [37]. Then there is the ubiquitous problem of how to scale up the production from thin film to bulk.

4.2.3 Examples of REE free PM materials candidates

As stated before when searching for a new PMM the first things to look for are the intrinsic properties, M_S, K_U and T_C. If these are good there is a higher chance also the extrinsic properties are satisfactory. But the final parameter which matters in applications is the energy product $|BH|_{max}$. Below is listed a selection of possible REE free PMM candidates. Although research is currently performed on improving ferrites such as $BaFe_{12}O_{19}$ or $SrFe_{12}O_{19}$, which are very common in applications today, these are not treated here.

Alnico

The PM properties of Alnico (consisting of Al, Ni, Co and Fe) comes from the shape anisotropy of the nano sized FeCo needle structure embedded in AlNi. The material was invented in the 1930s and has been used in many applications since then. Now it is studied again, but with today's tools of nanotechnology.

The issue with Alnico is that it is a semi-hard magnet i.e. $\kappa = 0.45$. Therefore it is limited to certain shapes and the flux can only exit the magnet in certain directions. It has a large value of magnetization but small anisotropy. What makes it stand out is the very good temperature stability: at $200\,°C$ the energy product is comparable with that of $Fe_2Nd_{14}B$ [22]. Since the magnetization comes from the needles of FeCo the potential for high flux is large. The hope is that these grains which are formed in a spinodal decomposition can be controlled and engineered, as it has been shown that they have a suboptimal size and distribution. Recent work has given deepened understanding of the material on a nanometer scale but significant progress in enhancing the properties has not been achieved [24].

MnBi

MnBi with the hexagonal $B8_1$ structure [20] has quite good magnetic properties which would be better than Alnico and ferrites. The anisotropy comes from a strong spin-orbit coupling in Bi. It also has the interesting property that the anisotropy increases with temperature. It is fabricated as sintered bulk magnets and it is available commercially. But the drawback is that the magnetic phase decomposes at $355\,°C$ and the bulk powder is only stable to $200\,°C$

[50]. At higher temperatures Bi starts to segregate and form Bi grains. It has a low temperature phase and a high temperature phase, which have quite different properties. Due to this temperature dependence it is not suitable for most applications. Another drawback is that Bi with its low melting point is difficult to handle, and it is not very abundant and hence expensive. The new idea is to use it as a hard phase in exchange coupled materials (se section 4.2.2).

$Fe_{16}N_2$

The simplicity of nitrogenated iron, $Fe_{16}N_2$, is deceiving. Fe has the highest moment of all elements but it is not hard magnetic, and it does not have any uniaxial magnetocrystalline anisotropy. If Fe could just be given a uniaxial anisotropy it would have very good properties. It has been shown that N additions could give Fe a distorted structure and $Fe_{16}N_2$ has been fabricated in thin films, nanoparticles and in bulk [51, 52]. But it has proven very difficult to put the nitrogen atoms into the correct positions and to make them stay there. Already at 100°C nitrogen diffuses and evaporates from the material. The company Advanced Materials Corporation claims to have a process which can produce the material in enough quantities to sell.

Tetragonal FeCo

Actually there is an alloy which has an even higher moment than Fe: the $Fe_{65}Co_{35}$ alloy Permendur. The materials theoreticians at Uppsala University showed in 2004 [25] that if this material would be tetragonally strained (i.e. $c/a > 1$) it would supersede all other materials in terms of simultaneous uniaxial magnetocrystalline anisotropy and saturation magnetization, see fig. 4.1. Recent calculations show that B or C additions should create such a structure, $(Fe_{0.35}Co_{0.65})_{16}C$ [26]. The structure is related to $Fe_{16}N_2$ but here Fe is substituted with Co and for stabilization C or B are used instead of N. This phase is actually identical to martensitic Fe but with Co substitution. A major challenge is to align the crystal domains. Attempts at fabrication in bulk have not been entirely successful [53]. Also some attempts to make thin films have been made, but the strain in the material relaxes easily [54].

$L1_0$ intermetallics including FeNi

Of the four magnetic 3d elements, Mn, Fe, and Ni are quite abundant, cheap and easy to mine. The fourth element, Co, is a conflict material and usage should therefore be avoided. But neither Fe, Ni nor Mn have any uniaxial magnetocrystalline anisotropy since they have a cubic crystal structure. Mn couples antiferromagnetically both in pure form and in alloys, which at have best a small saturation magnetization. But if either of these cubic elements could be tetragonally strained they would have a uniaxial magnetocrystalline anisotropy, and the lattice expansions could make Mn atoms couple ferromagnetically, according to the Bethe-Slater curve [19, 55].

In the previous two examples, $Fe_{16}N_2$ and tetragonal FeCo, a strained material was achieved by alloying with N, C or B, where both material systems suffer from diffusion, but there is also another approach. The $L1_0$ structure is a tetragonally strained cubic structure and therefore attempts have been made to find different alloys with Fe, Ni or Mn which form the $L1_0$ structure. Aside from the tetragonal strain the $L1_0$ structure is chemically ordered with a stacking of monolayers (ML) of either element, see fig. 4.2. This structural and chemical anisotropy is what gives the material its uniaxial anisotropy. The common synthesis challenge for all $L1_0$ alloys is to stabilize the phase enough so that it does not go through the order-disorder phase transformation into the chemically disordered A1 phase, which is an fcc structure with random positions of each element. Usually the $L1_0$ phase has the lowest free energy but the energy gap to the A1 phase is often small. There is also an unanswered question whether the tetragonal distortion gives the chemical ordering, or vice versa, or if one can not exist without the other.
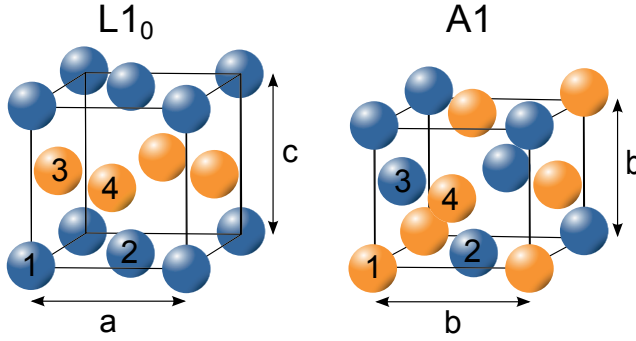
Figure 4.2. Left: schematic of a $L1_0$ unit cell, where atoms 1 and 2 are of element A and atoms 3 and 4 are of element B. The structure is tetragonally strained with $c/a > 1$. Right: schematic of an A1 unit cell, an fcc structure with equal cube sides, where the atoms of each element can have any random position distribution. In this example atoms 1 and 4 are element A and atoms 2 and 3 are element B.

FePt/Pd, CoPt/Pd, NiPt

CoPt was the first $L1_0$ material to be discovered, already in the 1930s [22]. The reason for it not being commonly used is the cost of the noble metal. Initially the alloys used were polycrystalline, meaning the material had $L1_0$ grains with different orientations, decreasing the total magnetization and anisotropy. All the different variants of either Fe and Co together with one of the noble metals Pd or Pt exist, and FePt has the highest $M_S =1.43\,T$ and $K_1 =6.6\,MJ\,m^{-3}$ (larger than $Fe_{14}Nd_2B$!) [19]. These materials are easily formed into $L1_0$ structure by simply annealing the disordered phase [56, 57]. As already mentioned the cost is an issue, as 50 % of the material consists of a noble metal. A further problem is how to achieve single crystals or to align the grains. Related

are also the non-equiatomic alloys such as Fe_3Pt forming into the similar $L1_2$ structure, which has similar properties although the anisotropy is small.

MnAl and MnGa

In the 1990s you could actually buy loudspeakers with τ-MnAl magnets, but when the prices on REE PMs decreased these were replaced [58]. The problem with the τ-phase (the $L1_0$ structure) is that it is actually metastable [59], and to increase the stability it is alloyed with carbon. But τ-MnAl usually degrades over time, even when stabilized with C. Also the fact that half of the material is non-magnetic Al (and even more when alloyed with C) gives a small M_S. MnGa has similar and slightly larger values of the magnetic properties compared to MnAl, but then Ga is much more expensive. An advantage is that MnGa is stable in bulk [28, 60] and therefore attempts have been made to substitute Al for Ga and to find the optimal substitution. This work is still on-going, and not yet published reports by Mix [29] show an increased stability, $\mu_0 M_S = 0.8$ T and $K_1 = 1.49$ MJ m^{-3}.

FeNi

FeNi in the $L1_0$ phase, when compared to the other $L1_0$ alloys, has the advantage of two magnetic elements, giving a much larger $\mu_0 M_S = 1.6$ T. The predicted $K_U = 0.8$ MJ m^{-3} [31] is not as good though, and the resulting $\kappa = 0.6$ means it is only a semi-hard material. It is still interesting to study since H_C can be engineered through the microstructure, and it can be a good magnet for the right geometry. Since the material exists in such small quantities we still do not know about all of its properties, as is indicated by the variation in values in table 4.1. The main problem with this phase is the slow kinetics during formation. It is found in nature in meteorites where it has been formed in space during hundreds of millions of years with cooling rates of less than 1 K per million years [33]. The challenge when synthesizing is that the phase boundary is at such a low temperature, 320 °C, that basically no diffusion occurs at this or lower temperatures. When synthesizing, heating is not very effective since this will only make the alloy transform into the disordered phase [61]. The diffusion has to be promoted by some other means. In one report the authors state they have manufactured the phase by severe plastic deformation [62], and in another report by a chemical reaction [63]. Even in thin film form it is difficult to synthesize but it has been done by Takanashi's group [34] and also in this work as will be described in Papers I and II.

5. Synthesis of FeNi L1$_0$

5.1 The L1$_0$ structure

As was described in the previous chapter FeNi with the L1$_0$ structure, which has been the focus of this thesis work, is an interesting candidate for new intermediate strength permanent magnets. L1$_0$ is the lowest energy phase of this material system at the 50/50 at.% composition [64] and is therefore a stable phase. The practical problem of formation is the slow diffusion below the phase boundary at 320 °C. This structure is composed of alternating monoatomic layers of Fe and Ni where the atoms have the positions of a tetragonally strained fcc structure. This means the in-plane lattice parameter a is smaller than the out-of-plane lattice parameter c i.e. $c/a > 1$ (see fig. 4.2).[1] It is important here to point out that this structure is anisotropic. It is different in the direction of the c-axis compared to the a-axis directions. Along the c-axis there is a stacking of chemically different planes in addition to the larger lattice parameter. This structural and chemical anisotropy is what gives the material its magnetic anisotropy in comparison to the chemically disordered A1 phase, which has no anisotropy. Therefore the chemical ordering of Fe and Ni into monolayers is of utmost importance for the magnetic properties of the L1$_0$ phase.

The FeNi L1$_0$ system needed more study, both of the magnetic properties but also the synthesis. Four groups have been doing this: Northeastern University in a group led by Lewis, the group of Takanashi in Tohoku, the group of Sagawa in Kyoto, recently Makino from another Tohoku group and lastly our group. Since our speciality is thin films and we have fabricated very well ordered multilayers before, we believed we could fabricate this material in thin film form. Even though the ultimate goal is to fabricate the material in bulk it is still motivated to study in thin film form since there does not exist much material in the world to study. What has been studied was found in meteorites, but that material was embedded into a matrix together with other phases [65, 66]. Other studies have been made on small amounts of material fabricated by neutron bombardment [67] and electron irradiation [68]. The study of this material in pure form has only been done in the thin films by Takanashi's group [34] and more work is needed.

In this chapter I will present and summarize the experimental work to fabricate and characterize this phase. The results are presented in Paper I and

---

[1]By tradition I will view the structure as this tetragonal fcc even though this is not the fundamental and crystallographically correct unit cell, which would be a body centred tetragonal (bct) cell.

Paper II. Related work on Fe/Ni multilayers fabricated with the same methods but not in the $L1_0$ phase is presented in Paper III. In the following sections, I will also present some experimental observations concerning the growth method which have not been included in the papers.

5.2 Definition of the directions and orientations

We will use the following directions and orientations to describe the structure. The nominal orientation is with the c-axis of the $L1_0$ unit cell parallel to the surface normal (z-axis) of the film grown. This direction will also be referred to as the out-of-plane direction. In reciprocal space the [$00l$] direction is parallel to the surface normal and the ($00l$) planes are parallel to the surface, i.e. the film is referred to as (001) oriented. In a symmetric x-ray diffraction (XRD) scan the scattering vector **Q** is parallel to the surface normal. In an epitaxial (001) oriented film, such a scan probes the ($00l$) planes and only multiples of these reflections should be seen. In the symmetric scans the length of the scattering vector is given as:

$$|Q| = \frac{4\pi \sin\theta}{\lambda} \tag{5.1}$$

where 2θ is the scattering angle and λ the wavelength of the x-rays.

Asymmetric scans have also been used to determine the in-plane lattice parameter a. In these scans **Q** was not parallel to the surface normal and reflections from other planes than ($00l$) were thus measured.

5.3 Synthesis by sputtering

Our approach to synthesize the $L1_0$ phase is by DC magnetron sputtering rather than molecular beam epitaxy (MBE) (which was used by Mizuguchi [69]). Magnetron sputtering is a versatile technique which has many parameters to tune compared to MBE. Since heating and diffusion can not be used for the formation of the phase we tried to circumvent the diffusive phase formation by instead creating the material by deposition in a (mono)layer-by-layer fashion, see fig. 5.1. This requires very precise control of the sputtering deposition rates, which in fact can be achieved. It also requires that the film is deposited with the (001) orientation, and to ensure this we used epitaxial growth on a (001) oriented Si substrate.

5.3.1 Epitaxial growth of Cu on Si substrates

We have used Si substrates which are common and cheap and actually have a lattice parameter which is quite close to the one of FeNi $L1_0$. The use of Si
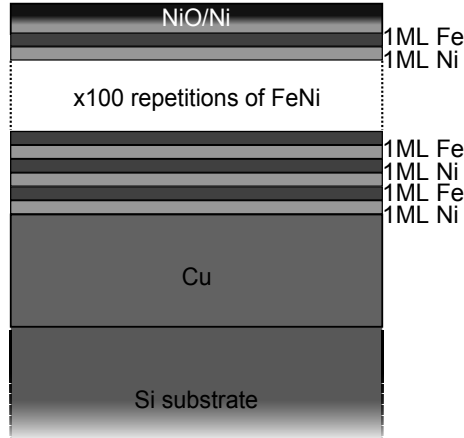
Figure 5.1. Schematic representation of the FeNi samples. Most samples had a repetition of 100 bilayers of Fe/Ni. In Paper II an additional CuNi layer was inserted between the Cu buffer and Fe/Ni layers. In Paper III the thicknesses of Fe and Ni layers were kept equal but varied from 4 ML to 48 ML.

substrates also opens up for the possibility of integration into semiconductor devices. The structure of Si(001) is cubic and the diagonal of the lattice parameter is 3.84 Å, i.e. close to the wanted 3.57 Å for FeNi $L1_0$. Since the Si lattice parameter is slightly too large we used Cu as a buffer layer which we wanted to relax so that it regained its bulk lattice parameter of 3.61 Å.

To enable epitaxy the native oxide layer on the Si had to be removed. According to literature Cu grows epitaxially on Si(001) etched with hydrofluoric acid (HF) [70, 71, 72, 73], and furthermore Ni should grow epitaxially on Cu(001) [74]. Our experiments did indeed show that by HF etching Si, Cu could grow epitaxially on this hydrogen terminated Si surface, as is shown by the x-ray diffraction results in Paper I. Furthermore, we saw that the etched Si wafers are quite stable and the 30 min–60 min which they were exposed to air did not seem to affect the growth. The etched substrates could also be stored for up to a month in the vacuum chamber load-lock (with a pressure of 1×10^{-8} torr) without any measurable degradation. The surface quality was measured by contact angle measurements [75, 76]. Freshly etched substrates were compared to substrates which had been stored for more than two months, all having about the same contact angle.

Different temperature schemes were tested for the growth, from room temperature up to 210 °C. A problem we encountered was copper silicide (Cu-Si) formation. This occurred either if the Cu was deposited while heating the substrate or if the annealing of the buffer layer was performed above 180 °C. At 200 °C the silicide formation is a question of time, and the full 1000 Å Cu films transformed into silicide after about 15 min. In films where Cu-Si has formed all the way through the Cu layer, the epitaxy is lost and here the FeNi layers

lose the (001) orientation and become (111) oriented. By ocular inspection it could easily be seen which film had formed silicide since the surface became milky and diffuse compared to the reflective surface of an epitaxial Cu film. Due to these challenges all buffer layers were deposited at room temperature and subsequently annealed. Initially we also experienced problems with silicide formation even at room temperature. This risk was eliminated by a 1 h heat treatment of the substrate at 300 °C at base pressure (ultra high vacuum) followed by cool-down to room temperature.
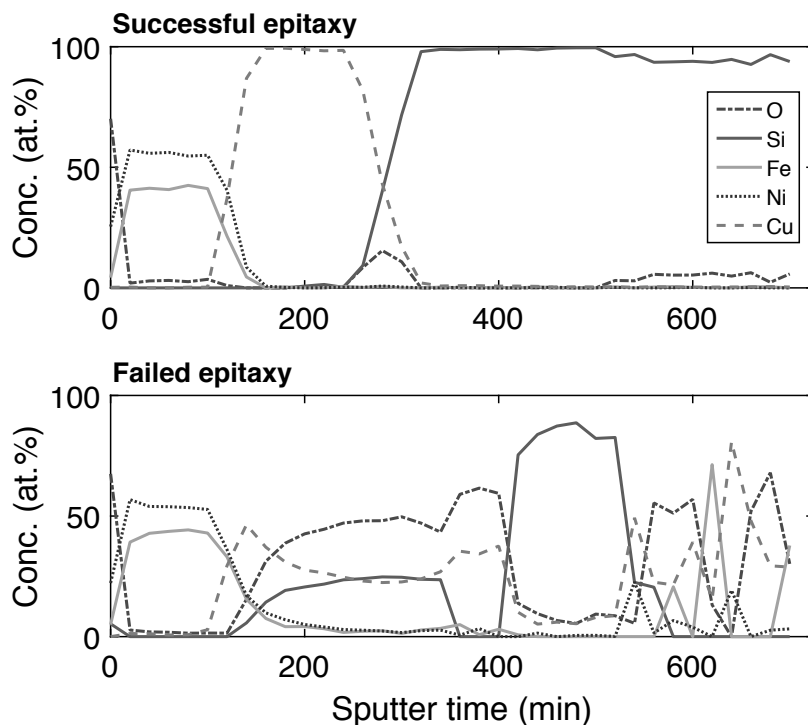
Figure 5.2. Depth profiling XPS using Ar ions, where the sputter time is proportional to depth into the samples. These two samples were deposited at the same time next to each other. On one piece the epitaxy failed and on the other it was successful. In the successful sample some oxygen can be seen at the Si/Cu interface. The failed sample has formed CuSi and reacted with O all the way up to the FeNi layer but the Cu, Si and O do not seem to diffuse into the FeNi.

Depth profiling x-ray photoelectron spectroscopy (XPS) was performed to determine the diffusion in the films, see fig. 5.2 and fig. 5.3. It could be seen that for films where Cu-Si has formed during growth, Si goes all the way to the surface. These films also have oxygen inside. This presence of oxygen was seen in larger extent for the earlier samples where the substrates had not been heat treated. Therefore we believe the oxygen is promoting silicide formation and loss of epitaxy. Another factor could have been variations in the

35

thermal contact between the substrate and sample holder, and thus for later batches other clamps were used which gave more consistent sample mounting. In films where Cu-Si has been formed after the FeNi layer was deposited there is no intermixing of Si into the FeNi layer, fig. 5.3, within the depth resolution of XPS. Even for films which have not formed Cu-Si and which still are (001) oriented there is a slight diffusion of Cu into the FeNi, but not noticeably larger than in the film which formed Cu-Si. When annealing a film, see fig. 5.3, the diffusion of Si into Cu is faster than the possible diffusion of Cu into FeNi, which seems very slow, and it is difficult to quantify due to the depth resolution. In conclusion, the Cu-Si diffusion is the limiting factor for the temperature during growth of this thin film system. We could see better crystalline quality for higher temperatures but the silicide formation confined our temperature range to $< 180\,°C$. This restriction in temperature is acceptable since Kojima *et al.* [77], who used another substrate and buffer layer solution, found that the optimal growth temperature for their FeNi thin films is $< 190\,°C$.

5.3.2 Epitaxy of FeNi on Cu

The purpose of the Cu buffer layer was to reduce the lattice parameter to more closely match that of FeNi. If Cu grows epitaxially on Si it will initially be under tensile strain with the same in-plane lattice parameter as Si, but if it is thick enough relaxation will occur and the Cu lattice parameter decreases. This will introduce dislocations and surface roughness. Therefore, when choosing the thickness there will be a trade-off between lattice match of the buffer and FeNi film versus the surface quality. To find the thickness where the Cu buffer relaxed to the optimum lattice parameter we used a combinatorial technique which will be explained in Part II (see fig. 6.13). As close lattice match as possible between the Cu and FeNi was achieved with a thickness of $1000\,\text{Å}$, since then the Cu lattice parameter was equal to the bulk value, see fig. 5.4.

In Paper II we investigated the effect of the in-plane lattice parameter a of the buffer layer on the induced strain in the FeNi film. To tune a we used a CuNi buffer of different compositions on top of the Cu buffer. Cu and Ni both have fcc structure and are soluble in each other which means the lattice parameter of the alloy can be controlled linearly by the composition, according to Vegards' law [78].

The sought after epitaxial relationships $Si(001)[110] \parallel Cu(001)[100]$ and $Cu(001)[100] \parallel FeNi(001)[100]$ between Si and FeNi through Cu, as well as $Cu(001)[100] \parallel CuNi(001)[100] \parallel FeNi(001)[100]$ between Cu and FeNi through CuNi, was confirmed by in-house XRD which can be seen in the pole figures and reciprocal space maps (RSM), see Paper I and Paper II. As a contrast to this epitaxial growth, in Paper III some of the Fe and Ni layers were so thick that the epitaxy was lost. This could easily be seen since reflec-
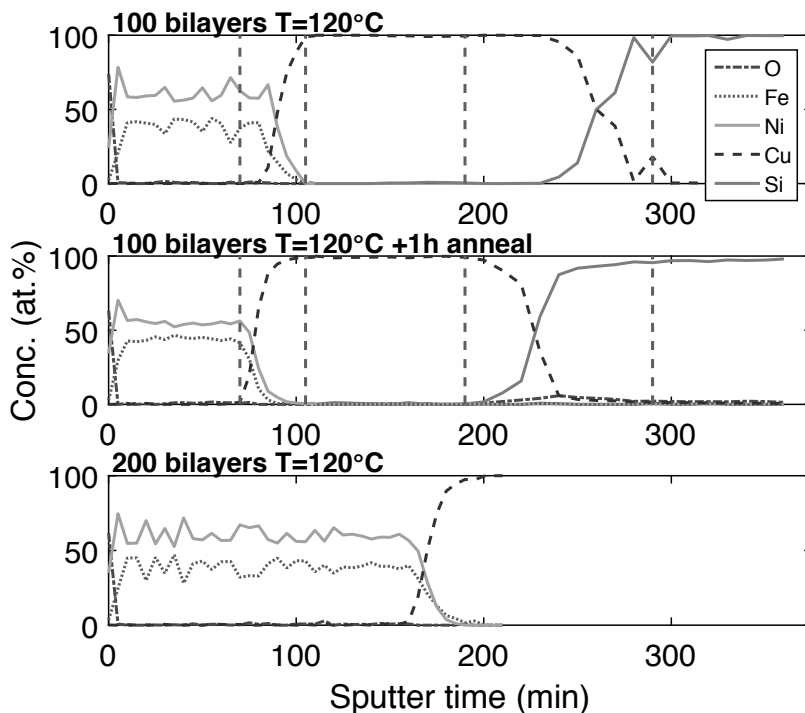
Figure 5.3. Depth profiling XPS using Ar ions, where the sputter time is proportional to depth into the samples. These three scans show the propagation of Cu diffusion for samples all grown at 120 °C. The middle scan shows the same sample as in the top but after an additional annealing at 120 °C for 1h after deposition. As can be seen, the major diffusion is from Si into Cu. The Cu diffusion into FeNi seems to be within the measurement uncertainty. The bottom scan is from a sample with 200 repetitions of the FeNi layers. The Cu diffusion is not larger here even though the growth time and thus effective annealing was twice as long.

tions other than from (00l) appeared in the symmetric $\theta/2\theta$ diffraction scans. The crystalline quality of all layers in the films was fairly good but there was some mosaicity of a few degrees. The quality of the (CuNi and) FeNi film seemed to follow that of the Cu buffer layer. Both the XRD correlation length and mosaicity are correlated between the buffer layer(s) and the FeNi layer. Therefore to enhance the quality of the FeNi the most effective approach will be to improve the buffer. We could see that the heat treatment improved all parameters measured by XRD both in the FeNi and the buffer layer. The diffusion between the Cu and FeNi did not seem to be a problem either (fig. 5.3). Therefore we used as high temperature as possible, below the limiting value 180 °C, (see above).

The surface roughness of the Cu buffer was measured with atomic force microscopy (AFM), fig. 5.5. What we found agreed with previous reports
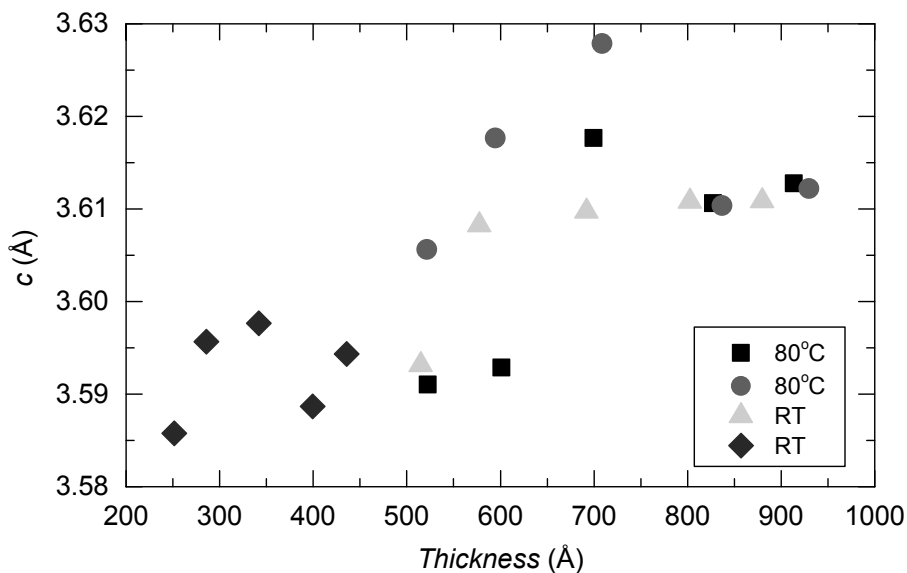
Figure 5.4. Out-of-plane lattice parameter c of Cu layer vs Cu layer thickness for Cu thickness gradient samples. There is a large uncertainty in the measurements due to the use of Cu $K_{\alpha1+2}$ radiation and suboptimal optics. Above 1000 Å Cu thickness, all lattice parameter values converge.

[79, 80, 81]. The Cu surface is composed of mound shaped islands with a lateral size of ≈ 300 Å and a roughness of 3 Å to 10 Å. This was also seen by transmission electron microscopy, where surface modulations of ≈ 500 Å could be seen in the FeNi layer (Paper III). As will be described in later sections the surface roughness of the buffer layer is important for the $L1_0$ formation.

Optimization of the buffer layer is very complex and time consuming. There are several parameters to tune: the thickness, the growth temperature, annealing temperature, and annealing time. There are also several properties to optimize: the surface roughness, the crystalline quality (e.g. mosaicity, correlation length) and the resulting lattice parameter. For Paper II optimizing the buffer layers became even more complex with a doubled set of parameters and the properties of Cu and the CuNi which are dependent on each other. AFM proved to be difficult to use for such an optimization, and we could not get reliable quantitative measurements. But within the limitations we saw that thicker buffers might increase the roughness. Heat treatment also seemed to increase the roughness, and a possible increase in island size was also seen by AFM. XRD results indicate enhancement of all crystalline properties with increasing thickness and warmer heat treatment. In addition to this the wanted lattice parameter should also be taken into account, and it could be tuned by both thickness and composition in the CuNi. In conclusion, a compromise
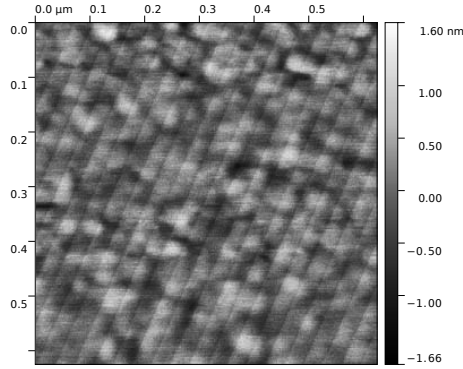
Figure 5.5. Atomic force microscopy on the surface of a 1000 Å Cu buffer layer capped with a 25 Å thick Ni layer. The mound shaped surface can be seen.

had to be made between surface roughness and crystalline quality. We decided to mainly consider the crystalline quality and lattice parameter since those we could quantify with certainty. There is still room for improvement of the buffer.

With this method of epitaxial growth of $(Fe/Ni)_n/Cu_{100-x}Ni_x/Cu/Si$ or using $(Fe/Ni)_n/Cu/Si$ we could achieve a good crystal structure of the FeNi layer but confirming the formation of the $L1_0$ phase requires some deeper description of XRD which is the topic of the next section.

5.4 Confirming the chemical ordering by resonant XRD

If FeNi is $L1_0$ ordered there should be alternating monolayers (ML) of Fe and Ni. These thin layers are very difficult to measure with most techniques. Many techniques for structural and chemical characterization are dependent on the atomic number e.g. by measuring the electron density. This is an important limitation on the material system discussed here since Fe and Ni have almost the same number of electrons (26 and 28) and the contrast will be small. In paper III characterization attempts using some different techniques on thicker Fe and Ni layers are described. X-ray diffraction is the standard technique for determining crystal structure and fortunately the FeNi $L1_0$ structure is possible to measure by XRD although this is difficult to do with an in-house x-ray source. In XRD each superstructure of either Fe or Ni will give a reflection of these (001) layers only if the sample is chemically ordered ($L1_0$), but this reflection will not occur if it is chemically disordered (A1). The problem is that the intensity of the 001 reflection is proportional to the square of the difference in electron density of Fe and Ni and there will be very little intensity. The measurements are greatly improved if the energy can be tuned using synchrotron light. With x-ray energies close to the absorption energy of either Fe or Ni there is a resonance of the atomic form factors which deviate from

the proportionality to the number of electrons, and they can have large values. This will increase the contrast between Fe and Ni. When measuring small intensities care must also be taken with respect to the background and fluorescence. In the following sections the basic concepts of this analysis for symmetric diffraction will be described.

5.4.1 Intensity of diffraction peaks

The intensity of an arbitrary diffraction peak depends on many different parameters. In text books such as Cullity, Birkholz [82, 83] and others the intensity is usually given by the following equation

$$I_{hkl} = SCF \cdot m_{hkl} \cdot T_{hkl} \cdot G(\theta) \cdot \bar{C}(\theta)^2 L(\theta) \cdot |F_{hkl}|^2 \cdot A(t,\theta) \cdot \mathrm{e}^{-2M(\theta)} \quad (5.2)$$

This is the most general version of the equation and it can be applied to powder diffraction, but for single crystal diffraction, or for diffraction on thin films or if synchrotron radiation is used the included terms will be modified, as will be described below. SCF is the scaling factor that lumps together instrumental settings. m_{hkl} is the multiplicity of a reflection, determined by the symmetry. For single crystal diffraction the multiplicity factor is 1 since only one specific reflection is measured (e.g. (001) instead of {001} for powder diffraction). T_{hkl} is the texture factor which describes the fraction of grains oriented in the specified direction. For single crystal diffraction the texture factor is 1 since only one specific reflection is measured.

Lorentz polarization factor
Usually $G\bar{C}^2L$ are lumped together and called the Lorentz polarization factor. G is the geometry factor, $\bar{C}^2$ is the polarization factor, and L is the Lorentz factor. The combined factor Lp is given by

$$Lp = G(\theta) \cdot \bar{C}(\theta)^2 \cdot L(\theta) = \frac{1}{2\sin\theta} \cdot \frac{1+\cos^2 2\theta}{2} \cdot \frac{1}{\sin 2\theta} = \frac{1+\cos^2 2\theta}{\sin\theta \sin 2\theta} \quad (5.3)$$

Geometry factor
The geometry factor can be written as

$$G(\theta) = \frac{1}{2\sin\theta} = \frac{\cos\theta}{\sin 2\theta} \quad (5.4)$$

It describes the smearing of a reflection over the cone with the opening angle 4θ, which becomes the ring in a texture scan for a polycrystalline or powder sample. This is due to the random orientation of crystallites in a powder or a polycrystalline material and hence for single crystal diffraction $G(\theta) = 1$.

Polarization factor

For circularly polarized light as from the tube of an in-house diffractometer the relation is

$$\bar{C}_{circ}(\theta)^2 = \frac{1+\cos^2(2\theta)}{2} \tag{5.5}$$

The polarization factor will be different for synchrotron measurements compared to in-house XRD. It is derived in the following way. The scattered intensity from an electron (Thomson scattering) is

$$I = I_0 \frac{K}{r^2} \sin^2(\alpha) \tag{5.6}$$

for light of intensity I_0 propagating in the x direction with the polarization in y and z directions. r is the distance from the scattering centre and α is the angle between scattering direction and acceleration of the electron (which depends on the polarization), K is a constant composed of fundamental constants. The total intensity is given by $I = I_y + I_z$. Then if xz is the scattering plane the respective intensities become

$$I_y = I_{0y} \frac{K}{r^2} \tag{5.7}$$

$$I_z = I_{0z} \frac{K}{r^2} \cos^2 2\theta \tag{5.8}$$

For circularly polarized light $I_{0y} = I_{0z} = \frac{1}{2}$ and we have

$$I = I_0 \frac{K}{r^2} \left(\frac{1+\cos^2 2\theta}{2} \right) \tag{5.9}$$

But at a synchrotron the light is linearly polarized in the plane of the ring, i.e. $I_{0z} = 0$, and the expression becomes

$$\bar{C}^2_{synchr} = I = I_0 \frac{K}{r^2} \tag{5.10}$$

This factor which is constant for a specific diffractometer can be shuffled into the *SCF* term.

Lorentz factor

The Lorentz factor is related to the peak broadening and sample extension along the beam. Therefore it also depends on the divergence of the beam and the acceptance of the detector.

$$L(\theta) \propto \frac{1}{\cos\theta} \frac{1}{\sin\theta} \approx \frac{1}{\sin 2\theta} \tag{5.11}$$

where the first cosine factor is the same as in the peak broadening described by the Scherrer equation (see Birkholz [83]). The second sine factor is related to

the footprint, which will be described later. A scaling factor, which depends on the slits, sample size, acceptance of the detector etcetera should be multiplied but this is baked into SCF.

The Lorentz polarization factor for single crystal measurements at a synchrotron then becomes

$$Lp = G \cdot \bar{C}^2_{synchr} \cdot L(\theta) = 1 \cdot 1 \cdot \frac{1}{\sin 2\theta} = \frac{1}{2\sin\theta\cos\theta} \qquad (5.12)$$

When performing diffraction with different energies at a synchrotron it is more convenient to work with the length of the scattering vector $|Q|$ instead of θ:

$$|Q| = \frac{4\pi\sin\theta}{\lambda} \qquad (5.13)$$

and then the Lorentz polarization factor becomes

$$Lp(Q) = \frac{1}{\sin\left(2\arcsin(\frac{|Q|\lambda}{4\pi})\right)} = \frac{2\pi}{|Q|\lambda\cos\left(\arcsin(\frac{|Q|\lambda}{4\pi})\right)} \qquad (5.14)$$

Absorption factor $A(t,\theta)$
$A(t,\theta)$ is the absorption factor which comes from the fact that the beam is attenuated the longer it travels into the film. Hence it depends on the angle, the thickness t and the linear absorption coefficient of the film μ, (which is also energy dependent and tabulated e.g. by Sasaki [84]). For smaller angles the path through the film is longer. This term can also be viewed as the volume of the sample which produces fluorescence as we will discuss later. It is given by the following expression:

$$A(t,\theta) = \left(1 - \exp\left(-\frac{2\mu t}{\sin\theta}\right)\right) \qquad (5.15)$$

Structure factor $|F_{hkl}|^2$
The structure factor $|F_{hkl}|^2$ is what gives the actual diffraction pattern and it includes the atomic form factors and depends on the reflection hkl.

$$F_{(hkl)} = \sum_{n=1}^{N} f_n(Q,E)e^{2\pi i(hu_n+kv_n+lw_n)} \qquad (5.16)$$

N is the number of atoms in a unit cell, f_n is the atomic form factor of atom n and u_n, v_n, w_n is the coordinates of atom n.

For FeNi L1$_0$ the structure factors of 001 and 002 reflections are:

$$F_{(001)} = 2\left(f_{Fe} - f_{Ni}\right) \qquad (5.17)$$

$$F_{(002)} = 2(f_{Fe} + f_{Ni}) \qquad (5.18)$$

For FeNi A1 the positions of the atoms are random and an average of the atomic form factor is used: $f_{A1} = (f_{Fe} + f_{Ni})/2$. Then the structure factor for 001 and 002 reflections are:

$$F_{(001)} = 0 \qquad (5.19)$$

$$F_{(002)} = 4\left(\frac{f_{Fe} + f_{Ni}}{2}\right) = 2(f_{Fe} + f_{Ni}) \qquad (5.20)$$

The atomic form factors $f_{Fe}(Q, E)$ and $f_{Ni}(Q, E)$ have both energy dependence and angular dependence ($\frac{\sin\theta}{\lambda} = \frac{|Q|}{4\pi}$), and also a temperature dependence. This is where the temperature factor originates. The total expression for f is

$$f_{tot} = f_0(Q)e^{-M} + f' + if'' \qquad (5.21)$$

Values of f are tabulated; $f_0(Q)$ is found in e.g. International Tables for Crystallography [85] and Sasaki [84] gives f' and f'' in his tables. Both f' and f'' have a strong energy dependence as can be seen in figs. 5.6 and 5.7. Measuring diffraction at or close to the absorption edges will give enhanced contrast since the real part of f can be very large. In papers I and II this resonant x-ray diffraction was used. This energy dependence is also relevant in extended x-ray absorption fine structure (EXAFS) which was used in paper V. Here measurements are done with an x-ray energy at the absorption edge, while measuring the absorption for different energies.

Figure 5.6. The real and imaginary atomic form factors, f' and f'', of Fe as a function of energy, from Sasaki [84]. f' has a divergence at the K absorption edge (7120 eV) while f'' has a step here. The y-axis has been cut for clarity; minimum value of $f' \approx -17$.
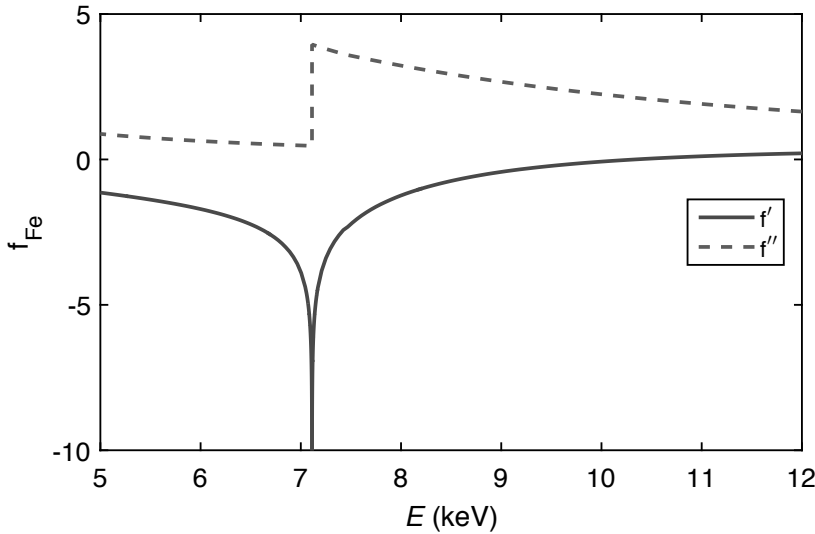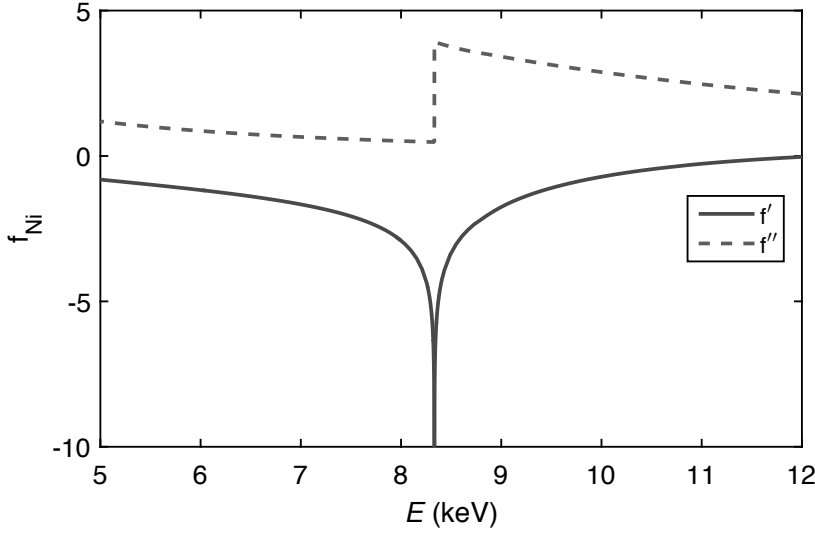
Figure 5.7. The real and imaginary atomic form factors, f' and f'', of Ni as a function of energy, from Sasaki [84]. f' has a divergence at the K absorption edge (8335 eV) while f'' has a step here. The y-axis has been cut for clarity, minimum value of $f' \approx -12$.

Equations (5.17) to (5.20) for FeNi tell us two things. First, for the disordered A1 phase there will be no 001 reflection, while the 002 reflection will have the same intensity as that of the $L1_0$ structure. This means the presence of a 001 reflection is an indication of the existence of $L1_0$ phase. Using tabulated values of f_0, f' and f'' for Cu K_α (8050 eV) in eqs. (5.17) and (5.18), the intensities can be approximated

$$I_{(002)} \propto \left|F_{(002)}\right|^2 = |2(17.378 - 1.2 + i3.2 + 19.365 - 3 + i0.5)|^2 \approx 4291 \tag{5.22}$$

while for the 001 reflection

$$I_{(001)} \propto \left|F_{(001)}\right|^2 = |2(22.197 - 1.2 + i3.2 - 24.344 + 3 - i0.5)|^2 \approx 30 \tag{5.23}$$

The 001 reflection will be about 143 times weaker than the 002. This means it can be very difficult to detect especially if the material is not fully ordered and there are A1 ordered parts. By instead measuring at the Fe resonance (7120 eV) the intensities become

$$I_{(002)} \propto \left|F_{(002)}\right|^2 = |2(17.378 - 6.7 + i3.9 + 19.365 - 1.7 + i0.6)|^2 \approx 3294 \tag{5.24}$$

$$I_{(001)} \propto \left|F_{(001)}\right|^2 = |2(22.197 - 6.7 - i3.9 - 24.344 + 1.7 - i0.6)|^2 \approx 248 \tag{5.25}$$

44

The 001 reflection will have about 8 times larger intensity if measuring at resonance while the 002 is still in the same order of magnitude. If there is disorder in the material the intensity of the 001 reflection will be decreased further and using resonant XRD might be required to detect the 001 reflection.

Temperature factor $e^{-2M(\theta)}$

The last term in eq. (5.2) is the temperature factor. The 2 in the exponent of the (Debye-Waller) temperature factor $e^{-2M(\theta)}$ comes from the square of F. M itself is also angle dependent and is given by

$$M(\theta) = \frac{8\pi\overline{u^2}\sin^2\theta}{\lambda^2} = \frac{-\overline{u^2}|Q|^2}{2\pi} \tag{5.26}$$

where $\overline{u^2}$ is the mean square displacement of the atoms which depends on the temperature.

Intensity of diffraction peaks from a single crystal measured at a synchrotron

Combining all equations from eq. (5.2) to eq. (5.26) we get the intensity for single crystal diffraction peaks when measured with synchrotron radiation:

$$I_{hkl} = SCF \cdot |F_{hkl}|^2 \cdot \frac{1}{\sin 2\theta} \cdot \left(1 - \exp\left(-\frac{2\mu t}{\sin\theta}\right)\right) \cdot e^{\frac{-16\pi\overline{u^2}\sin^2\theta}{\lambda^2}} \tag{5.27}$$

When rewriting in $|Q|$, the Jacobian must be multiplied and this becomes:

$$
\begin{aligned}
I_{hkl} &= SCF \cdot |F_{hkl}|^2 \cdot \frac{\left(1 - \exp\left(-\frac{2\mu t}{\sin\theta}\right)\right) \cdot e^{\frac{-16\pi\overline{u^2}\sin^2\theta}{\lambda^2}}}{2\sin\theta\cos\theta} \cdot \frac{\lambda}{4\pi\cos\theta} = \\
&= SCF \cdot |F_{hkl}|^2 \cdot \frac{\left(1 - \exp\left(-\frac{8\pi\mu t}{|Q|\lambda}\right)\right) \cdot e^{\frac{-\overline{u^2}|Q|^2}{\pi}}}{2|Q|\cos^2\left(\arcsin\frac{|Q|\lambda}{4\pi}\right)}
\end{aligned}
\tag{5.28}
$$

Knowing the theoretical value of the intensity I_{hkl} is necessary for calculations of the long-range order parameter S [82] which is used as a measure of the fraction of the structure composed of the L1$_0$ phase.

$$S = \sqrt{\left(\frac{I_{001}}{I_{002}}\right)_{\text{measured}} \cdot \left(\frac{I_{002}}{I_{001}}\right)_{\text{calculated}}} \tag{5.29}$$

Analysed volume

One factor which neither Cullity nor Birkholz deals with is the analysed volume. This becomes important for small angles, and for the background as will be seen in next section. It depends on two factors: the footprint and the depth, or actually path length through the film.

Footprint

The footprint is the area of the sample which is illuminated by the beam. The width of this area perpendicular to the beam $W_\perp$ is constant while the length along the beam depends on the slit width W_{slit} and varies with θ. Therefore the footprint is proportional to:

$$A_{fp} = \frac{W_{\text{slit}} \cdot W_\perp}{\sin \theta} = \frac{4\pi W_{\text{slit}} W_\perp}{|Q|\lambda} \qquad (5.30)$$

Path length

The path length through the film is depending on the depth of the film and the incident angle. For a smaller angle the beam must traverse a longer path in the film. This path length is the same as considered when deriving the expression for the absorption. The total length for a beam through the sample is the sum of the length down and up:

$$l_{tot} = l_{down} + l_{up} \qquad (5.31)$$

For symmetric diffraction the down and up lengths are equal. If the depth is z and the incident angle is θ the total length is

$$l_{tot} = \frac{z}{\sin \theta} + \frac{z}{\sin \theta} = \frac{2z}{\sin \theta} = \frac{z8\pi}{|Q|\lambda} \qquad (5.32)$$

Volume

The total volume which the beam probes is then

$$V_{probed} = A_{fp} \cdot l_{tot} = \frac{W_{\text{slit}} W_\perp}{\sin \theta} \frac{2z}{\sin \theta} = \frac{2z W_{\text{slit}} W_\perp}{\sin^2 \theta}$$
$$= \frac{2z W_{\text{slit}} W_\perp 16\pi^2}{|Q|^2 \lambda^2} \propto \frac{16\pi^2}{|Q|^2 \lambda^2} \qquad (5.33)$$

Compared to the attenuation factor this is a factor which gives intensity to the scan, i.e. this is the volume in which the beam can interact with the material.

5.4.2 Intensity in the background

A low intensity diffraction peak might be difficult to detect if there is much intensity in the background. Therefore decreasing the background intensity is usually advantageous. The background in a diffraction scan comes from many different sources. If we first consider the absorbed energy, this energy can do one of the following: it can heat up the sample, it can produce photo- or Auger-electrons, or it can be re-emitted as light. The last process is called fluorescence.

Fluorescence

The fluorescent light is emitted in all directions and will therefore create a continuous background in the diffraction scan. The fluorescence is energy dependent and it will create a characteristic spectrum with peaks at the energies of the atomic transitions which where excited, e.g. the K shell, see fig. 5.8. The excitations, and therefore the fluorescence spectra, depend on the incident energy. Transitions at energies below the energy of the incident light will fluoresce. E.g. a x-ray beam with an energy above the Fe K absorption edge incident on a sample containing Fe will cause fluorescence lines at the Fe K-edge energy.

The shape of the fluorescence background will depend on the volume of the sample which is analysed. The intensity will be dependent on angle and proportional to the absorption given by eq. (5.15).

By using an energy resolved detector the fluorescence can be removed by only measuring the elastically scattered light of the same energy as the incident light. But if the incident light is close to the fluorescence line there might be some overlap in energy, which has to be taken care of. In our measurements at ESRF in paper II we used an energy resolved detector for which we defined six regions of interest (ROI), one at each of the K_α-emission lines of Fe, Ni and Cu (ROI_{fluo}^{Fe}, ROI_{fluo}^{Ni}, ROI_{fluo}^{Cu}). The other three ROI were defined so that they included the regions where we scanned the energy ($ROI_{elastic}^{Fe}$, $ROI_{elastic}^{Ni}$, $ROI_{elastic}^{Cu}$), see fig. 5.8. There was some overlap of the K_β-emission lines into the $ROI_{elastic}^{Fe}$, $ROI_{elastic}^{Ni}$, $ROI_{elastic}^{Cu}$. But the following equations can be used to calculate the compensated intensities. For measurements at the Fe edge the intensity becomes:

$$I^{Fe} = ROI_{elastic}^{Fe} - I_\beta^{Fe} = ROI_{elastic}^{Fe} - ROI_{fluo}^{Fe} K_{\beta/\alpha}^{Fe} \qquad (5.34)$$

where $K_{\beta/\alpha}^{Fe}$ is the ratio of the intensity of the K_α and K_β fluorescence lines, since the K_β fluorescence line was inside $ROI_{elastic}^{Fe}$.

In the same way at the Ni edge we get:

$$I^{Ni} = ROI_{elastic}^{Ni} - I_\beta^{Ni} = ROI_{elastic}^{Ni} - I_\alpha^{Ni} \cdot K_{\beta/\alpha}^{Ni} \qquad (5.35)$$

$$I_\alpha^{Ni} = (ROI_{fluo}^{Ni} - I_\beta^{Fe} B) \cdot C = (ROI_{fluo}^{Ni} - ROI_{fluo}^{Fe} K_{\beta/\alpha}^{Fe} B) \cdot C \qquad (5.36)$$

where B is the ratio of the overlap of I_β^{Fe} into ROI_{fluo}^{Ni}

$$B = \frac{ROI_{fluo}^{Ni}}{I_\beta^{Fe}} < 1 \qquad (5.37)$$

B can be calculated from measurements of ROI_{fluo}^{Ni} and $I_\beta^{Fe} = ROI_{elastic}^{Fe}$ above the Fe edge but below the Ni edge when doing an energy scan over the Ni edge. This can be done for Ni-edge energy scans, but for energy scan around
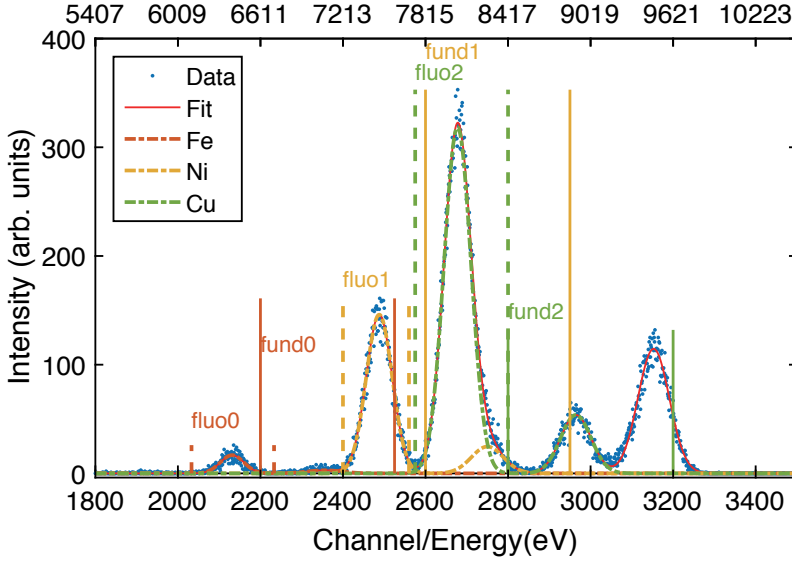
Figure 5.8. Fluorescence spectra: An example of the intensity vs energy measured by the detector. The incident energy was above the Cu K absorption edge, therefore the fluorescence peaks from Fe, Ni and Cu are all visible. The figure shows the definitions of the ROIs: fluo0=ROI^{Fe}_{fluo}, fluo1=ROI^{Ni}_{fluo}, fluo2=ROI^{Cu}_{fluo}, fund0=ROI^{Fe}_{fluo}, fund1=ROI^{Ni}_{fluo}, fund2=ROI^{Cu}_{fluo}. The different coloured lines are Gaussian functions fitted to each elemental fluorescence peak, these fits were used for calculating scaling factors.

the Cu-edge there is always fluorescence from the Ni, and B calculated from fits of the spectrum has to be used instead. C is a factor to compensate for the counts from the Ni α peak which are not covered by the limits of ROI^{Ni}_{fluo}:

$$C = \frac{I^{Ni}_{\alpha}}{ROI^{Ni}_{fluo}} > 1 \tag{5.38}$$

C was calculated by integrating ROI^{Ni}_{fluo} and I^{Ni}_{α} from the fits of the spectra in the figure and used for all measurements.

It was observed that there is some angle dependence of the factors B and $K^{Fe}_{\beta/\alpha}$. These values differed slightly from measurements at the 001 reflection, compared to the 002, 202 and 220 reflections.

For the Cu edge the following equations give the intensity

$$I^{Cu} = ROI^{Cu}_{elastic} - I^{Cu}_{\beta} - (I^{Ni}_{\beta} \in ROI^{Cu}_{elastic}) \tag{5.39}$$

$$I^{Cu}_{\beta} = I^{Cu}_{\alpha} \cdot K^{Cu}_{\beta/\alpha} \tag{5.40}$$

$$I^{Cu}_{\alpha} = \left[ROI^{Cu}_{fluo} - I^{Ni}_{\alpha}E - (I^{Ni}_{\beta} - (I^{Ni}_{\beta} \in ROI^{Cu}_{elastic})) \right] D \tag{5.41}$$

The constant D is a factor to compensate for the counts from the Cu α peak which are not covered by the limits of ROI^{Cu}_{fluo}. Like C it was calculated from the fits of the spectra in the figure and used for all measurements.

$$D = \frac{I^{Cu}_\alpha}{(I^{Cu}_\alpha \in ROI^{Cu}_{fluo})} \geq 1 \qquad (5.42)$$

for the second term $I^{Ni}_\alpha \cdot E$ in eq. (5.41), I^{Ni}_α is calculated as in eq. (5.36). E is the ratio of I^{Ni}_α which overlaps with ROI^{Cu}_{fluo} and is calculated from the scan in fig. 5.8.

$$E = \frac{(I^{Ni}_\alpha \in ROI^{Cu}_{fluo})}{I^{Ni}_\alpha} \ll 1 \qquad (5.43)$$

$I^{Ni}_\beta = I^{Ni}_\alpha \cdot K^{Ni}_{\beta/\alpha}$ as in eq. (5.35), and this term is also used for the final term

$$(I^{Ni}_\beta \in ROI^{Cu}_{elastic}) = I^{Ni}_\beta \cdot F = I^{Ni}_\alpha \cdot K^{Ni}_{\beta/\alpha} \cdot F \qquad (5.44)$$

Where F is in the same way as E a ratio of the overlap of I^{Ni}_β into $ROI^{Cu}_{elastic}$ and was calculated from the figure above.

$$F = \frac{(I^{Ni}_\beta \in ROI^{Cu}_{elastic})}{I^{Ni}_\beta} < 1 \qquad (5.45)$$

Now we have

$$
\begin{aligned}
I^{Cu}_\beta &= \left[ROI^{Cu}_{fluo} - I^{Ni}_\alpha E - (I^{Ni}_\alpha \cdot K^{Ni}_{\beta/\alpha} - I^{Ni}_\alpha \cdot K^{Ni}_{\beta/\alpha} F) \right] D \cdot K^{Cu}_{\beta/\alpha} \\
&= \left[ROI^{Cu}_{fluo} - I^{Ni}_\alpha (E + K^{Ni}_{\beta/\alpha} - K^{Ni}_{\beta/\alpha} F) \right] D \cdot K^{Cu}_{\beta/\alpha}
\end{aligned} \qquad (5.46)
$$

and finally

$$
\begin{aligned}
I^{Cu} &= ROI^{Cu}_{elastic} - \left[ROI^{Cu}_{fluo} - I^{Ni}_\alpha (E + K^{Ni}_{\beta/\alpha} - K^{Ni}_{\beta/\alpha} F) \right] D \cdot K^{Cu}_{\beta/\alpha} - (I^{Ni}_\beta \in ROI^{Cu}_{elastic}) \\
&= ROI^{Cu}_{elastic} - \left[ROI^{Cu}_{fluo} - I^{Ni}_\alpha (E + K^{Ni}_{\beta/\alpha}(1 - F)) \right] D \cdot K^{Cu}_{\beta/\alpha} - I^{Ni}_\alpha K^{Ni}_{\beta/\alpha} F
\end{aligned}
$$
$$(5.47)$$

In fig. 5.9 eq. (5.35) has been applied to calculate the elastically scattered light I^{Ni} for an energy scan over the Ni K absorption edge at a fixed $|Q|$ which equals the position of the 001 reflection. The intensities in all the ROIs are shown. The fluorescence of Fe is constant since we are above the Fe absorption energy, while the fluorescence of Ni shows the shape of the absorption edge. $ROI^{Fe}_{elastic}$ seems to follow the Ni fluorescence since these ROIs are overlapping. As can be seen the background step is removed from I^{Ni}, and it shows that the reflection goes through a maximum in intensity at the edge.
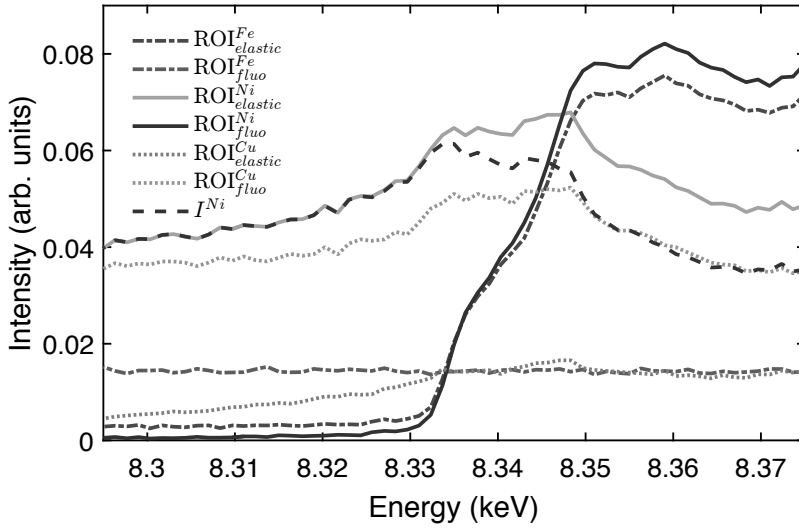
Figure 5.9. An example of an energy scan at fixed $|Q|$ at the 001 reflection. The incident energy is scanned over the Ni K absorption edge, therefore there is fluorescence from Fe and Ni. The intensities in the six ROIs are shown as well as the fluorescence compensated inelastic signal I^{Ni}.

When compensating the intensity of a diffraction scan for the fluorescence using eq. (5.34), eq. (5.35) or eq. (5.39) as can be seen in fig. 5.10, it seems this compensation does not do much to the background. There is still a background which is angle dependent. The fluorescence has also a slight angle dependence but the slope is different compared to the elastically scattered intensity. The amount of fluorescence is depending on the absorption in the material, and therefore is should have the same $|Q|$ dependence as eq. (5.15). In fig. 5.10 is shown a fit of this equation which indeed fits well to the Fe fluorescence (ROI_{fluo}^{Fe}). This means there is still some other background in the elastically scattered light, which follows another $|Q|$ dependence.

Modelling the background

To be able to fit the diffraction peaks a background has to be included. In text books (e.g. [83, 82]) it is only stated that it is important to include a background to achieve a good fit, but the shape of this background is often not given. The background from the fluorescence has been removed and what remains is an elastically scattered background. I have found that a background of the shape

$$I_{bkg} = n_1 + \frac{n_2}{|Q|^2} \tag{5.48}$$

where n_1 and n_2 are fitting parameters, works well. An example of a fit using this equation is seen in fig. 5.11, which shows that it works well, even up to
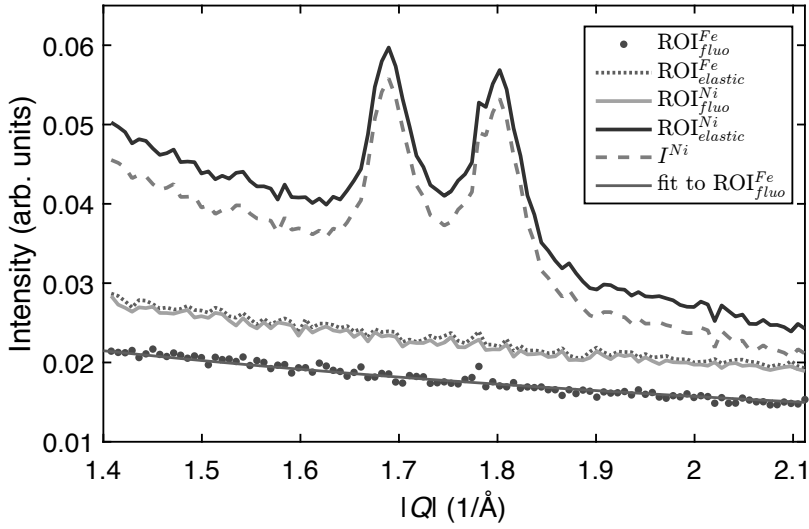
50

Figure 5.10. An example of a $|Q|$-scan over the 001 reflection. The intensities for the different ROIs are shown. The incident energy is at (8335 eV) which is just at the beginning of the Ni K absorption edge, and therefore there is fluorescence from Fe and some from Ni. The background slope of the elastic scattered intensity I^{Ni} is different from that of the fluorescence ROI_{fluo}^{Fe}. A fit of ROI_{fluo}^{Fe} using the expression for the absorption is also shown.

high angles as can be seen in in figure 3 of paper II. But there is the question if this shape can be motivated. An argument could be like this: the background might come from diffuse scattering, e.g. disorder, dislocations imperfections, etc. If it is assumed this disorder is homogeneous throughout the sample, then the scattered intensity will be proportional to the volume which the x-ray beam has probed and eq. (5.33) which describes this volume has the same $1/|Q|^2$ dependence. The constant term n_1 represents a homogeneous angle independent background, which would then be from many different sources such as electronics. But usually this term becomes quite small when fitting.

Another way of looking at this would be that the intensity has the same angle dependence as the diffraction peaks. Then it should scale with the Lorentz factor and also by the geometry factor if we assume it originates from disordered grains. However this is more difficult to motivate since the Lorenz factor describes the angular dependence over which coherent diffraction occurs, whereas we now are discussing non-coherent scattering. But still this expression includes both a depth and a footprint dependent part. By combining the

51
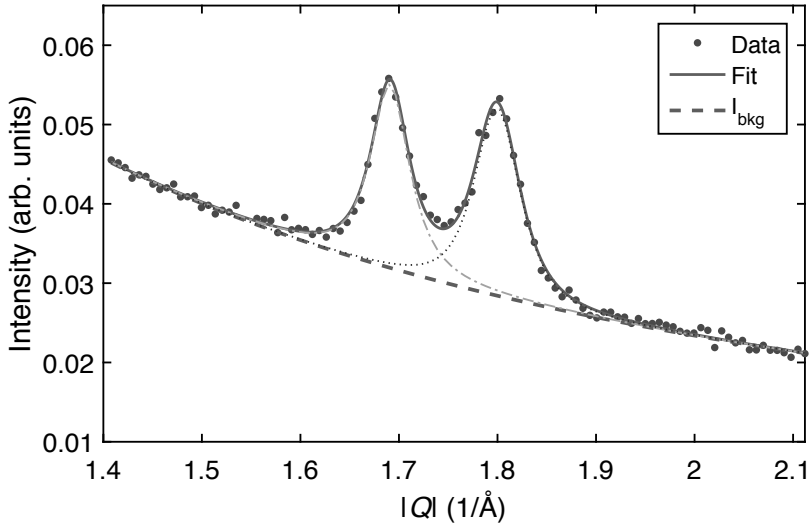
Figure 5.11. A $|Q|$-scan over the 001 reflection acquired with x-rays of energy just be-low the Ni-edge (8335 eV). A fit of the peaks and a background modelled by eq. (5.48) is very good. The peaks are fitted by two Pearson7 functions [83] and the individual fits of the peaks are also shown.

Lorentz and geometry factors it looks like

$$I_{bkg2} \propto \frac{1}{2 \sin\theta \sin 2\theta} = \frac{1}{4 \sin^2\theta \cos\theta} =$$
$$= \frac{4\pi^2}{|Q|^2 \lambda^2 \cos\left(\arcsin\frac{|Q|\lambda}{4\pi}\right)} \tag{5.49}$$

For small angles the $\cos\theta \approx 1$ and this can be approximated to

$$I_{bkg2} \approx \frac{4\pi^2}{|Q|^2 \lambda^2} \tag{5.50}$$

which is close to the same expression used for fitting. A third possibility is that the angle dependence comes from the atomic form factor $f_0(Q)$, but this has not been tried.

5.5 Composition modulations and the importance of controlling the composition

XRD measurements on our samples reveal a symmetrically split peak centred around the expected 001 position, see figs. 5.11 and 5.12. We could see this split for most samples but with variations in the peak separation Δq. It can be explained by a model in which the deposition rates of either one or both magnetrons deviate slightly from the nominal 1 ML/layer repetition. This will cause a composition modulation in the layers of the film with a periodicity ($\Delta d = 2\pi/\Delta q$) which depends on the deposition rate deviation and hence also the total composition, see fig. 5.13. The basic idea is the following: suppose the deposition rate of Fe is too high and more than 1 ML is deposited per layer repetition. When then the next layer of Ni is deposited there will not be room for all the atoms in this layer, and some Ni atoms will then end up in the third layer. When the third layer is deposited with again a too much Fe, there are already Ni atoms in this layer and even more Fe atoms will end up in the fourth layer. In this way the amount of excess atoms will accumulate until an extra layer of Fe is formed. This layer is then an Fe layer but in a position which should have been a Ni layer according to the original stacking, meaning there is a phase shift of π in the stacking sequence of the layers. They are then anti-phase relative each other, and the next Ni layer is also in the wrong position. With the following Fe layer the next composition modulation period is started. The use of "composition" here refers to each atomic layer, as depicted in fig. 5.13, and the modulation is in Fe and Ni content of each layer. This is explained in more detail in Paper I.

5.5.1 A simplified analogy to radio technology

To explain the appearance of the split diffraction peak we can use an analogy to radio technology, and the concepts of amplitude modulation (AM). The left panel in fig. 5.14 depicts an amplitude modulation of a carrier sinus signal in real space. The carrier signal should be seen as the atomic lattice planes and the position corresponds to the depth in the film. For the amplitude we are here making the analogy to the atomic form factor, or scattering factor, which depends on the composition and is varying between 100 % Fe or Ni. In the right panel of fig. 5.14 the corresponding spatial frequencies are shown, and the analogy is that the spatial frequency corresponds to $|Q|$.

As can be seen an amplitude modulation causes a split frequency peak without any central peak in the same way as the 001 reflection was split. The negative sign of the modulating signal causes a phase shift in the resulting signal which is seen in fig. 5.14 left panel, meaning that Fe and Ni have changed the stacking order e.g. there are Ni atoms where there should be Fe atoms, as in fig. 5.13. The absence of a central peak can be seen as due to this phase shift, which causes destructive interference.
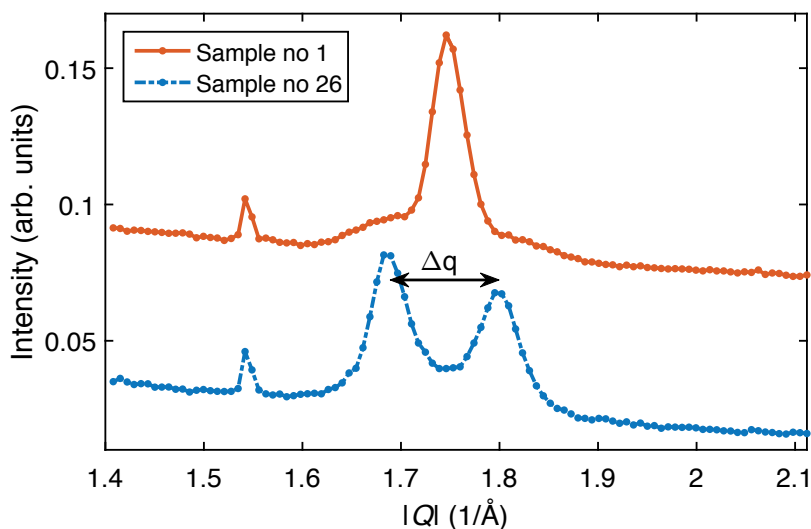
Figure 5.12. Diffraction scan over the 001 reflection for two samples grown using the same procedure. Sample no. 1 was grown first in the batch, while sample no. 26 was grown last in the batch. A drift in the sputtering rate of the magnetrons has caused a composition modulation in sample no. 26, which is seen as the split 001 reflection with peak separation Δq.
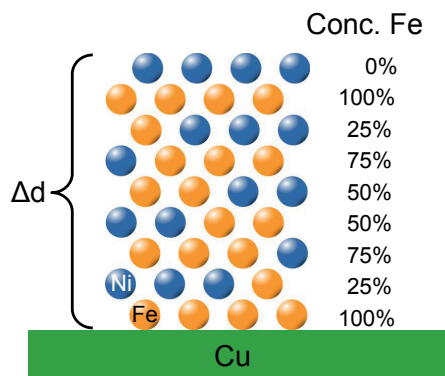
Figure 5.13. Schematic showing the composition modulation period Δd, if the deposition rate of Fe is 1.25 times the ideal value. The total composition would here be 56 at.% Fe.
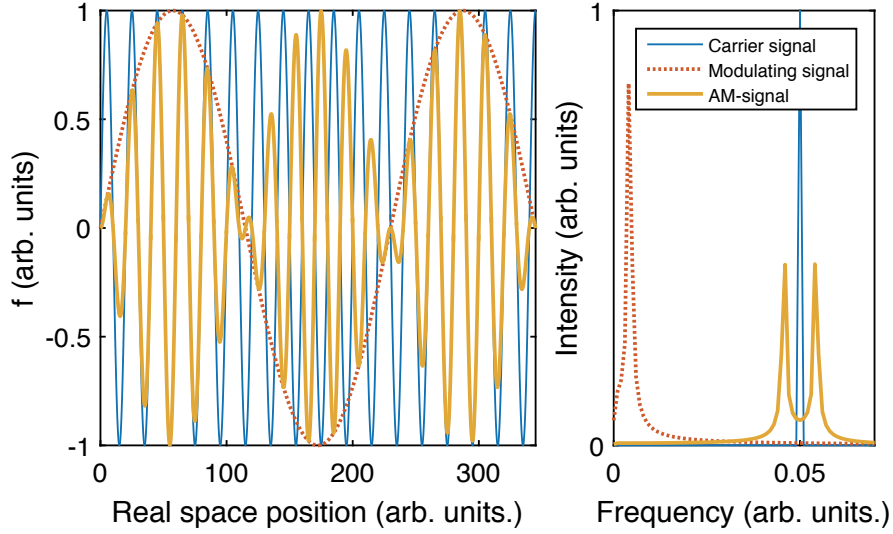
Figure 5.14. Left: An amplitude modulated signal in real space, where the thin line is the carrier signal, dotted is the modulation signal, and the thick line is the resulting AM-signal. Right: The corresponding frequencies of the three signals. The amplitude modulated signal has two frequencies, symmetrically split around the carrier frequency, without any central peak. Our 001 reflections are comparable to this AM modulated signal.

Since the atomic form factor in reality changes stepwise from layer to layer and does not have negative values, a better model is made by representing the atoms as a square wave plus a constant offset. A simulation of this can be seen in fig. 5.15, which shows there is still a split peak at the position of the lattice peak (carrier signal). The effect of the discrete steps gives some higher harmonics, i.e. satellites at higher frequencies.

The $L1_0$ is the extreme case of a superlattice, with the bilayer length of only two atomic layers. Therefore it is now interesting to note the difference of diffraction patterns to a "standard" superlattice in a multilayer with thicker layers, where there is always a central peak, which we do not see for the composition modulated structure. The simulated frequencies of a 4/4 ML structure, as was studied in Paper III, can be seen in fig. 5.16. The central peak corresponding to the lattice parameter is seen as well as satellites due to the bilayer. The origin of these satellites is different from the split peak of the composition modulation. The satellites are due to the higher harmonics caused by the square wave pattern of the atomic form factor in the multilayer.

This is a very simplified model to visualise the concept of the composition modulation. A more correct model was made with actual atomic form factors of Fe, Ni and Cu. The resulting simulations are shown in Paper I and the pattern has good correspondence to our diffraction data.
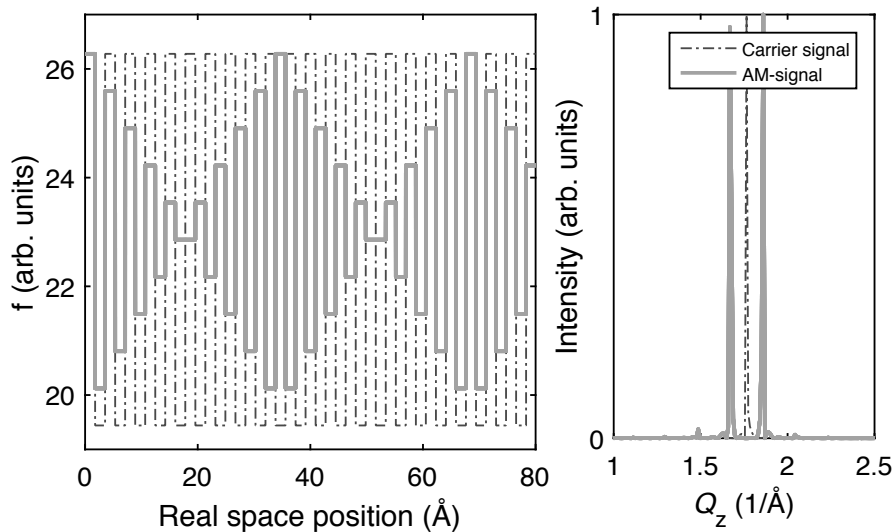
Figure 5.15. Left: A more realistic model using a shifted square wave for the carrier, and a triangular wave as amplitude modulation. The real atomic distances have been used. Right: The corresponding frequencies with a split peak, at the same $|Q|$ as in measurements. Due to the use of a square wave some higher order frequencies appear.
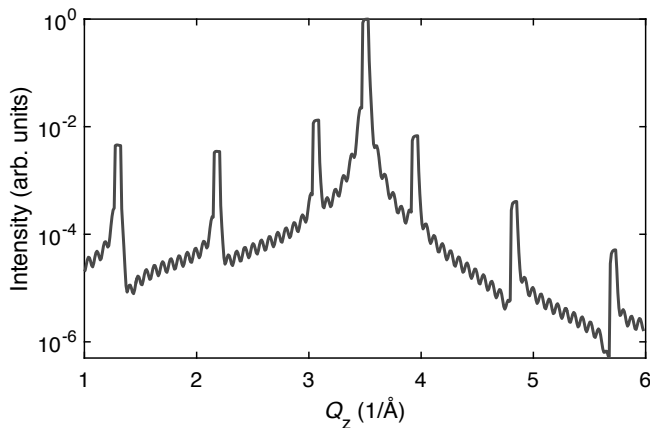
Figure 5.16. Simulation of the spatial frequencies from a 4/4ML Fe/Ni multilayer. The satellites due to the bilayer are seen.

Here is the place to come back to the surface roughness discussed in section 5.3. If we first assume there is no composition modulation, but there is an atomic step on the buffer surface, the consequence would be that parts of the film are 1 ML out of phase, i.e. anti-phase compared to the rest. If these different parts of the film are within the x-ray coherence length there will be

destructive interference. Such anti-phase domains would in an ideal case result in that a (almost) perfect $L1_0$ film with one atomic step would give no intensity at all in the 001 reflection. But if there are composition modulations, the atomic step will not cause all of the film to be anti-phase, and the consequence would be only a decrease of the intensity. From one point of view the existence of these composition modulations is helpful when measuring 001 reflections. But the roughness is also causing chemical disorder and it can be viewed as parts of the film being A1 phase.

5.5.2 The peak separation Δq and its relation to order

The presence of composition modulation means that the chemical ordering of the material is not good. Normally the long range order parameter S, eq. (5.29), is used as a measure for the ordering. It requires the integration of the peak intensity, but for a sample with composition modulations this integral will not be well defined, and it will not be a good measure. Therefore we have not used it for our studies. For samples with composition modulations a better measure of the chemical order is the size of Δq (or Δd). A small separation in Δq means the composition modulation is long, the shift of atoms is small in each layer and it takes many layers for the structure to repeat. Such a sample then has a better order than one with a large Δq, where there are many atoms in the wrong layer and the phase will rather be the disordered A1 phase. Therefore Δq is a measure of the amount of disordered phase in the material.

The composition modulation period should have a dependence on the total composition. More excess atoms in each layer will give a shorter composition modulation period. If the saturation magnetization M_S is assumed to be proportional to the composition according to the Slater-Pauling curve for a mixture of Fe and Ni [86], then the composition can be estimated from M_S. According to this method the samples for Paper I contain less Fe than the nominal 50 %, whereas they are moving away from 50 % towards more Fe for the samples of Paper II. The samples with the composition closest to the nominal value also had the longest composition modulation period (smaller Δq), as expected, see fig 10 of Paper I. When plotting the composition versus amount of accumulated deposited material, for the samples of Paper II (see fig. 5.17) it can clearly be seen that the sputtering rates of the targets have been drifting over time. A similar increase of Δq seems to be present throughout the sample series.

Even though the presence of a split peak means there is chemical disorder in the material, this is not only bad when growing FeNi $L1_0$. Since we know the split is roughly proportional to the composition, by measuring the 001 reflection with in-house diffraction, we can fine-tune the deposition times to minimize Δq. Measurements of the 001 reflection with Cu K_α radiation have been proven possible. This radiation has an energy between the Fe and Ni
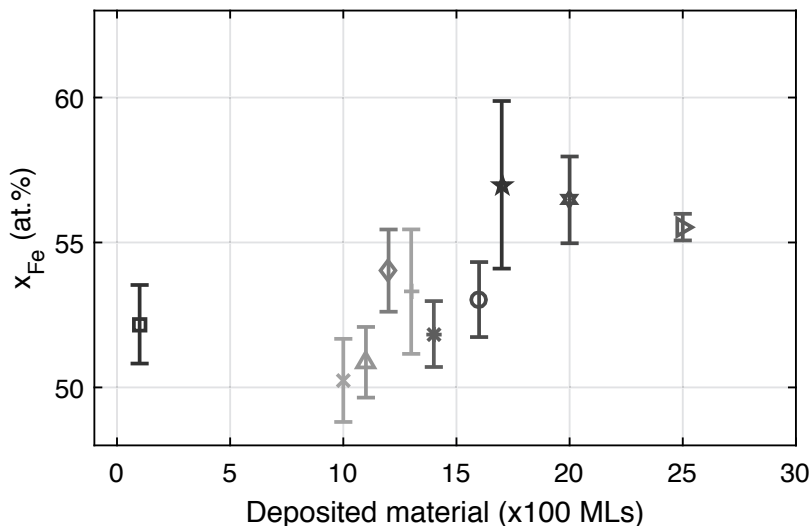
Figure 5.17. The Fe composition estimated from the saturation magnetization M_S versus accumulated deposition time for the sample series in terms of numbers of hundreds of FeNi bilayers deposited, (i.e. roughly the sample number). This data is for the series grown on CuNi/Cu buffers. There seems to be an increase in Fe content, showing there is a drift in the sputtering rate over time.

absorption edges and there is actually a difference in the scattering factors, but the signal to noise ratio is still very small and a detector which can discriminate the Fe fluorescence must be used. Still the counting time required is quite long (typically 12 h), but acceptable. Such a tuning was performed before the first sample of Paper II was deposited, with excellent results.

This section has shown the importance of controlling the composition when growing thin films by sputtering. Even if the composition can be tuned accurately at one point, using one rate calibration in the beginning of the growth of a series of samples is not enough. It is obvious that the rate must be monitored and calibrated regularly throughout the entire period of growing samples. Otherwise the first and final samples can not be assumed to be comparable.

5.5.3 Successful fabrication of FeNi L1$_0$

Our first results on FeNi L1$_0$ fabricated by the procedure described in this chapter are presented in Paper I. Below is a summary.

Question:
- Is it possible to fabricate FeNi L1$_0$ by sputtering onto Si(001) substrates?

Results:

- FeNi in the $L1_0$ structure is possible to grow by sputtering onto Si(001) substrates. But in these first experiments there was a high degree of chemical disorder and the fraction of well ordered material was very small.
- Even with a well-ordered crystalline structure the chemical order was not guaranteed with our method.
- The FeNi layers were under tensile in-plane strain with $c/a < 1$.
- By resonant XRD, it was possible to qualitatively measure and to some degree quantify composition modulations, which are connected to the total magnetization and originate in deviations in deposition rates. For future successful growth using our method it is important to keep track of and compensate for any drift in the deposition rates.
- Using a simple simulation model of XRD we qualitatively explained the shape of diffraction patterns and how they depend on different aspects of the chemical ordering which can appear in this thin film system.
- The surface of the Cu buffer layer was found to be very important, and the roughness of the surface affected the chemical order.
- The saturation magnetization was close to expected values.
- The magnetic uniaxial anisotropy energy was very small due to both the roughness induced chemical disorder and the tensile in-plane strain.

5.6 In-plane strain and c/a

In Paper II we improved the growth method further, by using different temperatures and sputtering rates compared to Paper I. In the samples for Paper I there was a tensile in-plane strain compared to ideal $L1_0$ values and the tetragonal structure was inverted, $c/a < 1$. If this was hindering the correct $L1_0$ formation a strain close to the nominal might help the growth. Theoretical calculations by Miura [87] had predicted that K_U should vary with strain, but a systematic experimental comparison had not been done. Therefore in this article we applied varying in-plane strain to FeNi $L1_0$ films in a systematic manner. The in-plane lattice parameter was varied by using CuNi buffers of different composition. The questions and results of Paper II are given below.

Questions:

- With our method, is it possible to grow FeNi $L1_0$ with better chemical order compared to our previous study?
- Does a correct in-plane lattice parameter of the buffer layer promote formation of the wanted $L1_0$ structure in the FeNi layer?
- Is the magnetic uniaxial anisotropy of FeNi in the $L1_0$ structure possible to change by an in-plane strain, as theoretical calculations have predicted?

Results:

- By more careful control of all growth parameters the FeNi $L1_0$ could be grown without any composition modulation.
- c/a can be controlled in a FeNi film by the in-plane lattice parameter of the underlying buffer. We achieved an overall $\pm 2\%$ variation in c/a.
- The correct lattice parameter might promote the $L1_0$ formation, but the effect of composition modulations interferes and seems to be overshadowing other effects. It is not possible to draw conclusions for certain.
- There is not a perfect in-plane lattice match of a_{FeNi} to a_{CuNi}. The deviation increases with the difference from the nominal $L1_0$ strain, and some partial relaxation occurs.
- A dependence of K_U on c/a can not be seen. But in the region of acquired c/a the predicted variation is within our measurement uncertainty. Larger K_U values, $\sim 0.35\,\text{MJ}\,\text{m}^{-3}$, were achieved compared to Paper I.
- A 110 reflection, which is due to $L1_0$ ordering with the c-axis out-of-plane, is present in the in-plane diffraction scans. This 110 reflection is not split and was observed for samples with a split 001 reflection, showing that the composition modulation is an effect in the out-of-plane direction. It further strengthens our model of the origin of composition modulations and the formation of the split 001 reflection and confirms that the peak separation Δq is linked to the total composition and the deposition rate.

5.7 Fe/Ni multilayers

The original goal of Paper III was an investigation of the resolution of depth profiling XPS, but some interesting magnetic properties were measured as well. XPS had been used to investigate the diffusion between the layers, but the results indicated very large interface regions or diffusion, see fig. 5.3. The depth resolution also inhibited us from measuring the monolayer variation in compositions in the FeNi $L1_0$ samples. We were curious about how thin layers can be measured. We also wanted to have a measure of the roughness and the intermixing of the Fe/Ni layers, hoping this could help explain the weak K_U in our $L1_0$ samples. Therefore we deposited symmetric Fe/Ni multilayers, $(d_{Ni} = d_{Fe})_N$, by the same technique as for Paper II, but with layer thicknesses of $d_{Ni} = 4, 8, 16, 32$ and $48\,\text{ML}$. We hoped to be able to extrapolate their interface width down to the 1 ML structures. The paper is summarized as follows.

Questions:

- What is the spatial resolution of the depth profiling XPS and TEM?
- What happens when the Fe/Ni layers are thicker than 1 ML?
- What is the roughness and/or intermixing of the Fe and Ni layers?

Results:

- The depth resolution of XPS is according to literature a bit larger than $12\,\mathrm{ML} \approx 22\,\mathrm{\mathring{A}}$ but in our thin films system structures down to 8 ML can be hinted. Care must be taken when XPS is used to investigate these thin structures.
- The layering is very good and elemental layers can be observed by TEM measurements down to at least 4 ML thickness.
- The epitaxial fcc (001) structure is maintained up to 8 ML but for thicker Fe layers they relax to (110) bcc orientation. The overlying Ni layers then change orientation to the close packed (111) orientation.
- Magnetic measurements indicate there is pure fcc Fe layers in the 4 ML multilayer, and to some part also in the 8 ML multilayer. Since the magnetic signal from Fe is lost for these thicknesses, we conclude that layers must be anti-ferromagnetic fcc Fe as has been seen by others [88, 89, 90].
- It was difficult to separate roughness, intermixing and diffusion at the Fe/Ni interface. But by electron energy loss spectroscopy, the intermixed interface width can qualitatively be estimated to not more than 8 ML, which equals about 13 Å.

5.8 Conclusion and further improvements of the synthesis

The purpose of synthesizing the FeNi $L1_0$ phase was to achieve the proposed good magnetic properties: a high magnetization and a strong uniaxial anisotropy. We achieved the magnetization value but this was fairly easy since it mainly depends on the overall composition. We could not reach the uniaxial anisotropy energy which we hoped for. But there are still parts of the synthesis that can be improved. As was seen in Paper I the chemical disorder is the most probable cause for the destroyed magnetic uniaxial anisotropy. Even when the in-plane strain and c/a ratio are correct, and there is no composition modulation as in Paper II, there is still a reduction in K_U compared to expected values.

Still it is very important with a correct composition. The deposition rates must be correct and this is something which we now know how to compensate for. The initial offset in deposition rates between Fe and Ni can be determined by either measuring the 001 peak separation or the composition. The deviation over time can be compensated for by e.g. monitoring the peak separation and/or measuring, and keeping track of, the deposition rate drift.

To achieve higher K_U values the main point which remains to optimize is the buffer layer. The roughness should be minimized while keeping the correct lattice parameter and good crystalline order. First, a more reliable quantifiable measure of the roughness must be used. After this there are many parameters

to tune and there might be a better combination of thicknesses, temperatures and annealing times. A more thorough investigation than there was time for in this work would be needed.

Other alternatives for a buffer layer have been considered. One option is a CuAu buffer [91] but Au is expensive, which is why we avoided using it. Another possibility which was considered, but was never tested since there was not enough time to rebuild the equipment, is to anneal Cu in a hydrogen atmosphere. This has been reported to improve the crystalline quality and surface structure of Cu [92, 93], and should be done in-situ before deposition of the Fe/Ni layers. Yet another idea is to grow buffers with an out-of-plane composition gradient. A buffer layer could then be grown which starts as a Cu film but ends as a CuNi film. It might then be possible to facilitate the strain relaxation of the film through the composition rather than introduction of dislocations.

Part II:
Combinatorial sputtering

6. The combinatorial sputter system Sleipnir

The combinatorial approach to materials science is a combination of different ways of quickly creating many samples and in a fast and structured way analyse them [94, 95]. When the dependence of material properties on composition shall be studied many samples, each with a different composition, have to be deposited. This is a lengthy and repetitive procedure and a compromise choosing what compositions to investigate has to be made. The time can however be shortened dramatically by employing a combinatorial technique where samples with continuous gradients in composition and/or thickness along the sample surface are fabricated. Such a sample can be fabricated in one deposition session equal to the time of one ordinary sample. Any arbitrary composition, within the range of the sample, can subsequently be selected for analysis by simply measuring at the corresponding position on the sample.

We have built a UHV sputtering system with four magnetrons capable of depositing such gradient samples. This combinatorial sputter system, named Sleipnir, will be described in this chapter. A model to simulate the combinatorial growth will also be presented, and finally some examples of the system capabilities are given.

6.1 Instrument features

An image of the sputter chamber can be seen in fig. 6.1 and a schematic can be seen in fig. 6.2. The sputter chamber is built for UHV conditions. It is pumped by a $300 \, \mathrm{l s^{-1}}$ turbo-drag pump backed up by a variable speed membrane pump, which allows for an almost totally oil free system. To maintain a good vacuum and minimize pumping times the chamber has a load lock which is separated from the main chamber by a high vacuum valve. The load lock is pumped separately by a $30 \, \mathrm{l s^{-1}}$ turbo-drag backed up by another variable speed membrane pump.

The system has a normal base-pressure at around 1.5×10^{-9} torr, after 2 days of baking. By sputtering oxygen pumping materials such as Ti or Zr on the walls in the chamber a base pressure of 5×10^{-11} torr has been reached.

The sputtering gas, Argon, is introduced into the chamber through four valves located next to each magnetron. With these valves the flow of gas over each magnetron can be turned on or off individually. The total flow to all magnetrons of the sputtering gas is controlled by a Mass Flow Controller (MFC) which is located upstream from the four valves and their manifold.
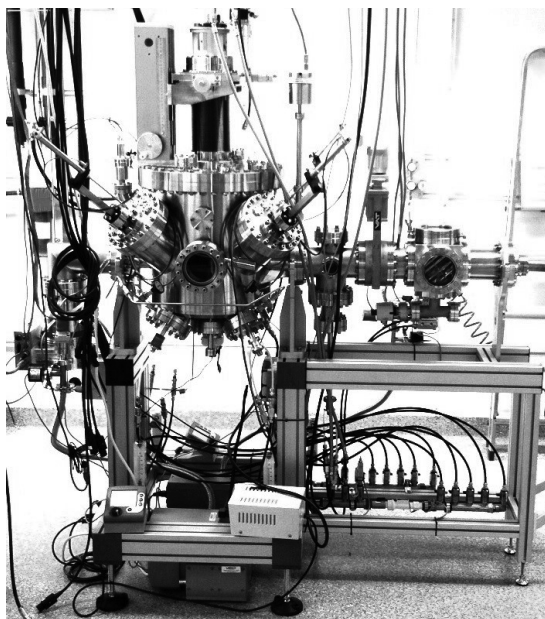
Figure 6.1. Sputter chamber, with the water cooled sample manipulator.

This mass flow controller has a range from 0-20 sccm and is calibrated for Ar. An extra inlet for gas is located on the side of the chamber, and this inlet is used for reactive gases, O_2 and N_2. This gas inlet has valves to select gas and individually MFCs calibrated for O_2 or N_2 with ranges up to 10 sccm. Typical sputtering pressures used in the system are in the range 1 mtorr to 10 mtorr, where the higher range has been used during reactive sputtering.

The pressure and pumping speed can be controlled by a butterfly style throttle valve on the exhaust, which can be set continuously from fully open to almost closed. This is needed to allow a small gas flow but still maintaining a high sputter pressure.

The system has four MightyMAK magnetrons (sold by ScoTech Ltd) with a target size of 3 inches. The targets are each held by a magnet which also serves as the provider of the magnetic field for trapping electrons close to the target. On non-magnetic targets a target holder disk of iron has to be screwed to the back.

Shutters covering the magnetrons can be controlled individually by an electronic controlling unit which is also connected to a computer. Through a LabView software the timing for opening and closing of individual shutters can be controlled. Entire deposition programs can be created and run. With this software it is possible to automatically deposit multilayer systems. The time resolution for this control is 0.1 s.

Two options of sample holder manipulators are available. The first one has the benefit of water cooling which enables quicker cool down after heating,
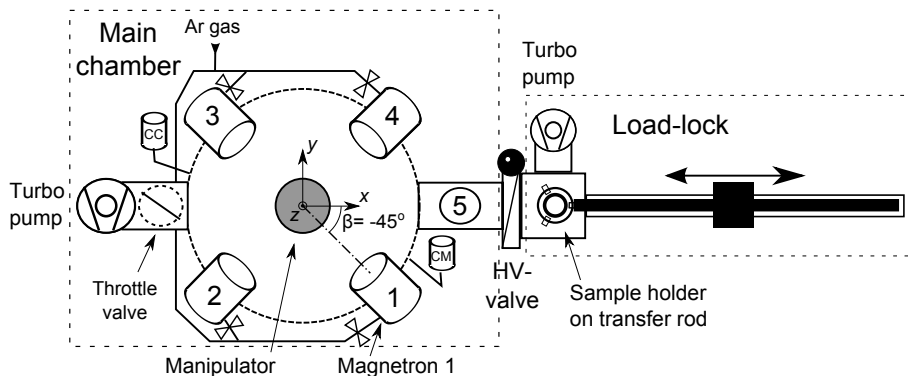
Figure 6.2. Top view schematic of the chamber and its different parts: main chamber, load lock, high vacuum (HV) valve, magnetrons (which are numbered 1 to 5), manipulator, throttle valve, gas inputs, transfer rod, turbo pumps, cold-cathode gauge (CC), capacitive manometer gauge (CM). The definitions of the coordinate system for calculations are marked. The origin is set to the focus point of the magnetrons. The angle β is also defined.

whereas the second manipulator lacks this feature. The second manipulator instead has the capability to provide both DC and RF biasing on the substrates. This RF biasing can be used to sputter clean the substrates. DC-biasing is used to control the energy of incident ions during film growth.

When depositing gradient samples, both thickness and composition depend on where the sample is situated relative to the magnetrons. This will be explained further in coming sections. To give more freedom when depositing such samples the sample manipulators have a *xy*-movement capability of $\pm 12.5\,\text{mm}$ (first manipulator), or $\pm 19\,\text{mm}$ (second manipulator) in each direction, see fig. 6.2. This can be useful e.g. if the deposition rate from one magnetron is too high and the power can not be changed to modify the rate, then the substrate could instead be moved slightly off axis. In this way the focus point will be moved on the sample surface. The manipulators also have *z*-movement which can change the height from $-92\,\text{mm}$ to $100\,\text{mm}$ relative to the centre position, with some restrictions in the *xy*-movements at the end points, see fig. 6.3. This can move the sample in and out of focus, which will change the thickness and composition profile. In the next section this will be explained and examples are given in section 6.3.

The sample manipulators have heaters which can heat the substrate up to $1000°\text{C}$. The temperature of the substrate is measured by a thermocouple located between the heater and the sample holder.

To allow for deposition of uniform samples without gradients the manipulator has the capability to rotate. At a sufficiently high rotation speed each point on the sample will in average spend the same time at a specific distance from each magnetron. If the deposition rate is linear with distance the deposition

should be homogeneous. If it is not, which is the real case (see section 6.3) there will be a slight radial variation. Both manipulators have a maximum rotation speed of 60 rpm.

Substrates are mounted on sample holders which are then loaded onto the sample manipulator by the transfer rod. The standard sample holder can hold 3 inch (≈ 76.2 mm) diameter wafers, which is the maximum size for the system. Modified versions can hold smaller wafers or pieces of substrates. One geometry in particular is adapted for holding 60 mm strips with special clamps. Another geometry has clamps to hold rods for tribology tests. There is also a special holder for $50 \times 50 \times 10$ mm^3 substrates usually used for neutron diffraction experiments. Further, there is one special holder that contains two magnets, creating a magnetic field of about 130 mT parallel to the substrate surface, which should have the shape of a 60 mm strip. This one was used in paper IV.
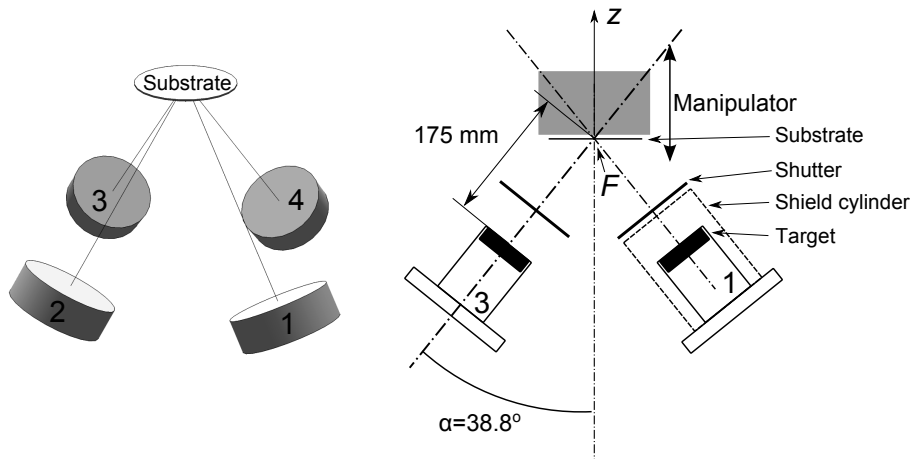
6.1.1 Deposition geometry

The geometry of the sample and the four magnetrons can be seen in figs. 6.2 and 6.3. The four magnetrons are located at an angle of $\alpha = 38.81°$ relative to the sample surface normal. They are distributed symmetrically at 90° from each other around the central vertical z-axis of the system, see fig. 6.2. The intersection of the normal of the magnetron targets will be referred to as the focusing point (F). When the sample centre is in the focus of the four magnetrons the distance from target surface to sample is 175 mm. We define a coordinate system with the origin in the focus point, the x-axis pointing along the long centre axis of the system and the z-axis pointing in the vertical direction with the positive direction upwards, fig. 6.2. In this coordinate system the location of the magnetrons are given in table 6.1.

Table 6.1. *Coordinates of the four magnetrons, see fig. 6.2 and fig. 6.3 for definitions.*

Magnetron k	x (mm)	y (mm)	z (mm)	In-plane angle β (°)
1	77.62	−77.62	−136.47	315
2	−77.62	−77.62	−136.47	225
3	−77.62	77.62	−136.47	135
4	77.62	77.62	−136.47	45

Films with gradients in thickness can be deposited in this geometry. By co-sputtering from two or more targets a gradient in both composition and thickness will be created. At each point the depositions from each magnetron will contribute to the total thickness. Since the materials are deposited at the same time they will be mixed and a material with a specific composition is

Figure 6.3. Sputter chamber geometry. Left: a schematic in perspective view showing the position of the four magnetrons relative to the substrate. Right: A cross-section of the chamber at $\beta = -45°$, (see fig. 6.2 for definition of this angle). Magnetrons 1 and 3 are in the plane of the cut, their angle relative to the vertical is marked and the target to focuspoint distance is indicated. The different components of the magnetron are marked. Also the focus point F is marked which is the origin of the coordinate system.

deposited at this point. In this way up to a quaternary "phase-diagram" can in principle be mapped on a single sample.

6.2 Modelling the sputtering chamber

The ability to simulate the composition and thicknesses in a deposited thin film can be useful as well as time saving when planning experiments. In this section a model for how the composition and thickness can be calculated is presented. These calculations are implemented in a MATLAB script which is included in Appendix A. In the section after this examples of calculations will be presented and compared to measurements.

6.2.1 Combinatorial deposition rate

For a combinatorial sputter system with m magnetrons the total deposition rate $\Phi(P)$ in atoms/(area$\times$time) at a point P on a substrate depends on the sum of the rates from each magnetron,

$$\Phi(P) = \sum_{k=1}^{m} \Phi_k(P) \tag{6.1}$$

If we have such a low pressure that the mean free path is longer than the chamber dimension we can assume straight paths of sputtered particles. Then the rate from magnetron k can be given as eq. (6.2).

$$\Phi_k(P) = A_k \frac{\cos\theta \cos\varphi}{\pi |\bar{\mathbf{r}}_k(P)|^2} \tag{6.2}$$

This rate depends on the geometrical variables defined in fig. 6.4 and in this following text. The dimensions of the deposition rate is given in atoms/(surface area$\times$second). Here I will assume an infinitesimal area i.e. a point, and the rate is given for each point. With the model presented here three effects are taken into account. Firstly, the rate will decay with the reciprocal of the square of the distance from the source $|\bar{\mathbf{r}}_k(P)|$. Secondly, the rate will have a cosine dependence on the receiving angle θ which is the angle between the substrate surface normal (parallel to $\bar{\mathbf{z}}$) and the vector $\bar{\mathbf{r}}_k(P)$ to the point P. The third effect is a variation with the cosine distribution of the source $\cos\varphi$, see fig. 2.3, where φ is the angle between the target surface normal $\bar{\mathbf{r}}_{Fk}$ and $\bar{\mathbf{r}}_k(P)$. The angles φ and θ are both depending on the coordinates of point P. The angle α is the tilt angle of the magnetron relative to the substrate surface normal and also the angle of rotation of the magnetron relative to $\hat{\mathbf{z}}_0$, the same as in fig. 6.3. Note that the relation $\theta = \varphi + \alpha$ only holds for points along lines in the plane defined by vectors $\hat{\mathbf{z}}_0$ and $\bar{\mathbf{r}}_{Fk}$. $\bar{\mathbf{z}}$ is the vertical vector from the magnetron to the plane of the substrate, and can hence vary. $\hat{\mathbf{z}}_0$ is also a vertical vector but from the magnetron to the horizontal plane of the focus point F, and is hence constant. The proportionality constant A_k will depend on many factors which are assumed to be constant during the time of the growth. These factors include the power on the magnetron, the pressure in the chamber, factors describing

the magnetron, such as the target material, the strength of the magnetic field, the race-track depth of the target, etc. The relation to A_k is not always linear for these factors. Further A_k only describes non-angular dependencies of these factors. To obtain the value of this parameter calibrations must be done, as will be described below.
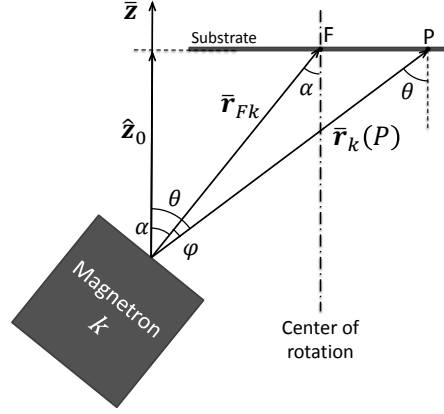

Figure 6.4. Schematic showing the definitions of angles and vectors used to calculate the deposition rate from magnetron k at a point P. The point F is the focus point of the magnetrons as defined in fig. 6.3, $\hat{\mathbf{z}}$ is parallel with the z-axis as defined in the coordinate system of fig. 6.2 and fig. 6.3. For clarity the length of $\bar{\mathbf{z}}$ has been exaggerated, whereas for this geometry in this figure it should actually be $\bar{\mathbf{z}} = \hat{\mathbf{z}}_0$.

At the sputtering pressure, all atoms will not travel straight. Due to the gas phase collisions there will be a distribution or directionality of the vapour cloud from the source. Here I have modelled this by $\cos^n \varphi$ in a similar way as the directional n:th power cosine distribution for evaporation [11], see fig. 2.3. n is an empirically determined number which describes how narrow the vapour cloud is. It will depend on the pressure, target properties like race-track diameter and depth etc. and then takes into account the angular dependence of these factors. A high value of n then means a more directed lobe. However even with this modification, the model does not hold if the pressure is too high or the sputtered elements are too light. With this modification the expression becomes:

$$\Phi_k(P) = A_k \frac{\cos\theta \cos^n \varphi}{\pi |\bar{\mathbf{r}}_k(P)|^2} \tag{6.3}$$

At the special point F, the focus point of the magnetrons as defined in fig. 6.3, the following holds: $\varphi = 0$, $\theta = \alpha$ and $\bar{\mathbf{r}}_k(P) = \bar{\mathbf{r}}_{Fk}$. Here the rate becomes

$$\Phi_{Fk} = A_k \frac{\cos\alpha}{\pi |\bar{\mathbf{r}}_{Fk}|^2} \tag{6.4}$$

71

Calibration is done by determining Φ_{Fk} experimentally for a specific condition described by A_k. We can then remove A_k by combining it with eq. (6.3) to get

$$\frac{\Phi_k(P)}{\Phi_{Fk}} = \frac{A_k \frac{\cos\theta \cos^n\varphi}{\pi|\bar{\mathbf{r}}_k(P)|^2}}{A_k \frac{\cos\alpha}{\pi|\bar{\mathbf{r}}_{Fk}|^2}} \implies \tag{6.5}$$

$$\Phi_k(P) = \Phi_{Fk} \frac{|\bar{\mathbf{r}}_{Fk}|^2}{|\bar{\mathbf{r}}_k(P)|^2} \frac{\cos\theta \cos^n\varphi}{\cos\alpha} \tag{6.6}$$

But since we have three variables depending on P this expression is cumbersome to use, especially for points not in the plane where $\theta \neq \alpha + \varphi$. By using the definition of the scalar product we have

$$\cos\varphi = \frac{\bar{\mathbf{r}}_{Fk} \cdot \bar{\mathbf{r}}_k(P)}{|\bar{\mathbf{r}}_{Fk}||\bar{\mathbf{r}}_k(P)|} \tag{6.7}$$

$$\cos\theta = \frac{\bar{\mathbf{r}}_k(P) \cdot \bar{z}}{|\bar{\mathbf{r}}_k(P)||\bar{z}|} \tag{6.8}$$

$$\cos\alpha = \frac{\bar{\mathbf{r}}_{Fk} \cdot \hat{z}_0}{|\bar{\mathbf{r}}_{Fk}||\hat{z}_0|} \tag{6.9}$$

and we can substitute the cosines in eq. (6.6) to have

$$
\begin{aligned}
\Phi_k(P) &= \Phi_{Fk} \frac{|\bar{\mathbf{r}}_{Fk}|^2}{|\bar{\mathbf{r}}_k(P)|^2} \frac{\bar{\mathbf{r}}_k(P)\cdot\bar{z}}{|\bar{\mathbf{r}}_k(P)||\bar{z}|} \left(\frac{\bar{\mathbf{r}}_{Fk}\cdot\bar{\mathbf{r}}_k(P)}{|\bar{\mathbf{r}}_{Fk}||\bar{\mathbf{r}}_k(P)|} \right)^n \frac{|\bar{\mathbf{r}}_{Fk}||\hat{z}_0|}{\bar{\mathbf{r}}_{Fk}\cdot\hat{z}_0} \\
&= \Phi_{Fk} \frac{|\bar{\mathbf{r}}_{Fk}|^3}{|\bar{\mathbf{r}}_k(P)|^3} \frac{|\hat{z}_0|}{|\bar{z}|} \frac{\bar{\mathbf{r}}_k(P)\cdot\bar{z}}{\bar{\mathbf{r}}_{Fk}\cdot\hat{z}_0} \left(\frac{\bar{\mathbf{r}}_{Fk}\cdot\bar{\mathbf{r}}_k(P)}{|\bar{\mathbf{r}}_{Fk}||\bar{\mathbf{r}}_k(P)|} \right)^n \\
&= \Phi_{Fk} \frac{|\bar{\mathbf{r}}_{Fk}|^{(3-n)}}{|\bar{\mathbf{r}}_k(P)|^{(3+n)}} \frac{|\hat{z}_0|}{|\bar{z}|} \frac{(\bar{\mathbf{r}}_k(P)\cdot\hat{z})(\bar{\mathbf{r}}_{Fk}\cdot\bar{\mathbf{r}}_k(P))^n}{\bar{\mathbf{r}}_{Fk}\cdot\hat{z}_0}
\end{aligned} \tag{6.10}
$$

Non-combinatorial deposition rate

For a non-combinatorial sputtering system the geometry is usually such that substrate and the target are parallel, $\alpha = 0$, or if $\alpha \approx 0$ the distance from target to substrate is usually so large that the angle can be neglected. Then $\theta = \varphi$ and the relation becomes:

$$\Phi_k(P) = \Phi_{Fk} \frac{|\bar{\mathbf{r}}_{Fk}|^2 \cos^{(n+1)}\varphi}{|\bar{\mathbf{r}}_k(P)|^2} \tag{6.11}$$

Usually the sample is so small relative to the distance to the source that $\varphi \approx 0$ and $\bar{\mathbf{r}}_k(P) \approx \bar{\mathbf{r}}_{Fk}$ and the rate becomes constant over the entire sample, which is the usual assumption, when performing non-combinatorial sputter deposition. For all the samples grown in part I this assumption was used.

Rate calculations for Sleipnir

To apply these formulas to the geometry of the sputter system described in section 6.1, we need to define some of the vectors. The position of F has the coordinates $[0,0,0]$, and the position M_k of each magnetron is given by the coordinates in table 6.1. The coordinates $[P_x, P_y, P_z]$ of position P is a variable. From these we can calculate the vectors

$$\bar{\mathbf{r}}_{Fk} = F - M_k \tag{6.12}$$

$$\bar{\mathbf{r}}_k(P) = P - M_k \tag{6.13}$$

$$\hat{z}_0 = [0,0,136.47] \tag{6.14}$$

$$\bar{z} = [0,0,(\bar{\mathbf{r}}_k)_z] \tag{6.15}$$

If we want to calculate the rate in any point P (for which we have the coordinates) we first need to measure the rate Φ_{Fk} for each magnetron in the focus point. Then we use eqs. (6.12) to (6.15) together with eq. (6.10).

Rotation

A common way to ensure homogeneous films in non-combinatorial sputtering is by rotating the substrate. For geometries where $\alpha \approx 0$ rotation is usually enough to average out any directionality of the incident sputtered atoms. But for the geometry we are considering $\alpha \gg 0$ and therefore more care has to be taken when averaging. By symmetry the deposition rate at a certain radial distance from the centre of rotation should, if the rotation speed is large enough, have the same average composition. If the rate is linear with distance from the magnetron the same should be valid for all points, but the rates in the current geometry do not vary linearly. Performing the integral of the deposition rate over an entire rotation at a radial distance r_0 and dividing by the circumference gives the average rate at this r_0:

$$\Phi_k^{rot.avg.} = \frac{1}{2\pi r_0} \int_0^{2\pi} \Phi_k(P(r_0, \beta)) \, d\beta \tag{6.16}$$

where β is the in-plane angle as defined in fig. 6.2 and P is parametrized as

$$P(r_0, \beta) = [r_0 \cos(\beta), r_0 \sin(\beta), 0] \tag{6.17}$$

6.2.2 Composition

When co-sputtering, the composition $C_k(P)$ of element k in point P can be calculated through

$$C_k(P) = \frac{\Phi_k(P)}{\Phi(P)} = \frac{\Phi_k(P)}{\sum_{k=1}^m \Phi_k(P)} \tag{6.18}$$

Where the deposition rates are given in atoms per area per second (at./(Å^2 s)). Composition in atomic percent (at.%) is obtained by multiplying $C_k(P)$ by 100.

6.2.3 Thickness

Calculating the thickness in a film is not as straightforward as the composition. The thickness of the resulting film will depend on the density and the structure of the resulting material at that specific composition. Both the density and the structure are composition dependent so if a composition gradient sample is deposited this composition variation must be taken into account. Furthermore, when dealing with thin films other effects such as those imposed by the substrate must be considered. Examples are the clamping of the substrate, epitaxial growth, textured growth, and more. The structure can also be affected by the energy and incident angle of the sputtered atoms, e.g. an energetic particle flux can create a denser film while even higher energy can instead introduce disorder and make it less dense. The incident angle can create shadowing effects or tilted textures.

If we assume these effects to be negligible then if we know the final density $\delta_f(P)$ (at./Å^3) we can calculate the thickness d(P) (Å) at each point. The thickness is linear with time t_{dep} as

$$d(P) = t_{dep} \frac{\sum_{k=1}^{m} \Phi_k(P)}{\delta_f(P)} \tag{6.19}$$

If the density is linearly dependent on composition $\delta_f(P) = \sum_k^m \delta_k C_k(P)$ then the thickness is

$$
\begin{aligned}
d(P) &= t_{dep} \frac{\sum_{k=1}^{m} \Phi_k(P)}{\sum_{k=1}^{m} \delta_k C_k(P)} \\
&= t_{dep} \frac{\sum_{k=1}^{m} \Phi_k(P)}{\sum_{k=1}^{m} \delta_k \left(\frac{\Phi_k(P)}{\sum_{k=1}^{m} \Phi_k(P)} \right)} \\
&= t_{dep} \frac{\left(\sum_{k=1}^{m} \Phi_k(P)\right)^2}{\sum_{k=1}^{m} \delta_k \Phi_k(P)}
\end{aligned}
\tag{6.20}
$$

This should work well for e.g. amorphous or alloys where the constituents are fully soluble. If the material has different phases for different compositions the thickness can not be calculated using this expression, and a modification for the specific case must be made. But even if the thicknesses can not be calculated this model can still calculate the compositions.

6.2.4 Adjusting rate

If a certain composition and/or thickness is wanted in the sputtered film this can be tuned by selecting the appropriate combinations of powers and depositions times. The deposition rate can be tuned since it is linear with the supplied power, W, above a certain minimum power which is required to ignite

the plasma. Calibration of the sputter rate versus power is done by a linear fit of measured rates at different powers. From my experience it is required to include both a power dependent slope and an offset. The tuned rate is given by:

$$\Phi'_k = \Phi_k^{\text{slope}} \cdot W_k + \Phi_k^{\text{offset}} \qquad (6.21)$$

The slope and offset rate must be calculated separately by eq. (6.10) using the corresponding term in the calibration rate Φ_{Fk} before the final rate is given by eq. (6.21). Φ'_k must be used in eqs. (6.18) and (6.20) to get the resulting $C_k(P)$ and $d(P)$.

Selecting power and time

If a multi-element film of a specific composition is wanted the combinations of powers needed is found by solving eq. (6.18) for the rates at this composition. The corresponding power is then found by eq. (6.21). For a binary compound eq. (6.18) gives a system of two equations but the composition must follow $C_1 + C_2 = 1$ which leads to an overdetermined system of equations. The two equations from eq. (6.18) are linearly dependent and follows this relation

$$\frac{C_1}{C_2} = \frac{\Phi'_1}{\Phi'_2} \implies \qquad (6.22)$$

$$\Phi'_1 = \Phi'_2 \frac{C_1}{C_2} \qquad (6.23)$$

This means there is an infinite number of solutions with combinations of W_1 and W_2. In practice the following two equations can be used to find a suitable combination:

$$W_1 = \frac{\frac{C_2}{C_1}\left(W_2\Phi_2^{\text{slope}} + \Phi_2^{\text{offset}}\right) - \Phi_1^{\text{offset}}}{\Phi_1^{\text{slope}}} \qquad (6.24)$$

$$W_2 = \frac{\frac{C_1}{C_2}\left(W_1\Phi_1^{\text{slope}} + \Phi_1^{\text{offset}}\right) - \Phi_2^{\text{offset}}}{\Phi_2^{\text{slope}}} \qquad (6.25)$$

Apart from these equations there are other restrictions on W_1 and W_2 which have to be considered. Such restrictions include: the range of powers over which the rate has a linear relation to power, another is the minimum power over which the plasma is stable, and yet another is the maximum power the power-supplies can deliver, or the maximum power at which the target melts. Usually a solution can be found if the powers are allowed to be high, but then other problems occur. The higher energy of the sputtered atoms may affect the structure of the film, and this has to be taken into account. If instead small powers are desired the resolution with which the power can be set is the restriction: the smaller the resolution, the more combinations of (W_1, W_2) are

available. When there is a restriction in film thickness it has to be controlled by the deposition time. If higher power settings are required to achieve a specific composition, this means shorter times might be needed. Then another limiting factor comes in to play, the time resolution for controlling the deposition time.

Determining the power for deposition of ternary (or quaternary) materials is done in the same way. But now it might be more difficult to find a suitable combination of powers since two (or three) of them are coupled and still only one is a free parameter. Once again using the k set of equations from eq. (6.18) and $\sum_{k=1}^{3or4} C_k = 1$ gives four(five) equations and three(four) unknowns. In the quaternary case this becomes

$$\Phi_1'(W_1) = \frac{C_1}{1-C_1}(\Phi_2'(W_2) + \Phi_3'(W_3) + \Phi_4'(W_4)) \tag{6.26}$$

$$\Phi_2'(W_2) = \frac{C_2}{1-C_2}(\Phi_1'(W_1) + \Phi_3'(W_3) + \Phi_4'(W_4)) \tag{6.27}$$

$$\Phi_3'(W_3) = \frac{C_3}{1-C_3}(\Phi_1'(W_1) + \Phi_2'(W_2) + \Phi_4'(W_4)) \tag{6.28}$$

$$\Phi_4'(W_4) = \frac{C_4}{1-C_4}(\Phi_1'(W_1) + \Phi_2'(W_2) + \Phi_3'(W_3)) \tag{6.29}$$

For simplicity we solve for the rate $\Phi_k'(W_k)$ since it is proportional to W_k and the corresponding value can be calculated afterwards. Now we have one degree of freedom, if we select the rate $\Phi_4'(W_4) = A$ we get

$$\Phi_1' = \frac{C_1}{1-C_1}(\Phi_2' + \Phi_3' + A) \tag{6.30}$$

$$\Phi_2' = \frac{C_2}{1-C_2}(\Phi_1' + \Phi_3' + A) \tag{6.31}$$

$$\Phi_3' = \frac{C_3}{1-C_3}(\Phi_1' + \Phi_2' + A) \tag{6.32}$$

which becomes

$$\begin{pmatrix} \frac{1-C_1}{C_1} & -1 & -1 \\ -1 & \frac{1-C_2}{C_2} & -1 \\ -1 & -1 & \frac{1-C_3}{C_3} \end{pmatrix} \begin{pmatrix} \Phi_1' \\ \Phi_2' \\ \Phi_3' \end{pmatrix} = \begin{pmatrix} A \\ A \\ A \end{pmatrix} \tag{6.33}$$

This is easily solved for the three deposition rates. There is still an infinite number of solutions, and it does not matter which rate we set, but it can still be difficult to find a combination where all the max/min and resolution limitations on (W_1, W_2, W_3, W_4) are fulfilled simultaneously. Fortunately for a combinatorial composition gradient film this might not be a problem since the desired composition can still be achieved at another point on the sample.

In part I the precise control of the deposition rate required a small resolution in both power and time. Due to the large size of the magnetron targets in the

combinatorial sputter system (Sleipnir) the deposition rate is generally high. Therefore another deposition system was used to grow the samples in part I. Another reason not to Sleipnir was to avoid the uncertainties introduced by the strong dependence of thickness and composition on radial position.

6.3 Verification of the sputter system capabilities

The performance of the sputter system's capability to produce composition graded samples is exemplified in paper IV and paper V as well as by others [96, 97]. This section will present some more detailed examples and also verifications that the mathematical models presented in the previous sections are valid. Several materials systems will be used for this: amorphous Co-Fe-Zr to show the ternary capabilities, and amorphous Tb-Co to show the binary gradient. Thickness gradients will be exemplified by amorphous Fe-Zr and Cu. Compositions have been measured with Rutherford backscattering spectrometry (RBS) and thicknesses with x-ray reflectivity (XRR).

6.3.1 Fabrication

All these samples were deposited at room temperature using 99.999 % pure Ar as a sputtering gas. For the Fe-Zr and Co-Fe-Zr samples the Ar gas flow was 15 sccm with the throttle valve fully open giving a pressure of 1×10^{-3} torr. For the Tb-Co and Cu samples the Ar gas flow was 20 sccm with the throttle valve partially closed giving a pressure of 2×10^{-3} torr. These different deposition sessions were carried out over several years but the base pressure in the chamber was never above 2.5×10^{-9} torr before any one of the sputtering sessions.

For the amorphous samples the films were deposited on naturally oxidized Si(100) substrates which were pre-heated, at base pressure, to 650°C for 20 min to remove impurities and cooled down to room temperature before deposition started. To ensure amorphous films, a buffer layer of $Al_{70}Zr_{30}$ with a nominal thickness of 30 Å to 80 Å was deposited on the natural oxide of the Si [98]. For the Cu samples etched Si substrates as described in part I were used. All samples were capped with a 30 Å to 80 Å thick $Al_{70}Zr_{30}$ layer to protect against oxidation. Both buffer and cap layers were deposited with a rotating sample to ensure a homogeneous composition over the wafer.

The geometry for each set of samples was different and will be explained right before the corresponding results further down in the text.

6.3.2 Composition and thickness characterization

RBS

Rutherford backscattering spectrometry (RBS) was used to determine the composition at different points on the samples. The analyzed area of the sample at each point was no more than 3 mm to 4 mm in diameter, which means it covers a range of compositions. This will be discussed together with the results on the Tb-Co samples. The measurements were performed using single charged He$^+$ ions at a primary beam energy of 2.00 MeV at a scattering angle of 160° relative to the incident beam. In an attempt to speed up analysis, simulations were not done using SIMNRA [99], which is the normal procedure, since it would have been tedious to repeat the simulations for this many measurement points. Instead the yield in the peak of each element was used to determine the composition. Each spectrum was normalized to the total yield to enable comparison between different RBS measurements. Then the peak of each element was integrated (see fig. 6.5), giving a yield Y_A for element A. For a material composed of n elements $A, B, \ldots W$ the relation between the yield Y_A and the composition x_A for element A is given by:

$$\frac{Y_A}{\sum\limits_i^n Y_i} = \frac{x_A Z_A^2}{\sum\limits_i^n x_i Z_i^2} \tag{6.34}$$

where Z_i is the atomic number of each elemental species. There are n similar equations and by simultaneously solving these equations together with the condition that $\sum_i^n x_i = 1$ the elemental concentrations x_i in at.% can be determined.

This approach caused two problems where the first concerned the Fe-Zr and Co-Fe-Zr samples since they had a buffer and cap layer containing Zr. The signal from this Zr was overlapping with the Zr from the combinatorial film. Therefore the yield of the total Zr peak was subtracted by the normalized yield measured from the Zr peak in an 80 Å (50 + 30Å) thick $Al_{70}Zr_{30}$ layer grown under nominally the same conditions as the cap and buffer layers. This introduce some extra uncertainty in the Zr compositions, and therefore also the Co and Fe compositions. The second problem concerned the Co-Fe-Zr samples. Since Fe and Co have similar atomic number and mass their peaks in an RBS spectrum will overlap if they are located at the same depth in the film. To be able to separate the signal from each element, layered reference samples were also deposited. In these samples the Co, Fe and Zr were not sputtered simultaneously but in sequence, giving a layered sample with nominally the same integrated composition as the co-sputtered versions at each point. The sequence Fe-Zr-Co (from the bottom) gave a larger enough peak separation between Fe and Co (see fig. 6.5). But the possibility of something being slightly different between these reference samples and the "real" samples adds some extra uncertainty to the measured compositions.
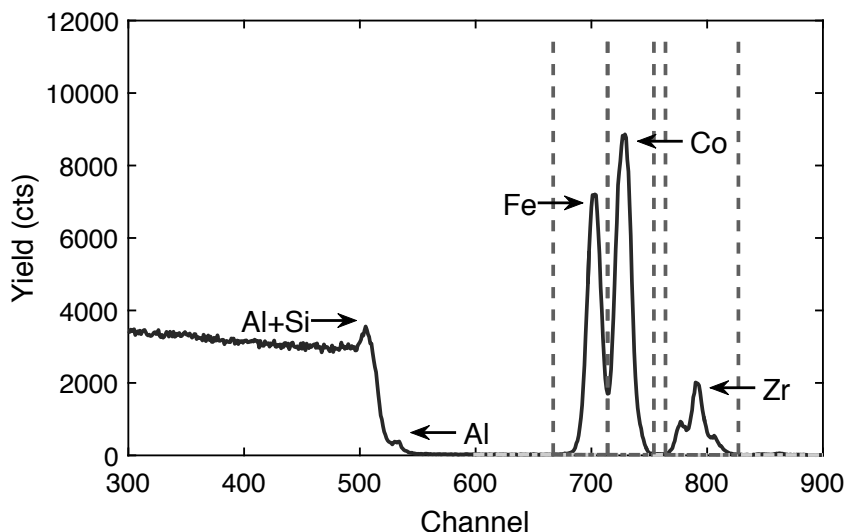
Figure 6.5. Example of an RBS spectrum from one of the sequential $Al_{70}Zr_{30}$/Co-Zr-Fe/$Al_{70}Zr_{30}$ samples. Here each of the elemental peaks are marked. The lines mark the limits of the yield integration.

XRR

The thicknessess at different points on the samples were measured with standard XRR. Cu K_α radiation was used in a Bruker D8 with Göbel mirror and a beam shaper slit as incident beam optics and slits defining the diffracted beam. A problem with XRR on combinatorial samples is the footprint. For XRR the footprint along the direction of the beam is very long, several centimetres, and usually a set-up with line optics and slits giving a line shaped beam in the transverse direction are used to give a large analysed area, which ensures high intensity. This area can, for a combinatorial sample, cover a large range of thicknesses and compositions. The consequence is that the resulting reflectivity scan is difficult to interpret and may be noisy. Therefore we used a beam shaper slit to narrow down the transverse width of the beam. To counter the longitudinal footprint all samples were cut into smaller pieces usually along the largest gradient to ensure that the variation in the direction of the beam should be as small as possible. These restrictions of the beam caused a decrease in intensity which had to be countered by longer measurement times. During the years we improved the size of the analysed area. For the first set of samples with Fe-Zr the probed area was about $20 \times 20 \, mm^2$, since these were measured on entire 3 inch wafers, while for the later samples the analysed area was only $8 \times 10 \, mm^2$ with samples cut to 10 mm (15 mm for Co-Fe-Zr) along the beam direction. Still for all the measured thicknessess given here they represent a mean value of the thickness around each point.

6.3.3 Results

Binary composition gradient

Samples with Tb-Co binary composition gradients were deposited as described in paper IV. The Tb target was mounted on position 1 and the Co target on position 3 according to fig. 6.2 and fig. 6.3. 60 mm long substrate strips were mounted at an angle $\beta = 135°$. Different powers to the magnetrons were used
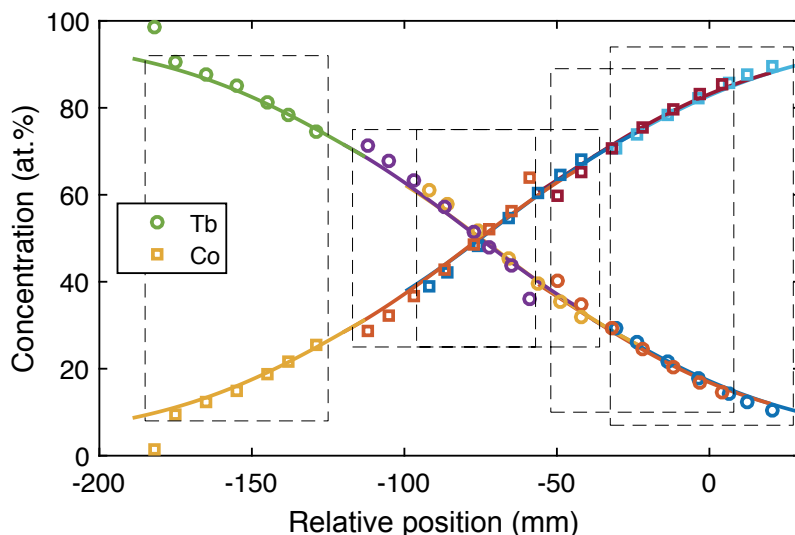
Figure 6.6. Composition vs position for the Tb-Co samples. Lines are the calculated compositions; circles and squares are Tb and Co concentrations, respectively, measured by RBS. The dashed lines show the borders of the five different samples, all grown with different power settings. Five samples is enough to cover the entire composition range. The x-axis is the position relative to the center of the highest Co concentration sample. Data for other samples have been shifted to make the compositions overlap.

to achieve different gradients for each sample. All samples were grown in the centre of the chamber. The composition of the samples can be seen in fig. 6.6. This shows a good example of the possibilities to map out composition variations. Compositions measured by RBS are compared with calculated values for all samples fabricated for paper IV. The dashed boxes show the extent of each 60 mm long sample fabricated. The *x*-axis in this plot does not represent a physical position, since all samples were grown in the centre of the chamber, but it is rather the relative position on each sample minus the shift required for the composition gradient of each sample to overlap with the neighbouring sample. These virtual positions on all but the sample with most Co, the center of which defines $x = 0$ have been shifted (to negative values). With only five samples we could almost completely map out the entire composition span

from 0 at.% to 100 at.%, if another overlap of the samples had been chosen. It is also seen that the calculations correspond well with the measured values.

The uncertainty in composition is not marked but has several contributions. Firstly there is an experimental uncertainty in RBS measurements which is usually some percent, secondly there is the uncertainty due to the size of the RBS spot size and the position determination of this measurement. As explained in paper IV the spot size of 4 mm gives less than 3 at.% uncertainty, which is more than the measurement uncertainty. But when comparing measured to calculated values it is the uncertainty in position which dominates the error, as can be seen in the x-errorbar in figure 1 of paper IV. These positional uncertainties are better illustrated by ternary gradients which will be disclosed in the next section.

Ternary gradients
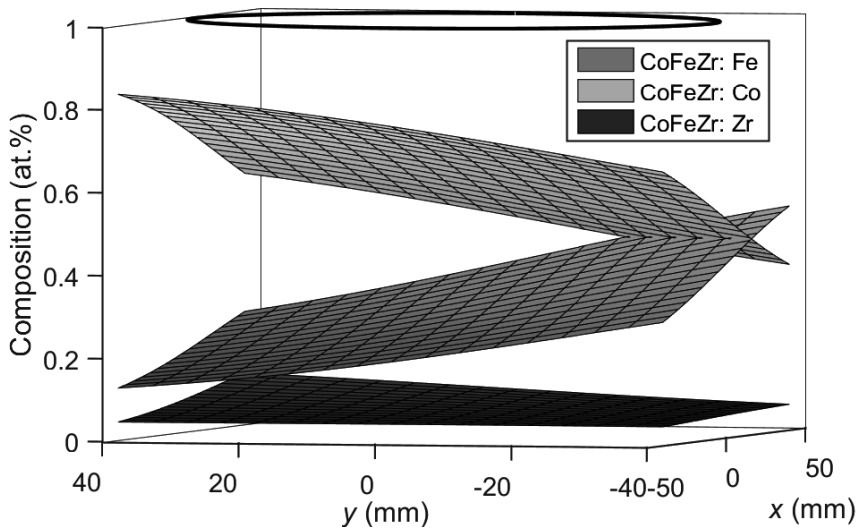
Figure 6.7. 3D plot of the calculated compositions of a ternary deposition. The x- and y-axes corresponds to the coordinate system of the chamber. The surfaces represent the compositions of Co, Fe and Zr, respectively. The black circle shows the xy-position of the 3 inch wafer. The viewing angle, which is close to the opposite side of the Zr magnetron, has been chosen for optimal clarity of the plotted surfaces.

The deposition geometry for the Co-Fe-Zr samples was such that Co and Fe targets where positioned facing each other on each side of the substrate and the Zr target was positioned at 90° from this axis. With the numbering of figs. 6.2 and 6.3, the Fe target was mounted on position 1, Co on position 3 and Zr on position 4. All these samples were deposited in the centre of the chamber. By co-sputtering from the Co, Fe and Zr targets, on non-rotating 3 inch Si wafers, samples with ternary composition gradients were created. A

calculated example is seen in fig. 6.7. These Co-Fe-Zr layers were deposited with a nominal thickness of 500 Å at the centre of the wafer and several different nominal compositions as described in paper V. Along the line from Fe to Co target ($\beta = 135°$) a composition gradient in Fe-Co was created while the Zr was almost constant, see fig. 6.8 for a schematic explanation. To enable measurements with several different techniques such as RBS, MOKE and XRR, the wafers were cut in strips along the Fe-Co gradient, see fig. 6.8.
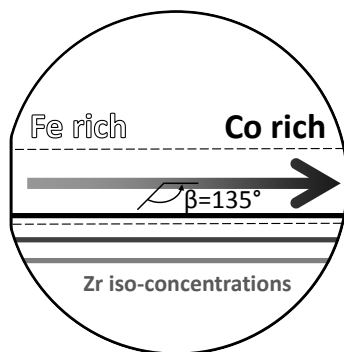
Figure 6.8. Wafer and cut-out strip, schematically showing the composition gradients.

From the beginning we believed the variations in Zr concentration along the Fe-Co gradient were so small they could be neglected, and we assumed them to be constant, as drawn in fig. 6.8. But as it is described in Paper V some properties had a strong dependence on sample position. This we could not explain in a satisfactory manner before we had made the simulations described here. In fig. 6.9 the directional variation of the Zr concentration gradient is clearly seen. The easy axis of the magnetization was found to be directly dependent on this variation.

The position on the wafer was mapped to composition by RBS, and fig. 6.10 shows that a ternary composition was achieved and it follows quite well the compositions predicted by calculations. A slight bend of the Zr composition can be seen, both in calculations but also (barely) in the measured values. When doing comparison between these calculations there are at least three uncertainties. The first is radial uncertainty (parallel to Fe-Co gradient) and the second is the perpendicular uncertainty, both of these due to the mounting of the substrate on the sample holder and in the manipulator, i.e. was the centre of the sample in the centre of the chamber during growth? The third uncertainty is the angular alignment of the sample. Was the same angle β used during growth and cutting of the sample as in the calculations? Calculations of these effects have been carried out and can be seen in fig. 6.11 and fig. 6.12, comparing a ± 5 mm misalignment parallel to the Fe-Co gradient direction (along x_s in fig. 6.9), and ± 7.5 mm misalignment perpendicular to
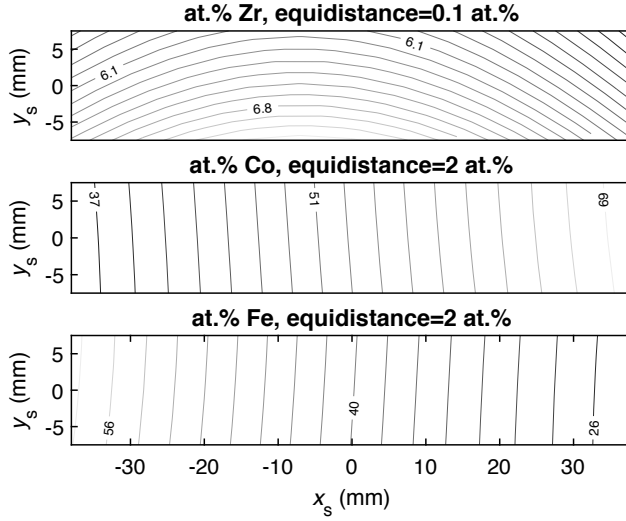
Figure 6.9. Compositions over a cut-out strip (see fig. 6.8), showing calculated composition gradients for (top to bottom) Zr, Co and Fe. x_s and y_s are coordinates on the cut-out strip.

the Fe-Co gradient (along y_s in fig. 6.9). The radial (parallel) misalignment is seen to be dominating with deviations up to $\pm 2\%$ while the perpendicular is as most $\pm 0.4\%$ for the Fe and Co. For Zr the dominating contribution is the perpendicular misalignment which is parallel to the Zr-gradient, here the deviation is as most $\pm 0.5\%$. A $\pm 10°$ misalignment was also calculated but is not shown since it gave smaller deviations than the others and became comparable in size only at the at edge positions. In fig. 6.12 the corresponding thicknesses are shown, and here the perpendicular misalignment is dominating, especially when moving away from the Zr target where the deviation is about 6 Å.

The relevance of this is not only for comparison to calculations. These misalignments also give a measure of the uncertainty in composition and thickness when performing various measurements. In practice the position on the sample is mapped to composition by RBS, and in this mapping the first contribution to the uncertainty enters. When measuring other properties of the sample, by e.g. MOKE, the composition where the measurement is done is determined by measuring the position of the laser spot, and this uncertainty in position then propagates into, and combines with, the compositional uncertainty.

Not all measurement techniques can be considered local (in a point) as MOKE, but many measure over an area or volume. One example is XRR which has a large footprint as already discussed. The Co-Fe-Zr samples were cut into 15 mm wide strips (fig. 6.9) and these where mounted with the x-ray beam going along this length. The ± 8 mm wide x-ray beam was then along
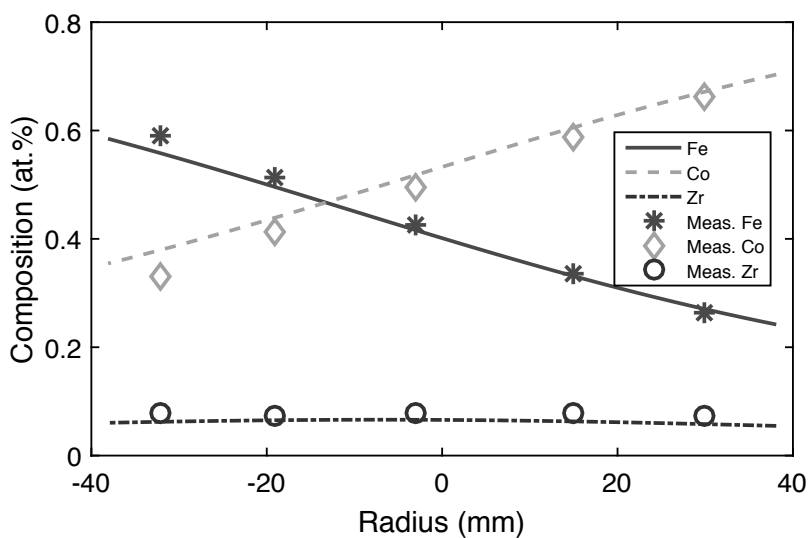
Figure 6.10. Compositions of Fe, Co and Zr along the line at $\beta = 135°$ going from the Fe target (closest to $-40\,\text{mm}$) towards the Co target ($+40\,\text{mm}$). Lines are calculated values and points are measured. A slight bend of the Zr composition can be seen.

Figure 6.11. Calculated compositions of Fe, Co and Zr, along the same line as in fig. 6.10. The different lines show different misalignments of the sample in the chamber; perp+/- represents a $\pm 7.5\,\text{mm}$ shift in the perpendicular direction relative to the Fe-Co gradient, para+/- represents a $\pm 5\,\text{mm}$ shift parallel to the Fe-Co gradient.
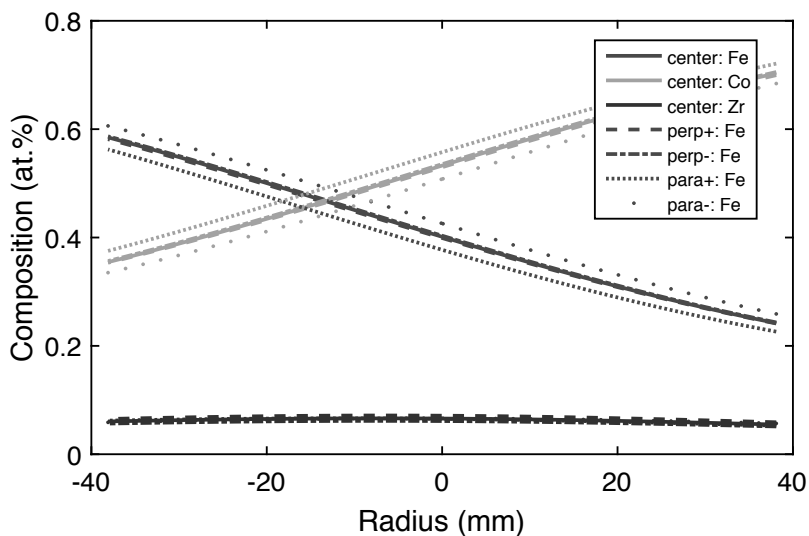
Figure 6.12. Calculated thickness of a Co-Fe-Zr layer, along the line going from the Fe target (closest to -40 mm) towards the Co target ($+40$ mm), i.e. same as in fig. 6.10. The different lines show different misalignments of the sample in the chamber; perp+/- represents a ± 7.5 mm shift in the perpendicular direction relative to the Fe-Co gradient, para+/- represents a ± 5 mm shift parallel to the Fe-Co gradient, ang+/- represents a $\pm 10°$ rotation.
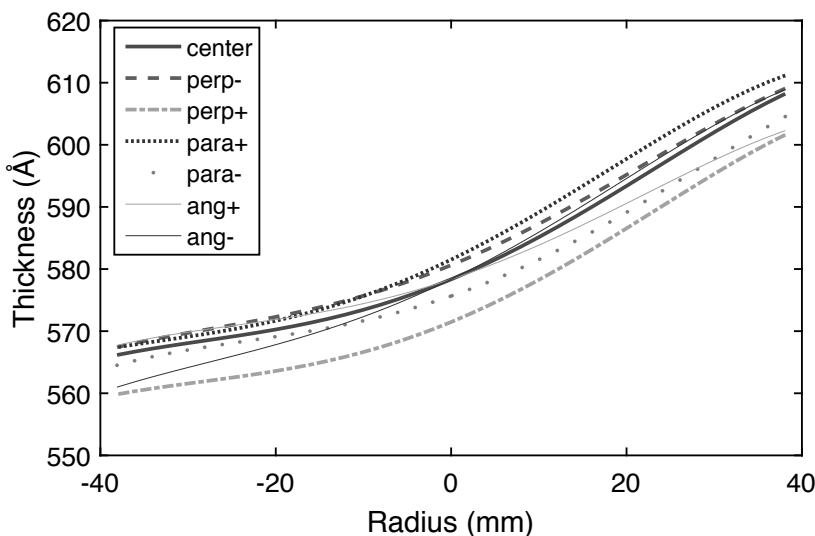
the Fe-Co gradient. This means the XRR scans were measured over a sample area which had a 4 at.% variation in Fe-Co composition and 1 at.% Zr composition, slightly larger than in fig. 6.11. The thickness variations shown in this example (fig. 6.12), will be quite large and different along different directions. Along the x-ray beam the variations will be 8 Å and perpendicular to the beam 4 Å. This will be seen as noise or roughness in the XRR scan, which makes the analysis more difficult. SQUID and VSM are examples of other techniques where these uncertainties can be very important. In both SQUID and VSM the magnetization of the entire sample volume is measured, and for a gradient sample it is then important to know over which compositions the sample piece spans, and also what the thickness variations are.

Thickness

It is not only the capability of the sputter system to fabricate compositional gradients which can be useful. Sputtering from only one source will result in a thickness gradient across the sample surface. This was used to find the optimal thickness for the Cu buffer layer in the samples discussed in part I. Samples were grown on HF-etched Si substrates. First a Cu layer was deposited with a non-rotating substrate and the Cu target was positioned at $\beta = 45°$. On top of this, monolayers of Fe and Ni were sequentially deposited while rotating,

and everything was capped during rotation by an $Al_{70}Zr_{30}$ layer to prevent oxidation. Thickness was measured by XRR and the crystalline structure was measured by XRD. It was found that the Cu lattice parameter increased with thickness up to about 1000 Å, where it levelled out to the bulk value of 3.61 Å. Hence I used 1000 Å Cu buffer layers in future FeNi samples. The measured and calculated thicknesses can be seen in fig. 6.13, and there is a good correspondence between the data sets. It is interesting that simulations show that the FeNi layer is not completely uniform even though it was deposited with rotation. This is since the deposition rates of Fe and Ni are not varying linearly with position over the wafer, and the radial averaging does not give the same rate for each radius. This is important to consider especially when depositing thicker layers, since then the effect becomes notable. This also means the monolayer control of the sputtering rate which is needed to create the $L1_0$ structure can be difficult to achieve using this sputter system.
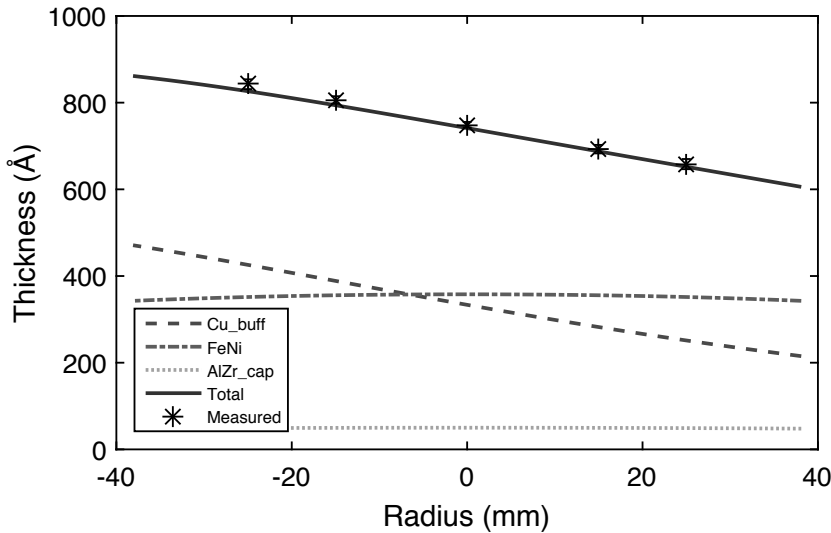
Figure 6.13. Calculated (line) and measured (stars) thickness of an $Al_{70}Zr_{30}$/FeNi/Cu sample, along the line at $\beta = 225°$ from the Cu target (closest to $r = -40$ mm). The calculated thickness corresponds well with the measured. Even though the FeNi layer was rotated during growth it can bee seen that it is not completely flat according to calculations.

Height and position variations of the manipulator

Fe-Zr gradient samples will be used to demonstrate the ability to position the manipulator (and substrate) at different *xyz*-positions and the purpose of this ability will be exemplified. Fe-Zr layers were deposited with Fe in position 1 and Zr in position 3 giving a gradient along the line from the Fe to the Zr target at $\beta = 135°$. The samples had a nominal thickness of 500 Å and nominal

compositions of $Fe_{50}Zr_{50}$ and $Fe_{90}Zr_{10}$ at the centre of the wafer. One sample with nominal $Fe_{90}Zr_{10}$ centre composition was deposited at a different height $z = -50\,mm$ from the focus point. The effect of the sample position in z can be seen in figs. 6.14 and 6.15 where the measured and calculated thicknesses of the two $Fe_{90}Zr_{10}$ samples grown at different z-positions are presented.

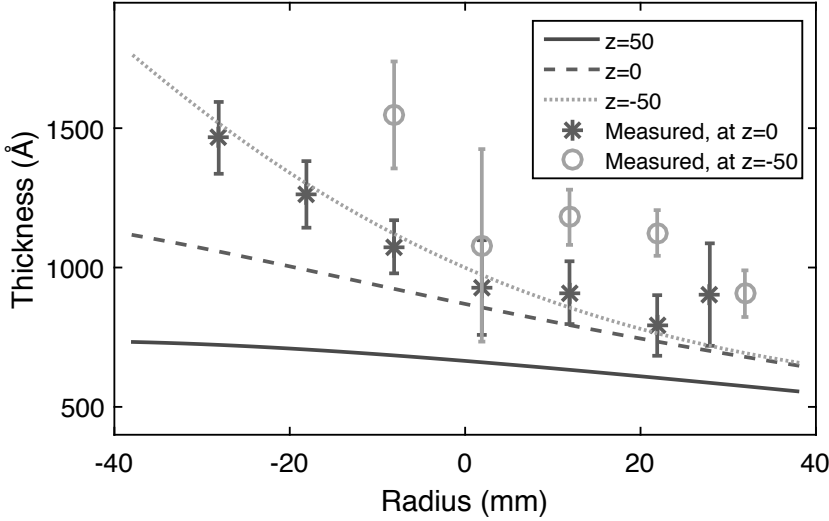*Figure 6.14.* Thickness vs radial position for $Fe_{90}Zr_{10}$ samples grown at two different z-positions ($0\,mm$ and $-50\,mm$). Lines are calculated thicknesses for different heights (50, 0 and $-50\,mm$). The Fe target was closest to $r = -40\,mm$ and Zr target to $r = +40\,mm$.

These plots reveal some interesting things of which I will first discuss the large discrepancy between measured and calculated values. There can be several reasons for this. Firstly, an offset of all values can be explained by the power used. To get the 90/10 composition a quite high rate was needed from the Fe magnetron. The power used was at least 10 times higher than the power where the calibration was done. Therefore, there might be some non-linearity in the rate-power relation, or the slope of the calibration might be off. Another effect might be that of the oblique angle of the incident sputtered atoms. This angle will be larger at the edges and at smaller distances to the magnetrons, as for the $z = 50\,mm$. This can create shadowing effects which will cause texturing of the film and may decrease the density. In this case the high deposition rate might also enhance the texturing effect, since the adatoms might not have time to move around, before they are buried. The oblique angle increases when moving closer to the magnetron, which might be what we see in fig. 6.14. The fact that the discrepancy is larger for the thickness than for the composition(fig. 6.15) might be an indication that texturing is the main cause. Another point to consider is that the accuracy of the model decreases
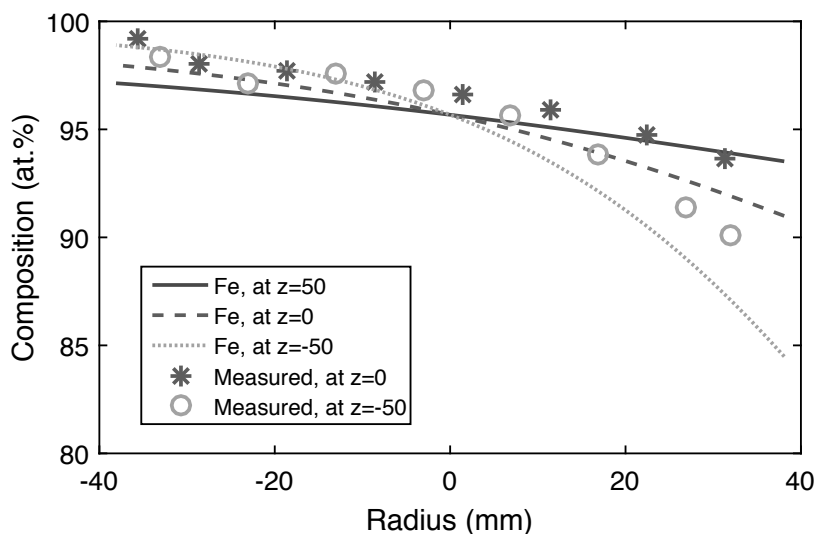
Figure 6.15. Fe compositions vs radial position for $Fe_{90}Zr_{10}$ samples grown at two different *z*-positions (0 mm and -50 mm). Lines are calculated values for different heights (50, 0 and -50 mm). The Fe target was closest to $r = -40$ mm and Zr target to $r = +40$ mm.

closer to the sources. The model assumes a point source but in reality the sputtered atoms mainly originate from the race-track of the targets. The spatial extension of this race-track will have larger effect at closer distances. This will seem like a spread in the cloud of sputtered atoms, and the *n* parameter was introduced to model the spread in the sputtered atoms. For all different samples the choice of *n* value made little difference and $n = 2$ was used for all plots presented in this text. But for these $Fe_{90}Zr_{10}$ samples a better correspondence between data and calculations was seen when using a negative value of *n* meaning a very much larger spread was needed to give the upwards tilt at the edges.

The composition plot is also an example of the difficulty to achieve large composition gradients when one target is dominating. This can also be seen by the flatness at the edges in fig. 6.6. In both figs. 6.14 and 6.15 are also shown the calculated values for a sample grown at a higher position ($z = +50$ mm). The main effect when going to higher positions is that the gradient in both thickness and composition is decreased. This can be useful if flatness is important or when a small compositional gradient is wanted.

The substrate can also be moved in the *xy*-directions, which mainly moves the gradient around. Part of the samples of fig. 6.6 could have been fabricated by this approach instead of changing the power to the magnetrons. This can be useful if e.g a rate can not be reached due to limitations in power settings.

The last examples are the plots in figs. 6.16 and 6.17. These show how the gradients vary in two different directions on one sample. Here $\beta = 135°$ is along the Fe-Zr gradient while $\beta = 225°$ is along the radius perpendicular to the Fe-Zr gradient. In contrast to the gradient composition along the line from the Fe to the Zr target, the composition in perpendicular direction is constant. For the thickness the effect is more difficult to see due to the uncertainties in the measured values, but the calculations predict a variation in both parallel and perpendicular directions.

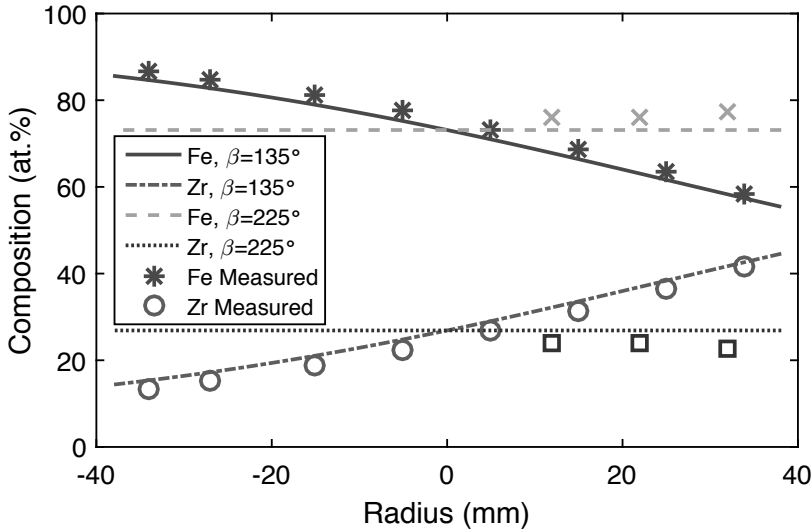*Figure 6.16.* Compositions vs position for sample $Fe_{50}Zr_{50}$ along the radius of two perpendicular directions. $\beta = 135°$ is parallel to the Fe-Zr gradient while $\beta = 225°$ is in the perpendicular direction. Lines are calculated and points are measured thickness. All open symbols are Zr. The Fe target is at $\beta = 315°$ and the Zr target is at $\beta = 135°$.
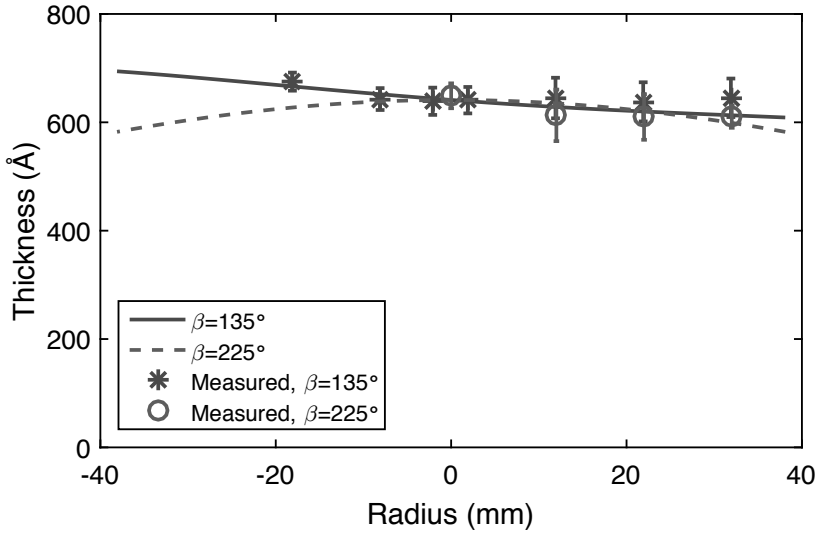
Figure 6.17. Thickness vs position for sample $Fe_{50}Zr_{50}$ along the radius of two perpendicular directions. $\beta = 135°$ is parallel to the Fe-Zr gradient while $\beta = 225°$ is in the perpendcular direction. Lines are calculated and points are measured thickness. The Fe target is at $\beta = 315°$ and the Zr target is at $\beta = 135°$.

6.4 Issues of the combinatorial method

The first thing which people generally come to think about as a benefit of the combinatorial method is that it will be time saving. This is not necessarily always true. Below follows a discussion about some of the benefits and drawbacks.

6.4.1 Benefits

Imagine you want to investigate the compositional dependence of a property of some elemental combination. The conventional way of doing this would be to grow a series of discrete samples with different composition. If you instead grow one combinatorial sample with a continuous gradient covering the compositions of these discrete samples, you have gained time corresponding to the number of discrete samples you made.

   If the investigated property has a "sweet spot" at an unknown composition, which you want to find or measure at, on your combinatorial sample you will simply continue to measure at different positions until you find the spot. On a conventionally sputtered uniform sample if you did not fabricate this composition in the first batch of samples, you might have to make more samples and fabrication of exactly the right composition is not guaranteed. There are many things which might add uncertainties to the comparability between sam-

ples, such as: the gas or a target run out, the chamber is vented, some chamber component is broken and must be replaced, the substrates run out and a new batch must be used, or the samples oxidise over time. These risks of reduced comparability between samples increase with the number of samples and the time separation between deposition sessions. If a gradient sample is made these are non-issues, all points on the gradient sample have been subjected to nearly identical conditions, even after the growth is finished.

From a combinatorial sample the amount of data which is possible to extract is limited only by the spatial resolution (which maps into compositional resolution) of your measurement techniques. If you are deposition ternary (or higher) compositions on wafers the amount is squared since there is a surface of varying compositions. This means you can gain very much data, compared to a series of discrete samples.

6.4.2 Drawbacks

The combinatorial method can be time saving when it concerns the growth of samples, but usually the bottleneck when studying thin films is the measurements and their analysis. If there are not appropriate combinatorial measurement and analysis methods, the time gained when growing the samples is soon lost. The fact that loads of data can been produced might rather result in a longer total time compared to conventional methods. Finding the relevant or interesting data might take time. Also, as was exemplified in the previous section, artefacts due to the graded samples themselves introduce uncertainties and complications in measurements and analysis which can increase the time of these steps.

In the previous sections the uncertainty in measurements of the thickness, structure and composition on a gradient sample were discussed. All measurements on continuous gradient samples are in reality measurements of an average of the property within the area covered by the measurement probe. To measure a property at one composition the measurements must be spatially local. Essentially, the measured area must be small enough to sample an area with acceptable variations in the property measured. The fact that an average property is obtained from a measurement might not be the problem per se. However, for some techniques the extraction of properties from data require modelling, which can be very difficult and simply using an average value of the property might not be appropriate if there are spatial variations.

Some measurement techniques, such as VSM, do not only require the measurement of an extended area/volume but also discrete pieces of samples. This means the sample must be cut into smaller pieces which then might inhibit the possibility to scan or map out a specific composition dependence. Once the sample is cut into small pieces the ability to use the continuous gradient is greatly limited. Non-destructive techniques would be preferred.

The advantage of comparability between samples is not entirely true. The fact that a sample contains a gradient might cause problems in itself. For example it might be difficult to study compositional dependence on a gradient sample if the thickness of the film is also important for the property under study. Decreasing the thickness gradient always means decreasing composition gradient, which implies loosing the benefit of gradient samples. The comparability between points is also connected to the possible shadowing and texture effects caused by the deposition at an oblique angle. This effect is stronger at the edges of the samples, which means edge points might not be fully comparable to other points on a sample. Finally, there are different effects on properties which originate in the compositional gradient itself. If these effects are not wanted or unknown they may complicate analysis. Examples of this are the magnetic anisotropies measured in Paper IV and V.

6.4.3 Solutions and challenges

As has been discussed when doing combinatorics it is important to use local measurement techniques as far a possible. However, if local measurements are not possible there are some ways of decreasing the effects of the gradient. For many techniques smaller areas can be measured, e.g. in XRR beam shapers can restrict the beam spot size. But usually smaller areas will mean that longer measurement times have to be used. For techniques measuring a non-symmetric area, such as XRR, a possibility to avoid the effect of the gradient is to choose the measurement direction to be perpendicular to the gradient itself. This averaging problem can also be decreased by cutting samples into pieces smaller than the area measured by the specific technique. Care has to be taken which direction samples are cut, since for some extended area measurement cutting parallel or perpendicular to the gradient can have different advantages. Cutting samples is done at the expense of the continuous gradient, therefore size and direction have to be chosen with care and different types of measurements should be performed in a suitable order. The techniques requiring cutting of samples must be performed last or after identifying any possible sweet spot or interesting compositions by other techniques. Planning measurements is therefore much more important compared to when conventional deposition and characterization techniques are used.

To exploit the advantages of combinatorics automatization of measurements and analysis should be done. This can be enabled by fabricating sample holders and equipment which allow scanning. The instrument control software must be possible to program to make series of measurements on different points, or to scan over the surface of the sample. Sometimes this will be impossible without cutting samples, e.g. for MOKE it is difficult to fit an entire 3 inch wafer in-between the magnets while still being able to apply high

enough magnetic fields. However, this only restricts the sample in one direction and a sample strip with a gradient can still be scanned.

The idea of combinatorics is to produce larger amounts of data, but to make it feasible manual analysis must be avoided. If automatic analysis of all data is not possible then clever algorithms have to be implemented to select which points to measure or which data to analyse. Otherwise to benefit from the combinatorial method more time and resources for measurement and analysis must be allocated compared to that required for conventional techniques.

Planning of experiments is always important but concerning combinatorics all steps, both growth and measurements, should be planned in parallel before growing any samples. Questions to consider can be: what measurement techniques will be used, are they suitable for samples with a gradient? If not, can the samples be made in way to make the measurements easier? E.g it might be better to make many samples each with a smaller gradient instead of one sample covering the entire composition range. Some experiments require a good choice of the gradient, e.g. if the property being studied is very sensitive to the composition. It might be beneficial to grow the samples at a high position in the chamber, which will create a smaller gradient. This means you increase the compositional resolution on the sample and decrease the averaging effect of the gradient, allowing a larger spatial resolution of the measurement equipment. Another example is if a ternary compound is investigated: will then a sample with a ternary gradient be needed? Will this be beneficial or will it just add more uncertainties to all measurements? It might be better to make several different samples with constant composition of the third element. The last example is that some materials are more suitable for combinatorics than others. For example if the structure is important, crystalline materials are very suitable since XRD can be measured relatively locally while amorphous materials will be more challenging since they will require grazing incidence XRD, with its large measurement area, for structure determination.

The simulation model described in this chapter can be very useful for this type of planning. The size and extent of the gradient both in composition and thickness can be calculated. The number of samples required if a certain composition range shall be covered can be obtained, etcetera. Different settings can be investigated to find the most optimal way of growing the series of samples. I recommended to perform a simulation before each growth of a combinatorial sample. Once the samples are grown, comparison to the simulations can also be very useful to plan what measurements to perform.

The final point to consider where combinatorial samples differ form conventional, is the issue of sample labels which might not be trivial. When using standard discrete samples keeping track of each sample is usually easy. There will be one sample box with one label for each sample. But what is the best practice when you have continuously varying properties? When the position on the sample will map to composition and different properties, it is very important to define a reference point on the sample and define how positions

are measured relative to this. Having a well defined labelling convention simplifies especially when there are many co-workers. In some cases it might be beneficial not to grow entire wafers or to grow on patterned substrates to simplify the identification of different points on the gradient sample.

6.5 Conclusion

We have built a combinatorial sputtering system which can produce up to 3 inch large samples with spatial composition and thickness gradients. The chamber is very versatile and can be used for many applications such as magnetic multilayers. The composition and thickness gradient can be controlled by the power on the magnetrons and also by the position of the wafer in the chamber. By a simple geometrical model we can simulate the sample composition and thickness of deposited samples. This model has been verified by comparison to experiment and it is very accurate for cases within the limiting assumptions. Some deviations are seen mainly for thicknesses which is difficult to model in a general way. Among the benefits of the combinatorial technique is the possibility to fabricate samples with a continuous composition. Among the drawbacks are the measurement difficulties due to averaging measurements. The simulation model can be useful for planing experiments enabling the full benefits of combinatorial technique to be exploited.

7. Studies employing the combinatorial method

This chapter gives a summary of papers IV and V, which both employ the combinatorial method for sample growth as presented in the previous chapter. The samples in both papers are amorphous thin films. An amorphous material lacks long range order: compared to a crystalline material where the atoms are positioned in a lattice, in the amorphous material they are randomly distributed. This gives many exciting properties which can be quite different from crystalline materials. An example is the fracture strength which is much larger for metallic glasses compared to the crystalline material of the same elements [100]. Amorphous materials are suitable for thin films. Since they do not have any dislocations or atomic steps on the surface they grow in very flat layers, which can simplify fabrication of multilayer structures. Implied in the word amorphous is that the material is isotropic, i.e. there is no intrinsically preferred direction of any property in the material. Therefore amorphous magnetic materials are very soft in the magnetic sense, and have been used in applications where low coercivity is wanted. But over the years it has been shown that there can be some anisotropy in the magnetic properties of amorphous thin films [101]. There seems to be some medium-range to short-range order which might give magnetic anisotropy. The mechanism behind this is therefore interesting to study.

7.1 Amorphous Tb-Co

In paper IV we investigated amorphous Tb-Co grown with a composition gradient in Tb and Co. We used a special sample holder which produced a constant magnetic field parallel to the surface of the samples and perpendicular to the gradient direction. Tb-Co is interesting since it has ferrimagnetic ordering. This means the magnetic moments of Tb and Co align anti-parallel, and this gives the material a compensation temperature T_{comp} and composition x_{comp}. At this temperature which varies with composition, the moments cancel each other and the total magnetization is zero. Thin film Tb-Co is also interesting since it has an out-of-plane magnetic anisotropy.

Questions:
We had three main questions which motivated this project:

- Is it possible to grow amorphous Tb-Co with composition gradients by combinatorial sputtering?
- Is it possible to imprint in-plane magnetic anisotropy in Tb-Co?
- How do the magnetic properties vary with Tb-Co composition?

Results:
- It is possible to grow amorphous Tb-Co with composition gradients by our combinatorial approach. This is very well exemplified in fig. 6.6.
- The magnetic properties, e.g. T_{comp}, are consistent with reports from previous literature. We measured a continuous variation in all magnetic properties with composition.
- When applying a growth field, the intrinsic out-of-plane anisotropy is not changed but an in-plane component is added. This possibility to affect the anisotropy is dependent on Tb-Co composition.
- The imprinted in-plane component of the magnetic anisotropy affects the direction and shape of the magnetic domains.

7.2 Amorphous and crystalline Co-Fe-Zr

In paper V we studied Co-Fe-Zr samples with a ternary composition gradient. This material system was one of our first attempt at combinatorics, and therefore one idea was to test the chamber's capabilities of producing ternary gradients. But there are some "teething problems" with these samples. First of all I did not have full control over the method to select compositions and therefore I missed our aim at 10 at.% and 18 at.% Zr in the samples. The consequence was a set of both amorphous and crystalline samples, which opened up for new possibilities for comparison of amorphous and crystalline structures. Furthermore, initially we were not aware of the strong influence of the Zr-gradient which we assumed was constant since the compositional variations were so small, see figs. 6.8 and 6.9. At first it was very confusing when different properties were plotted versus Co composition. For several of the properties we could see a strong positional dependence, an example of which is seen in fig. 7.1. Additionally, measurements at the edges sometimes gave strange results. We suspect there is some texturing here due to the glancing angle of incidence for the sputtered atoms, but this is something which we have not been able to confirm. Both Zr gradient and possible texturing complicated the analysis and we could not for certain compare edge values to measurements at other points. One of the main experiences learned from this project is that having a ternary gradient makes everything much more uncertain and much more difficult to interpret.

Questions:
These were our main questions in this project:

- Is it possible to grow Co-Fe-Zr samples with ternary composition gradients?
- What happens with the structure for different compositions?
- How are the magnetic properties affected for different compositions?

Results:
- Even though we have not measured the composition at points perpendicular to the Fe-Co gradient, it seems to be possible to grow ternary gradient samples. Since the Co-Fe compositions vary in accordance with calculated compositions, see fig. 6.10, we have no reason to believe the Zr gradient is not varying in the direction perpendicular to the Fe-Co gradient.
- There is a directional variation of the magnetic easy axis on the amorphous samples for different positions on the samples, which probably is due to strain induced by the Zr gradient. This is an indirect evidence that we have achieved ternary gradients.
- The structure is clearly dependent on both Zr and Fe-Co composition. The strongest effect is from the Zr composition. When the Zr content is small enough, <5 at.%, the samples lose the amorphous structure and become poly-(nano)crystalline with grains of size $\sim 15\,\text{Å}$.
- There is a clear difference in magnetic properties between amorphous and crystalline materials even with the same composition in Fe-Co.
- Coercivity and remanence vary with Fe-Co composition. In the crystalline samples this variation is stronger compared to the amorphous samples.
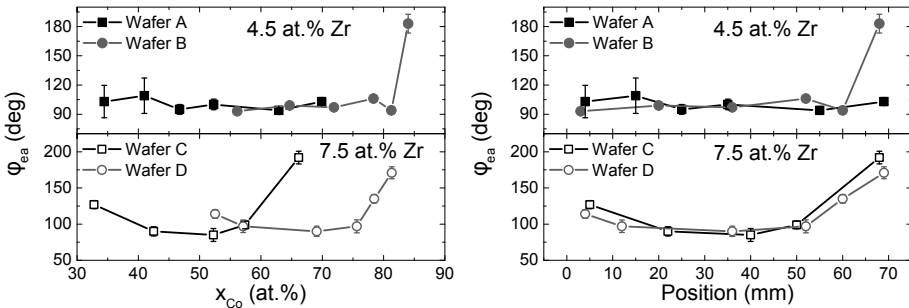

Figure 7.1. The measured easy-axis angle (φ_{ea}) of the Co-Fe-Zr samples, versus composition (left) and position (right). $\varphi_{ea} = 90°$ is parallel to the Fe-Co gradient. The easy-axis direction is clearly dependent on the position on the sample, rather than on the Co content.

8. Conclusions and outlook

A process which in nature takes millions of years has been circumvented in the laboratory by the successful fabrication of $L1_0$ phase FeNi in thin film form. This was done by sputter deposition on HF etched silicon substrates using a combination of epitaxial Cu and $Cu_{100-x}Ni_x$ buffer layers. Many materials systems are very sensitive to composition, which is exemplified by our studies of FeNi. Here, a slight deviation from the nominal deposition rates caused a structure with composition modulations. Fortunately the deviation can be quantified using the XRD pattern, which also enables tuning to obtain ideal growth conditions. To fully achieve the large out-of-plane magnetic anisotropy which is predicted for the FeNi $L1_0$ system, the chemical disorder caused by the surface roughness of the buffer layers must be minimized. Concerning this there is still work to be done.

Variations in composition can also be intentionally utilized to speed up synthesis and analysis of other materials systems. A combinatorial sputter approach was described in the second part of this thesis. Using combinatorics is not without complications, as has been exemplified by two separate studies of amorphous and nanocrystalline alloy films. If proper care is taken, the method is both very useful and powerful. The growth simulation model given here can help planning and analysing similar experiments, facilitating optimal use of the technique.

There is a need for a permanent magnetic material with intermediate cost and properties between those of ferrite magnets and the rare earth permanent magnets. If FeNi $L1_0$, or any similar permanent magnetic material currently under investigation by others, would be realized in bulk form this would be an important step towards more sustainable energy usage. The combinatorial approach might provide a way to find such a material.

9. Svensk sammanfattning

I antropocens tidsålder där mänskligheten måste kämpa mot de klimatförändringar som vi själva har orsakat är tillgång till, samt distributionen och användningen av förnybar och ren energi av största vikt. Den renaste och mest effektiva formen för distribution och användning av energi är i form av elektricitet. Därför måste vi sträva mot ett ännu mer elektrifierat samhälle än dagens, och följden är att behovet och användningen av elektriska maskiner kommer öka i framtiden. Vid omvandlingen mellan mekanisk och elektrisk energi och omvänt används generatorer och motorer. Därför är det väldigt viktigt med en effektiv användning av dessa maskiner både avseende den faktiska användningen men även när det gäller resurserna som krävs för tillverkning. Kopplingen mellan mekanisk och elektrisk energi i dessa maskiner sker genom ett magnetiskt fält. Den traditionella lösningen för att skapa detta magnetiska fält är att använda induktion i och från spolar. Denna lösning har huvudsakligen två problem: det första är att maskinerna blir stora både avseende massa och volym, och det andra är att de inte kan producera särskilt stort vridmoment. En lösning på detta är att skapa det magnetiska fältet med hjälp av permanentmagneter (PM). Även om massan hos en PM-maskin är mindre jämfört med motsvarande induktionsmaskin, så är det fortfarande fördelaktigt att maximera levererad eller genererad energi per massenhet. Två viktiga exempel är vindkraftverk och elektriska bilar. Dagens lösning för elektriska bilar, både hybrider och helt elektriska, kräver tunga batterier. Därför är det viktigt att minimera den totala massan för att maximera bilens energieffektivitet och dess räckvidd. När det gäller vindkraftverk är det uppenbart att en minimerad massa hos generatorn, som ska sitta i toppen på kraftverket, möjliggör enklare design, installation och så vidare. En annan aspekt är att PM-generatorer kan designas utan växellåda, vilket minskar totalvikten men framför allt behovet av underhåll och reparationer, något som är oerhört viktigt speciellt för vindkraftverk placerade till havs.

De permanentmagnetmaterial (PMM) som i dagsläget har bäst prestanda per massenhet är baserade på järn-neodym-bor (Fe-Nd-B) samt samariumkobolt (Sm-Co). För att förbättra högtemperaturegenskaperna hos Fe-Nd-B dopar man dem med dysprosium (Dy) och Terbium (Tb). Grundämnena Nd, Sm, Dy, Tb tillhör alla de sällsynta jordartsmetallerna (eng. Rare Earth Elements, REE). Motorer och generatorer innehållande REEPM har således mycket bättre prestanda jämfört med induktionsmotorer eller motorer innehållande ferritbaserade permanentmagneter, både när det gäller levererat vridmoment men även levererad effekt per massenhet. Ferriter är den typ av magneter som sitter på de flesta kylskåp runtom i världen. De är billiga men kräver

stor volym för att generera samma magnetiska flöde som en REEPM. De sällsynta jordartsmetallerna är därför väldigt viktiga ur ett hållbarhetsperspektiv.

Även fast de sällsynta jordartsmetallerna, trots namnet, är väldigt vanliga i jordskorpan så är de sällsynta i den aspekten att de är väldigt utblandade. De hittas aldrig i ren form, och det är därför väldigt dyrt att bryta dem. Oftast utvinns de som en biprodukt när man bryter andra ämnen såsom järn. Tyvärr så förekommer REE ofta tillsammans med giftiga och radioaktiva ämnen, t.ex. torium, som vid brytning då anrikas i deponeringshögar med slaggprodukter, vilket kan leda till förorening av den omgivande miljön. Bara med tanke på detta så borde användning av dessa ämnen undvikas. De största tillgångarna som är ekonomiskt motiverade att bryta finns i Kina. Detta har givit upphov till en geopolitisk situation som fått många följdverkningar, där denna avhandling är en av dem. Vissa menar att Kina medvetet har använt sin dominerande ställning som ett internationellt politiskt instrument. Men faktum är att på 1990-talet var de flesta gruvor utanför Kina tvungna att stänga på grund av konkurrens från billiga kinesiska gruvor. Detta skedde samtidigt som betydelsen av metallerna och efterfrågan på dem ökade, dels på grund av det ökade behovet av förnybar energi men även på grund av utvecklingen av high-tech-produkter, t.ex. mobiltelefoner, som kräver dessa ämnen. Detta ledde till vad har kommit att betecknas som en kris 2011. Den utlösande faktorn var en kraftig minskning i de exportkvoter som Kina sedan flera år haft på REE för att kunna säkerställa det inhemska behovet. I denna kris sköt priserna på REE i höjden på väldigt kort tid. Många länder och företag insåg sitt beroende av kinesiska REE. Ur många aspekter så var detta beroende oönskat och ur ekonomiskt perspektiv var de höga priserna och osäkerheten i prisvariation något framför allt företag ville bli fria från. Därför sattes en mängd processer igång. T.ex började man prospektera efter nya fyndigheter och det blev återigen ekonomiskt motiverat att öppna gruvor utanför Kina, och ett exempel är den i Norra Kärr utanför Gränna. Andra åtgärder var att försöka minska behovet av REE eller att hitta ersättningsmaterial. En mängd forskningsprogram startades av både länder och företag på dessa områden. Den första delen av denna avhandling är resultatet av ett sådant projekt initierat av ABB.

En sammanfattning av resultat från forskning runtom i världen ges i denna avhandling. När det gäller att minska användandet av REE har forskningen lett till att mängden av de dyrare dopningsämnena (Dy, Tb) kan minskas i Fe-Nd-B och man vet att Nd kan ersättas med billigare Ce om man är villig att minska prestandan en aning. Forskning om olika REE-fria ersättningsmaterial är väldigt spridd och det finns många möjliga kandidater. Men framför allt har forskarsamhället insett att det är osannolikt att det går att hitta ett ersättningsmaterial som är bättre än REE-baserade permanentmagneter just på grund av de speciella egenskaperna hos REE-atomerna. Men om man kan hitta ett material som ligger någonstans mellan ferritmagneter och REEPM avseende både egenskaper och pris då har vi vunnit mycket. I denna avhandling har en kan-

didat till ett sådant intermediärt material undersökts: järn-nickel (FeNi) i den så kallade $L1_0$-fasen.

Detta material verkar lovande för att det bara innehåller järn och nickel som är två vanligt förekommande metaller. Därmed är de billiga och dessutom förhållandevis (i jämförelse med REE) miljövänliga att bryta. Både Fe och Ni är dessutom magnetiska vilket ger ett stort magnetisk moment. Det som ger $L1_0$-fasen dess speciella egenskaper är dess strukturella och kemiska anisotropi som ger upphov till en magnetisk anisotropi. Ett anisotropt material har en (eller flera) riktningar som är annorlunda ur något hänseende, i jämförelse med ett isotropt material där alla egenskaper är samma oavsett i vilken riktning man tittar. Man kan tänka på FeNi $L1_0$-strukturen som en stapling av alternerande atomlager av Fe och Ni och den speciella riktningen är i staplingsriktningen. Det är fördelaktigt för de magnetiska momenten att peka i denna riktning. Storleken på den magnetiska anisotropienergin är ett mått på hur bra PM-materialet kan bli.

Det som är speciellt med $L1_0$-fasen är att den finns naturlig, men bara i meteoriter som har fått svalna väldigt långsamt under miljontals år. Dagens normala tillverkningsmetoder är inte möjliga att använda med mänsklig tidsskala, utan en ny metod måste utarbetas. Vi har försökt tillverka detta material i form av tunna filmer, med en tjocklek som är ca en tusendel av ett hårstrå: 300 Å (30 nm). Denna metod är inte skalbar till massiva material med massor i storleksordningen g eller kg. Studien är ändå motiverad för att studera fasens egenskaper, och en möjlig tillämpning av tunnfilmsformen skulle kunna vara i halvledarindustrin. Vi har deponerat dessa filmer så att de följer substratets kristallstruktur, vilket kallas epitaxi. För att få till den kemiska anisotropin har vi deponerat alternerande enstaka atomlager av Fe och Ni i en multilagerstruktur, och för att endast deponera ett atomlager åt gången krävdes väldigt noggrann kontroll.

För att bekräfta att den kemiska ordningen har skapats använder vi röntgendiffraktion (XRD). I denna teknik belyser man materialet med röntgenstrålning. Positionen hos röntgenljusets reflexer beror på atomernas avstånd och positioner i materialet. På detta sätt kan man mäta strukturen på atomnivå. Att skilja på positionerna hos Fe- och Ni-atomer är svårt eftersom de har liknande egenskaper. Men det är inte omöjligt och det underlättas om man använder röntgenljus av lämplig våglängd, som man kan få från en synkrotron, t.ex. MAX-lab i Lund. Endast om materialet har $L1_0$-fasen kommer en speciell reflex uppstå, men vid den förväntade positionen observerade vi två reflexer. Detta förklarar vi med en modulering i komposition. Man kan göra en liknelse till amplitudmodulerande radio (AM). Idealt ska kompositionen i materialet växla mellan 100 at.% Fe och 100 at.% Ni för varje atomlager, detta kan liknas vid bärvågen, men amplituden hos denna är i vårt fall inte konstant 100 at.% utan varierar genom djupet i materialet. Detta liknas med röstsignalen som modulerar bärvågen. I frekvensrummet ger detta upphov till två frekvenser symmetriskt kring bärvågsfrekvensen. Frekvensrummet för ett ma-

terial motsvaras av dess röntgendiffraktionsmönster, och här ser vi dessa två reflexer (två frekvenser). Separationen mellan reflexerna beror på längden hos kompositionsmodulationen och vi har använt denna separation som ett mått på kemisk oordning. Tyvärr så försämrar den kemiska oordningen den magnetiska anisotropin. Men vi kunde använda reflexseparationen för att ställa in rätt deponeringshastighet och därmed tillverka ett material utan modulering. Trots detta så uppnådde inte materialet förutspådda värden på den magnetiska anisotropin, vilket troligtvis beror på kvarvarande oordning orsakad av ytans ojämnhet, denna återstår därför att minimera.

En del av detta doktorandarbete har spenderats på att bygga en sputtringsdeponeringsutrustning som kan tillverka prover med tjockleks- och kompositionsgradienter. Tekniker där man simultant tillverkar prover med en mängd kompositioner kallas ofta för kombinatoriska. Sputtring är en process för deponering av tunna filmer som utförs i en vakuumkammare vid ett lågt tryck av argongas. Man får Ar-joner att kollidera med ett mål (eng. target) bestående av det ämne man vill deponera. I kollisionerna sputtras atomer från målet loss. Dessa kommer huvudsakligen färdas rakt fram, men vissa kolliderar med argonet och ju längre avståndet är, till det substrat man vill deponera på, desto färre atomer når fram. Om en sputterkälla är riktad med en vinkel mot ett substrat kommer det i varje punkt vara olika avstånd till källan och därmed olika depositionshastighet. Den resulterande filmen får då en tjockleksvariation (gradient) utmed ytan. Genom att rikta två eller flera sputterkällor med en vinkel mot ett substrat kan man på detta sätt deponera en film som har en kompositionsgradient. Här ges en modell för att simulera kompositions- och tjockleksvariationerna hos sådana filmer. Denna modell är användbar för att kunna planera och även analysera tillverkade tunnfilmer. Sputtersystemet testades genom att tillverka amorfa material. Ett amorft material är oordnat och atomernas positioner är huller om buller, till skillnad från ett kristallint material där de är precist ordnade i ett bestämt mönster. Sådana magnetiska material borde inte ha någon anisotropi, men vi har sett att de kan ha en magnetisk anisotropi. Det verkar bero på vår kombinatoriska sputtermetod.

10. Acknowledgments

My biggest and deepest thanks goes to Gabriella. Thanks for taking me in as a PhD student and allowing me to be selfish for five years by just learning physics only for the sake of my own interest. Thanks for always supporting when times were though, for always listening when I was complaining, and most of all thanks for always finding pragmatical and reasonable solutions.

Tomas although only official supervisor for the last half year, in my mind you have been my supervisor throughout the entire period. Thanks for your patience with me and always being so positive and encouraging.

Erik you stood by and irradiated calm even when it was a bit stormy, thanks for your unwavering interest and engagement into my work.

Peter I, thanks for initiating the REE free permanent magnet project. I have really enjoyed working with this and it has been very interesting, although I felt the time was short. Thanks for pushing me and making me do more than I thought I was able to.

Ulf, you were only my supervisor in the beginning but an invaluable such.

Anders, Im in such a gratitude depth to you it will be difficult to repay. Thanks for all help and support not only concerning work. I wonder if Sleipnir would exist today without your help.

Thanks Petra for always asking the uncomfortable questions forcing me to really think about things and having to motivate why I have done things the way I have. Thanks for saving the CoFeZr article at the end.

Tom, the most cheerful British guy I know, its been so fun working with you and I have learned so much diffraction stuff from you.

Bengt it is good to have someone who knows what he is doing and great work that we could figure out the composition modulations.

Björgvin thanks for allowing me to work in such a well equipped lab and sharing your insights into things not only related to physics.

Peter S thanks for all the magnetic characterization and the following fruitful discussions, your help was indispensable.

Rimantas, without your etching and sample cutting non of these projects would have even been possible, I am very very thankful.

Thanks all my postdocs, where would I be without you and your knowledge transfer. Martina, my new big sister. Fridrik for getting me on the right track making sure I got the first article out. Heikki my understanding of XRD would be much smaller without our lunch discussions. Spiros it was nice to have someone which understood me when I wanted to discuss physics in terms of electrical engineering and with whom I could indulge in engineering nerdery.

References

[1] Oliver Gutfleisch, Matthew A. Willard, Ekkes Brück, Christina H. Chen, S. G. Sankar, and J. Ping Liu. Magnetic Materials and Devices for the 21st century: Stronger, Lighter, and More Energy Efficient. *Advanced materials*, 23(7):821–42, mar 2011.

[2] SGU. Mineralmarknaden Tema: Specialmetaller. Technical report, Sveriges geologiska undersökning, 2011.

[3] G.B. Haxel, J.B. Hedrick, and G.J. Orris. Rare Earth Elements - Critical Resources for High Technology. *United States Geological Survey Fact Sheet*, 087-02, 2002.

[4] Richard Stone. As China's Rare Earth R&D Becomes Ever More Rarefied, Others Tremble. *Science*, 325(5946):1336–1337, sep 2009.

[5] U.S. DOE. Critical Materials Strategy. Technical report, U.S. Department of Energy, 2011.

[6] SGU. Metallprisutvecklingen. Technical Report 8, Sveriges geologiska undersökningar (SGU), 2015.

[7] Associated Press. China scraps quotas on rare earths after WTO complaint. *The Guardian*, January 5, 2015.

[8] U.S. DOE. Critical Materials Strategy. Technical Report December, U.S. Department of Energy, 2010.

[9] Arjun K. Pathak, Mahmud Khan, Karl A. Gschneidner, Ralph W. McCallum, Lin Zhou, Kewei Sun, Kevin W. Dennis, Chen Zhou, Frederick E. Pinkerton, Matthew J. Kramer, and Vitalij K. Pecharsky. Cerium: An Unlikely Replacement of Dysprosium in High Performance Nd-Fe-B Permanent Magnets. *Advanced Materials*, 27(16):2663–2667, 2015.

[10] J.M.D. Coey. Permanent magnets: Plugging the gap. *Scripta Materialia*, 67(6):524–529, 2012.

[11] Milton Ohring. *Materials Science of Thin Films*. Academic Press, 2 edition, 2002.

[12] James F Ziegler. www.srim.org SRIM - The Stopping and Range of Ions in Matter.

[13] James F Ziegler, J P Biersack, and U Littmark. *The Stopping and Range of Ions in Solids*. Stopping and ranges of ions in matter. Pergamon, 1985.

[14] John F O'Hanlon. *A User's Guide to Vacuum Technology*. John Wiley & Sons, Hoboken, 3 edition, 2003.

[15] Erik Särhammar, Erik Strandberg, Nicolas Martin, and Tomas Nyberg. Sputter rate distribution and compositional variations in films sputtered from elemental and multi-element targets at different pressures. *International Journal of Materials Science and Applications*, 3(2):29–36, 2014.

[16] Erik Särhammar, E Strandberg, J Sundberg, H Nyberg, T Kubart, S Jacobson, U Jansson, and T Nyberg. Mechanisms for compositional variations of

coatings sputtered from a WS2 target. *Surface & Coatings Technology*, 252:186–190, 2014.

[17] Simon Foner. Versatile and sensitive vibrating-sample magnetometer. *Review of Scientific Instruments*, 30(7):548–557, 1959.

[18] Z. Q. Qiu and S. D. Bader. Surface magneto-optic Kerr effect. *Review of Scientific Instruments*, 71(3):1243, 2000.

[19] J.M.D. Coey. *Magnetism and Magnetic Materials*. Cambridge University Press, 2009.

[20] R. Skomski and J.M.D. Coey. Magnetic anisotropy - How much is enough for a permanent magnet? *Scripta Materialia*, 112:3–8, 2015.

[21] J.M.D. Coey. Advances in Magnetics Hard Magnetic Materials: A Perspective. *IEEE Transactions on Magnetics*, 47(12):4671–4681, 2011.

[22] M. J. Kramer, R. W. McCallum, I. A. Anderson, and S. Constantinides. Prospects for Non-Rare Earth Permanent Magnets for Traction Motors and Generators. *JOM*, 64(7):752–763, jun 2012.

[23] Arjun K. Pathak, M. Khan, K.A. Gschneidner, R.W. McCallum, L. Zhou, K. Sun, M.J. Kramer, and V.K. Pecharsky. Magnetic properties of bulk, and rapidly solidified nanostructured $(Nd_{1-x}Ce_x)_2Fe_{14-y}Co_yB$ ribbons. *Acta Materialia*, 103:211–216, 2016.

[24] Lin Zhou, M. K. Miller, Ping Lu, Liqin Ke, R. Skomski, H. Dillon, Q. Xing, A. Palasyuk, M. R. McCartney, D. J. Smith, S. Constantinides, R. W. McCallum, I. E. Anderson, V. Antropov, and M. J. Kramer. Architecture and magnetism of alnico. *Acta Materialia*, 74:224–233, 2014.

[25] Till Burkert, Lars Nordström, Olle Eriksson, and Olle Heinonen. Giant Magnetic Anisotropy in Tetragonal FeCo Alloys. *Physical Review Letters*, 93(2):027203, 2004.

[26] E. K. Delczeg-Czirjak, Alexander Edström, M. Werwiński, Jan Rusz, N. V. Skorodumova, L. Vitos, and Olle Eriksson. Stabilization of the tetragonal distortion of Fe_xCo_{1-x} alloys by C impurities: A potential new permanent magnet. *Physical Review B*, 89(14):144403, 2014.

[27] Anurag Chaturvedi, Rumana Yaqub, and Ian Baker. A comparison of τ-MnAl particulates produced via different routes. *Journal of Physics: Condensed Matter*, 26(6):064201, 2014.

[28] T. Mix, K.-H. Müller, L. Schultz, and T.G. Woodcock. Formation and magnetic properties of the $L1_0$ phase in bulk, powder and hot compacted Mn–Ga alloys. *Journal of Magnetism and Magnetic Materials*, 391:89–95, 2015.

[29] T. Mix, K. Bittner, K. Müller, L. Schultz, and T. G. Woodcock. Phase formation and stability of the $L1_0$ phase in the Mn-Al-Ga system. In *13th Joint MMM-Intermag Conference*, pages DH–04, 2016.

[30] R.W. McCallum, Laura H. Lewis, R. Skomski, M.J. Kramer, and I.E. Anderson. Practical Aspects of Modern and Future Permanent Magnets. *Annual Review of Materials Research*, 44(1):451–477, 2014.

[31] Alexander Edström, Jonathan Chico, Adam Jakobsson, Anders Bergman, and Jan Rusz. Electronic structure and magnetic properties of $L1_0$ binary alloys. *Physical Review B*, 90(1):014402, 2014.

[32] J Paulevé, A Chamberod, K Krebs, and A Bourret. Magnetization Curves of

FeNi (50–50) Single Crystals Ordered by Neutron Irradiation with an Applied Magnetic Field. *Journal of Applied Physics*, 39(2):989, 1968.

[33] Eric Poirier, Frederick E. Pinkerton, Robert Kubic, Raja K. Mishra, Nina Bordeaux, Arif Mubarok, Laura H. Lewis, Joseph I. Goldstein, Ralph Skomski, and Katayun Barmak. Intrinsic magnetic properties of $L1_0$ FeNi obtained from meteorite NWA 6259. *Journal of Applied Physics*, 117(17):17E318, 2015.

[34] Takayuki Kojima, Misako Ogiwara, Masaki Mizuguchi, Masato Kotsugi, Tomoyuki Koganezawa, Takumi Ohtsuki, Taka-Yuki Tashiro, and Koki Takanashi. Fe-Ni composition dependence of magnetic anisotropy in artificially fabricated $L1_0$-ordered FeNi films. *Journal of Physics: Condensed Matter*, 26:064207, 2014.

[35] Ralph Skomski and J.M.D. Coey. Nitrogen diffusion in Sm2Fe17 and local elastic and magnetic properties. *Journal of Applied Physics*, 73(11):7602, 1993.

[36] Wei Bin Cui, Yukiko K. Takahashi, and Kazuhiro Hono. Nd2Fe14B/FeCo anisotropic nanocomposite films with a large maximum energy product. *Advanced Materials*, 24(48):6530–6535, 2012.

[37] V Neu, S Sawatzki, and M Kopte. Fully Epitaxial, Exchange Coupled SmCo5/Fe Multilayers With Energy Densities above 400 kJ/m3. *IEEE Transactions on Magnetics*, 48(11):3599–3602, 2012.

[38] Balamurugan Balasubramanian, Pinaki Mukherjee, Ralph Skomski, Priyanka Manchanda, Bhaskar Das, and David J Sellmyer. Magnetic nanostructuring and overcoming Brown's paradox to realize extraordinary high-temperature energy products. *Scientific reports*, 4:6265, 2014.

[39] J.M.D. Coey and Hong Sun. Improved magnetic properties by treatment of iron-based rare earth intermetallic compounds in anmonia. *Journal of Magnetism and Magnetic Materials*, 87:251–254, 1990.

[40] J.M.D. Coey. Novel permanent magnetic materials. *Physica Scripta*, T39:21–28, 1991.

[41] J.M.D. Coey and P.A.I. Smith. Magnetic nitrides. *Journal of Magnetism and Magnetic Materials*, 200(March), 1999.

[42] Tetsuji Saito. Magnetic properties of anisotropic Sm-Fe-N bulk magnets produced by spark plasma sintering method. *Journal of Magnetism and Magnetic Materials*, 369:184–188, 2014.

[43] Joon-Chul Yun, Su-Min Yoon, Geon-Yong Lee, Joon-Phil Choi, and Jai-Sung Lee. Microstructure and Magnetic Property of Sm_2Fe_{17} Nanopowder Synthesized by Modified Reduction-Diffusion Process. *Materials Transactions, JIM*, 55(10):1630–1633, 2014.

[44] H. Sepehri-Amin, T. Ohkubo, M. Gruber, T. Schrefl, and K. Hono. Micromagnetic simulations on the grain size dependence of coercivity in anisotropic Nd-Fe-B sintered magnets. *Scripta Materialia*, 89:29–32, 2014.

[45] Satoshi Sugimoto, Michihide Nakamura, Masashi Matsuura, Yasuhiro Une, Hirokazu Kubo, and Masato Sagawa. Enhancement of Coercivity of Nd-Fe-B Ultrafine Powders Comparable to Single Domain Size by the Grain Boundary Diffusion Process. *IEEE Transactions on Magnetics*, 50(1):1–1, 2015.

[46] S. Sugimoto, M. Nakamura, K. Isogai, M. Matsuura, Y. Une, H. Kubo, and M. Sagawa. Recent Progress in High-Performance Magnets. In *Rare Earth*

and Future Permanent Magnets and Their Applications (REPM2014), pages 34–38, 2014.

[47] Satoshi Hirosawa. Current Status of Research and Development toward Permanent Magnets Free from Critical Elements. *Journal of Magnetics Society of Japan*, 2015.

[48] Eckart F Kneller and Reinhard Hawig. The exchange-spring magnet: a new material principle for permanent magnets. *IEEE Transactions on Magnetics*, 27(4):3588–3600, 1991.

[49] Ralph Skomski, Priyanka Manchanda, Pankaj K. Kumar, B. Balamurugan, Arti Kashyap, and D. J. Sellmyer. Predicting the Future of Permanent-Magnet Materials. *IEEE Transactions on Magnetics*, 49(7):3215–3220, jul 2013.

[50] J Cui, J P Choi, G Li, E Polikarpov, J Darsell, N Overman, M Olszta, D Schreiber, M Bowden, and T Droubay. Thermal stability of MnBi magnetic materials. *Journal of Physics: Condensed Matter*, 26(6):064212, 2014.

[51] Tomoyuki Ogawa, Yasunobu Ogata, Ruwan Gallage, Naoya Kobayashi, Naoaki Hayashi, Yoshihiro Kusano, Shinpei Yamamoto, Kaori Kohara, Masaaki Doi, Mikio Takano, and Migaku Takahashi. Challenge to the synthesis of $\alpha"$-Fe$_{16}$N$_2$ compound nanoparticle with high saturation magnetization for rare earth free new permanent magnetic material. *Applied Physics Express*, 6(7), 2013.

[52] Yanfeng Jiang, Xiaowei Zhang, Aminul Al Mehedi, Meiyin Yang, and Jian-Ping Wang. A method to evaluate $\alpha"$-Fe$_{16}$N$_2$ volume ratio in FeN bulk material by XPS. *Materials Research Express*, 2(11):116103, 2015.

[53] MD Kuz'min, KP Skokov, H Jian, I Radulov, and Oliver Gutfleisch. Towards high-performance permanent magnets without rare earths. *Journal of Physics: Condensed Matter*, 26:064205, 2014.

[54] L. Reichel, G. Giannopoulos, S. Kauffmann-Weiss, M. Hoffmann, D. Pohl, Alexander Edström, S. Oswald, D. Niarchos, J. Rusz, L. Schultz, and S. Fähler. Increased magnetocrystalline anisotropy in epitaxial Fe-Co-C thin films with spontaneous strain. *Journal of Applied Physics*, 116(21):213901, 2014.

[55] Michael E McHenry, Matthew a Willard, and David E Laughlin. Amorphous and nanocrystalline materials for applications as soft magnets. *Prog. Mater. Sci.*, 44(4):291–433, 1999.

[56] Mitsuru Ohtake, Akira Itabashi, Fumiyoshi Kirino, and Masaaki Futamoto. L10 ordered FePd, FePt, and CoPt thin films with flat surfaces prepared on MgO(110) single-crystal substrates. *IEEE Transactions on Magnetics*, 49(7):3295–3298, 2013.

[57] Masaaki Futamoto, Masahiro Nakamura, Mitsuru Ohtake, Nobuyuki Inaba, and Teruho Shimotsu. Growth of L 10-ordered crystal in FePt and FePd thin films on MgO(001) substrate. *AIP Advances*, 6(8):085302, 2016.

[58] G. C. Hadjipanayis and R. Madugundo. Bulk Mn-Al-(C) permanent magnets. In *13th Joint MMM-Intermag Conference*, pages DH–02, 2016.

[59] Q. Zeng, I. Baker, J.B. Cui, and Z.C. Yan. Structural and magnetic properties of nanostructured Mn–Al–C magnetic materials. *Journal of Magnetism and Magnetic Materials*, 308(2):214–226, jan 2007.

[60] M Tanaka, J P Harbison, J. DeBoeck, T Sands, B Philips, T L Cheeks, and V G Keramidas. Epitaxial growth of ferromagnetic ultrathin MnGa films with

perpendicular magnetization on GaAs. *Applied Physics Letters*, 62(13):1565, 1993.

[61] Nina Bordeaux, Ana Maria Montes-Arango, J Liu, Katayun Barmak, and Laura H. Lewis. Thermodynamic and kinetic parameters of the chemical order-disorder transformation in $L1_0$ FeNi (tetrataenite). *Acta Materialia*, 103:608–615, 2016.

[62] Seungwon Lee, Kaveh Edalati, Hideaki Iwaoka, Zenji Horita, Takumi Ohtsuki, Takuo Ohkochi, Masato Kotsugi, Takayuki Kojima, Masaki Mizuguchi, and Koki Takanashi. Formation of FeNi with $L1_0$-ordered structure using high-pressure torsion. *Philosophical Magazine Letters*, 94(10):639–646, 2014.

[63] Akihiro Makino, Parmanand Sharma, Kazuhisa Sato, Akira Takeuchi, Yan Zhang, and Kana Takenaka. Artificially produced rare-earth free cosmic magnet. *Scientific Reports*, 5:16627, 2015.

[64] Y. Mishin, M.J. Mehl, and D.a. Papaconstantopoulos. Phase stability in the Fe–Ni system: Investigation by first-principles calculations and atomistic simulations. *Acta Materialia*, 53(15):4029–4041, sep 2005.

[65] Laura H. Lewis, A Mubarok, E Poirier, Nina Bordeaux, P Manchanda, A Kashyap, Ralph Skomski, J Goldstein, F E Pinkerton, R K Mishra, R C Kubic Jr, and K Barmak. Inspired by nature: investigating tetrataenite for permanent magnet applications. *Journal of Physics: Condensed Matter*, 26:064213, 2014.

[66] Masato Kotsugi, Masaki Mizuguchi, Shigeki Sekiya, Masaichiro Mizumaki, Takayuki Kojima, Tetsuya Nakamura, Hitoshi Osawa, Kenji Kodama, Takumi Ohtsuki, Takuo Ohkochi, Koki Takanashi, and Yoshio Watanabe. Origin of strong magnetic anisotropy in $L1_0$-FeNi probed by angular-dependent magnetic circular dichroism. *Journal of Magnetism and Magnetic Materials*, 326:235–239, jan 2013.

[67] L. Néel, J. Pauleve, R. Pauthenet, J. Laugier, and D. Dautreppe. Magnetic Properties of an Iron-Nickel Single Crystal Ordered by Neutron Bombardment. *Journal of Applied Physics*, 35(3):873, 1964.

[68] K.B. Reuter, D.B. Williams, and J.I. Goldstein. Ordering in the Fe-Ni system under electron irradiation. *Metallurgical Transactions A*, 20A(April):711–718, 1989.

[69] Masaki Mizuguchi, S. Sekiya, and Koki Takanashi. Characterization of Cu buffer layers for growth of $L1_0$-FeNi thin films. *Journal of Applied Physics*, 107(9):09A716, 2010.

[70] T. Ohmi, T. Saito, T. Shibata, and T. Nitta. Room-temperature copper metallization for ultralarge-scale integrated circuits by a low kinetic-energy particle process. *Applied Physics Letters*, 52(26):2236, 1988.

[71] I. Hashim, B. Park, and H. A. Atwater. Epitaxial growth of Cu (001) on Si (001): Mechanisms of orientation development and defect morphology. *Applied Physics Letters*, 63(20):2833–2835, 1993.

[72] H. Jiang, T. J. Klemmer, J. A. Barnard, and E. A. Payzant. Epitaxial growth of Cu on Si by magnetron sputtering. *Journal of Vacuum Science & Technology A: Vacuum, Surfaces, and Films*, 16(6):3376, nov 1998.

[73] R. A. Lukaszew, Y. Sheng, C. Uher, and R. Clarke. Smoothening of Cu films grown on Si(001). *Applied Physics Letters*, 76(6):724, 2000.

[74] W. Kreuzpaintner, M. Störmer, D. Lott, D. Solina, and A. Schreyer. Epitaxial growth of nickel on Si(100) by dc magnetron sputtering. *Journal of Applied Physics*, 104(11):114302, 2008.

[75] M. Grundner and H. Jacob. Investigations on hydrophilic and hydrophobic silicon (100) wafer surfaces by X-ray photoelectron and high-resolution electron energy loss-spectroscopy. *Applied Physics A Solids and Surfaces*, 39(2):73–82, feb 1986.

[76] W.A. Zisman. Relation of the Equilibrium Contact Angle to Liquid and Solid Constitution. In *Contact Angle, Wettability, and Adhesion*, volume 43 of *Advances in chemistry series*, chapter 1, pages 1–51. American Chemical Society, Washington D.C., 1964.

[77] Takayuki Kojima, Masaki Mizuguchi, Tomoyuki Koganezawa, Keiichi Osaka, Masato Kotsugi, and Koki Takanashi. Magnetic Anisotropy and Chemical Order of Artificially Synthesized $L1_0$-Ordered FeNi Films on Au–Cu–Ni Buffer Layers. *Japanese Journal of Applied Physics*, 51(1):010204, jan 2012.

[78] L. Vegard. Die Konstitution der Mischkristalle und die Raumfüllung der Atome. *Zeitschrift für Physik*, 5(1):17–26, 1921.

[79] A. Meunier, B. Gilles, and M. Verdier. Cu/Si(001) epitaxial growth: role of the epitaxial silicide formation in the structure and the morphology. *Journal of Crystal Growth*, 275:e1059–e1065, 2005.

[80] C.A.F. Vaz, S.J. Steinmuller, C. Moutafis, J.A.C. Bland, and A.Yu. Babkevich. Structural and morphological characterisation of hybrid Cu/Si(001) structures. *Surface Science*, 601:1377–1383, 2007.

[81] Rosa Alejandra Lukaszew and Roy Clarke. Scaling behavior of (0 0 1) and (1 1 1) Cu surfaces. *Applied Surface Science*, 191:118–122, 2002.

[82] Bernard Dennis Cullity. *Elements of X-ray Diffraction*. Addison-Wesley series in metallurgy and materials. Addison-Wesley Publishing Company, Reading, 2 edition, 1978.

[83] Mario Birkholz. *Thin Film Analysis by X-ray Scattering*. Wiley-VCH, Weinheim, 2006.

[84] Satoshi Sasaki. Numerical Tables of Anomalous Scattering Factors Calculated by the Cromer and Liberman's Method. Technical Report February, High Energy Accelerator Research Organization, Tsukuba, 1989.

[85] P J Brown, A G Fox, E N Maslen, M. A. O'Keefe, and B T M Willis. 6.1. Intensity of diffracted intensities. *International Tables for Crystallography*, C:554–595, 2006.

[86] J. Crangle and G.C. Hallam. The magnetization of face-centred cubic and body-centred cubic iron+nickel alloys. *Proceedings of the Royal Society of London A*, 272:119–132, 1963.

[87] Yoshio Miura, Sho Ozaki, Yasushi Kuwahara, Masahito Tsujikawa, Kazutaka Abe, and Masafumi Shirai. The origin of perpendicular magneto-crystalline anisotropy in $L1_0$-FeNi under tetragonal distortion. *Journal of Physics: Condensed Matter*, 25:106005, 2013.

[88] D. Spišák and J. Hafner. Structure and magnetism of gamma-Fe overlayers on face-centered-cubic Co(001) substrates. *Physical Review B - Condensed Matter and Materials Physics*, 62(14):9575–9585, 2000.

[89] S. Andrieu, F. Lahatra Razafindramisa, E. Snoeck, H. Renevier, A. Barbara,

J. M. Tonnerre, M. Brunel, and M. Piecuch. Bct to bcc iron in (001) FeIr superlattices: Relation between structure and magnetism. *Physical Review B*, 52(14):9938–9954, 1995.

[90] V. L. Moruzzi, P. M. Marcus, and J. Kübler. Magnetovolume instabilities and ferromagnetism versus antiferromagnetism in bulk fcc iron and manganese. *Physical Review B*, 39(10):6957–6961, 1989.

[91] Takayuki Kojima, Masaki Mizuguchi, and Koki Takanashi. Significant surface flattening effect by Au addition for Cu growth on $Cu_3Au(001)$. *Surface Science*, 619:44–48, 2014.

[92] P. D. Kirsch and J. G. Ekerdt. Chemical and thermal reduction of thin films of copper (II) oxide and copper (I) oxide. *Journal of Applied Physics*, 90(8):4256–4264, 2001.

[93] Welyson T S Ramos, Thiago H R Cunha, Ingrid D Barcelos, Douglas R Miquita, Gustavo A Ferrari, Sergio de Oliveira, Luciana M Seara, Eliel G Silva Neto, Andre S Ferlauto, and Rodrigo G Lacerda. The role of hydrogen partial pressure on the annealing of copper substrates for graphene CVD synthesis. *Materials Research Express*, 3(4):45602, 2016.

[94] Thomas Gebhardt, Denis Music, Tetsuya Takahashi, and Jochen M. Schneider. Combinatorial thin film materials science: From alloy discovery and optimization to alloy design. *Thin Solid Films*, 520(17):5491–5499, jun 2012.

[95] Ichiro Takeuchi, Jochen Lauterbach, and Michael J. Fasolka. Combinatorial materials synthesis. *Materials Today*, (October):18–26, 2005.

[96] Fang Mao, Tomas Nyberg, Thomas Thersleff, Anna M. Andersson, and Ulf Jansson. Combinatorial magnetron sputtering of AgFeO2 thin films with the delafossite structure. *Materials and Design*, 91:132–142, 2016.

[97] Erik Unosson, Daniel Rodriguez, Ken Welch, and Håkan Engqvist. Reactive combinatorial synthesis and characterization of a gradient Ag-Ti oxide thin film with antibacterial properties. *Acta biomaterialia*, oct 2014.

[98] P.T. Korelis, A. Liebig, M. Björck, B. Hjörvarsson, H. Lidbaum, K. Leifer, and A.R. Wildes. Highly amorphous Fe90Zr10 thin films, and the influence of crystallites on the magnetism. *Thin Solid Films*, 519(1):404–409, oct 2010.

[99] Matej Mayer. SIMNRA User's Guide. Technical Report IPP 9/113, Max-Planck-Instiut für Plasmaphysik, Graching, 1997.

[100] S.R. Elliott. *Physics of Amorphous Materials*. Longman Group Ltd, London and New York, 1984.

[101] V. G. Harris, K. D. Aylesworth, B. N. Das, W. T. Elam, and N. C. Koon. Structural origins of magnetic anisotropy in sputtered amorphous Tb-Fe films. *Physical Review Letters*, 69(13):1939–1942, 1992.

Appendix A.
MATLAB script for simulation of compositions and thicknesses from combinatorial sputtering in Sleipnir

This matlab code calculates the compositions and thicknesses on a combinatorial sample deposited in Sleipnir. It calculates in points either on a 3 inch wafer or in a square pattern, and the option is set by `cyl=1` or `cyl=0`. For both options it plots a 3D surface plot for each element of one layer in the sample, and which layer to plot is set by `layertoplot`. For the cylindrical option, the variable `beta_offset` is the main diagonal which is used as reference. The cylindrical option also plots composition and thickness along a specified diagonal on the surface, where the angle given by `plotangle` is at the positive value of the radius. Some optional parts, such as comparison to measured values or different plot settings have been commented out. `Combinatorial.m` is the main file to run. `Combinatorial.m` will make calls to the files `magnetron_settings.m`, `sample_settings.m`, and also `rate4magnetron.m`. The first two files contain the settings for the magnetrons and for the sample respectively. In `magnetron_settings.m` two examples are given but more material systems can be added in the file. In `sample_settings.m` two examples of samples are given for a 3-layer sample, where the second layer has a ternary composition gradient of Co-Fe-Zr. More samples can be included in each sample settings file. `rate4magnetron.m` is called by the calculations. If the code is to be adopted for another chamber the geometry in `rate4magnetron.m` needs to be changed.

Combinatorial.m

```
%Script which calculates composition and thickness in a
    combinatorial sputtered sample using the sputter system
    Sleipnir.
%The calculations and definitions of variables are done
    according to
%PhD thesis of Andreas Frisk, 2016,
%"The Importance of Controlling Composition to Tailor the
    Properties of Magnetic Thin Films"
```

```matlab
%Calibration measurements needs to be done at the center of the
    chamber, these values should be entered into phi_meas

clear all;
close all;

setup='CoFeZr';
samplename='Co63Fe27Zr10';

%For Comparison to experimentaldata
%rbspath='path to your RBS data e.g. ..\MATLAB\RBS\CoFeZr';
%XRRpath='path to your XRR data e.g. ..\MATLAB\XRR\CoFeZr';

%%%%%%%%%%%%%%%%%%%%%%%%%%%%%%%%%%%%%%%%%%%%%%%%%%%%%%%%%%%%%%%%%%
%Loading information about magnetrons and elements
[elements, atomic_density, phi_meas_at, n]=magnetron_settings(
    setup);
%%%%%%%%%%%%%%%%%%%%%%%%%%%%%%%%%%%%%%%%%%%%%%%%%%%%%%%%%%%%%%%%%%

%%%%%%%%%%%%%%%%%%%%%%%%%%%%%%%%%%%%%%%%%%%%%%%%%%%%%%%%%%%%%%%%%%
%Loading sputtering parameters, powers and times for this
    sample
[layername, t_sputter, power, rotation, manip_offset]=
    sample_settings(samplename);
%%%%%%%%%%%%%%%%%%%%%%%%%%%%%%%%%%%%%%%%%%%%%%%%%%%%%%%%%%%%%%%%%%

%%
%%%%%%%%%%%%%%%%%%%%%%%%%%%%%%%%%%%%%%%%%%%%%%%%%%%%%%%%%%%%%%%%%%
%Defining points and coordinates where calculations should be
    performed,
%either cylindrical (cyl=1) or linear grid (cyl=0)
cyl=1;
%%%%%%%%%%%%%%%%%%%%%%%%%%%%%%%%%%%%%%%%%%%%%%%%%%%%%%%%%%%%%%%%%%
if cyl == 1 %Calculate for cylindrical or linear coordinate
    system
    %%%%%%%%%%%%%%%%%%%%%%%%%%%%%%%%%%%%%%%%%%%%%%%%%%%%%%%%%%%%%%
    %Defining points in cylindrical coordinates on substrate
    %Performing calculate for full rotation
    %beta is the rotation angle of the substrate
    %r is the radius
    %%%%%%%%%%%%%%%%%%%%%%%%%%%%%%%%%%%%%%%%%%%%%%%%%%%%%%%%%%%%%%
    %Change these values if you want other spacings
    radialpoints=20;
    beta_offset=135; %Start angle, magnetron2 is at 135
    rotationpoints=18; %Number of anglular points, will be
    twice this number of angles
    %%%%%%%%%%%%%%%%%%%%%%%%%%%%%%%%%%%%%%%%%%%%%%%%%%%%%%%%%%%%%%

    r0=38.1; %Radius of a 3" wafer
    r=linspace(0.1, r0, radialpoints)';
```

```
%r_dia vector used for plotting along the diameter of the
wafer
r_dia=[flipud(r); -r];

beta=linspace(0, (180-(180/rotationpoints)), rotationpoints
); %First half turn
beta=[beta, linspace(180, (360-(180/rotationpoints)),
rotationpoints)]; %adding second half turn
beta=beta+beta_offset;
delta_beta=beta(2)-beta(1);
rotmat=[cosd(beta_offset), sind(beta_offset);
        -sind(beta_offset), cosd(beta_offset)];

%Looping through all layers
for l=1:length(layername)
    figure;
    hold on;
    for m=1:length(beta)
        for k=1:length(r)
            Op{k,m,l}=[r(k)*cosd(beta(m)), r(k)*sind(beta(m
)), 0]+manip_offset(l,:);
            Opx(k,m,l)=Op{k,m,l}(1);
            Opy(k,m,l)=Op{k,m,l}(2);
            Opz(k,m,l)=Op{k,m,l}(3);
            plot(Op{k,m,l}(1),Op{k,m,l}(2), '*');

%Calc. coordinates in the coordinate system of the wafer.
            Opsam{k,m}=[(rotmat*Op{k,m,l}(1:2)')', Op{k,m,l
}(3)];
            Opxsam(k,m,l)=Opsam{k,m}(1);
            Opysam(k,m,l)=Opsam{k,m}(2);
            Opzsam(k,m,l)=Opsam{k,m}(3);
        end
    end
    hand=plot(Op{end,1,l}(1), Op{end,1,l}(2), 'ko', '
MarkerSize', 10);
    legend(hand, 'Start angle');
    xlabel('x (mm)');
    ylabel('y (mm)');
    title(['Calculation points, layer: ', layername{l}], '
Interpreter', 'none');
end
else
%%%%%%%%%%%%%%%%%%%%%%%%%%%%%%%%%%%%%%%%%%%%%%%%%%%%%%%%%%%%%%
%Defining coordinates for points in a square lattice
%covering the substrate
%%%%%%%%%%%%%%%%%%%%%%%%%%%%%%%%%%%%%%%%%%%%%%%%%%%%%%%%%%%%%%
%Change these values if you want other spacings
steplength=5;
sidelength=40;
%%%%%%%%%%%%%%%%%%%%%%%%%%%%%%%%%%%%%%%%%%%%%%%%%%%%%%%%%%%%%%
```

114

```matlab
    r0=38.1; %Radius of a 3" wafer
    x=[-sidelength:steplength:sidelength];
    y=[-sidelength:steplength:sidelength]';
    %Can't do rotation in this geometry
    rotation=zeros(size(rotation));

    %Looping through all layers
    for l=1:length(layername)
        figure;
        hold on;
        for m=1:length(x)
            for k=1:length(y)
                Op{k,m,l}=[x(k), y(m), 0]+manip_offset(l,:);
                Opx(k,m,l)=Op{k,m,l}(1);
                Opy(k,m,l)=Op{k,m,l}(2);
                Opz(k,m,l)=Op{k,m,l}(3);
                plot(Op{k,m,l}(1),Op{k,m,l}(2), '*');
            end
        end
        ang=0:0.01:2*pi;
        hand=plot(manip_offset(l,1)+r0*cos(ang),manip_offset(l
    ,2)+r0*sin(ang), 'k', 'LineWidth', 2);
        legend(hand, 'Sample');
        xlabel('x (mm)');
        ylabel('y (mm)');
        title(['Calculation points, layer: ', layername{l}], '
    Interpreter', 'none');
    end
end

%%
%%%%%%%%%%%%%%%%%%%%%%%%%%%%%%%%%%%%%%%%%%%%%%%%%%%%%%%%%%%%%
%Calculate final rates, concentarations and thicknesses for
    each layer
%%%%%%%%%%%%%%%%%%%%%%%%%%%%%%%%%%%%%%%%%%%%%%%%%%%%%%%%%%%%%
thickness_tot=zeros(size(Op(:,:,1)));
%Need a matrix of densites for each point and each element to
    calculate thickness inside the loop
atomic_density_3D=ones(1,1,4);
atomic_density_3D(1,1,:)=atomic_density;
atomic_density_3D=repmat(atomic_density_3D, [size(Op(:,:,1))
    ,1]);

%%%%%%%%%%%%%%%%%%%%%%%%%%%%%%%%%%%%%%%%%%%%%%%%%%%%%%%%%%%%%
%Looping through all layers
for l=1:length(layername)

    %Loop through all elements
    for k=1:4
```

```matlab
    %Calculate the rate deviations phi_p for each element
and all points
    phi_p{l,k}=rate4magnetron(k, n, Op(:,:,l),phi_meas_at);

    %Calculate rate, third dimension (k) in matrixes is for
each element
    if power(l,k)
        rate{l}(:,:,k)=(phi_p{l,k}{1}.*repmat(power(l,k),
size(Op(:,:,l))))+phi_p{l,k}{2});
    else
        %If the power is 0, the magnetron was turned of and
rate should be 0
        rate{l}(:,:,k)=zeros(size(Op(:,:,l)));
    end
end

%If layer is rotated the concentration and thickness should
be integrated for each radius
if rotation(l)
    %Numerical integration
    rate_rotavg{l}=sum(rate{l}.*repmat(r,1,length(beta),4)
.*delta_beta,2)./(360*repmat(r,1,1,4));
    rate_rotavg{l}=repmat(rate_rotavg{l},1,length(beta),1);
    %Summing rates for all elements (3 is along third
dimension)
    rate_tot{l}=sum(rate_rotavg{l},3);
    %Concentration for all four elements
    conc{l}=rate_rotavg{l}./repmat(rate_tot{l},1,1,4);
    thickness{l}=t_sputter(l)*(rate_tot{l}.^2)./sum(
atomic_density_3D.*rate_rotavg{l}, 3);

%No rotation the conc and thickness is the sum for each
point
else
    %Summing rates for all elements (3 is along third
dimension)
    rate_tot{l}=sum(rate{l},3);
    %Concentration for all four elements
    conc{l}=rate{l}./repmat(rate_tot{l},1,1,4);
    thickness{l}=t_sputter(l)*(rate_tot{l}.^2)./sum(
atomic_density_3D.*rate{l}, 3);
end
thickness_tot=thickness_tot+thickness{l};

%Create vectors which span the enitre diamater of the wafer
if cyl == 1
    conc_dia{l}=[flipud(conc{l}(:,1:length(beta)/2,:));
conc{l}(:,((length(beta)/2)+1):end,:)];
    thick_dia{l}=[flipud(thickness{l}(:,1:length(beta)/2,:)
); thickness{l}(:,((length(beta)/2)+1):end,:)];
end
```

```
end
%Create vector which span the enitre diamater of the wafer
if cyl ==1
    thick_tot_dia =[flipud(thickness_tot(:,1:length(beta)/2,:));
     thickness_tot(:,((length(beta)/2)+1):end,:)];
end
%%%%%%%%%%%%%%%%%%%%%%%%%%%%%%%%%%%%%%%%%%%%%%%%%%%%%%%%%%%%%%%%%%%

%Save data
%%%%%%%%%%%%%%%%%%%%%%%%%%%%%%%%%%%%%%%%%%%%%%%%%%%%%%%%%%%%%%%%%%%
if cyl == 1
    save([samplename '_calculations_cyl.mat']);
else
    save([samplename '_calculations_lin.mat']);
end
%%%%%%%%%%%%%%%%%%%%%%%%%%%%%%%%%%%%%%%%%%%%%%%%%%%%%%%%%%%%%%%%%%%

%%
%Ploting data
%%%%%%%%%%%%%%%%%%%%%%%%%%%%%%%%%%%%%%%%%%%%%%%%%%%%%%%%%%%%%%%%%%%
%Change plotangle if you want to plot along another diagonal
plotangle =1;
cmp=lines(length(layername)+1);
plotlinestyle ={':', '-', '--', '-.'};

%Line plots only in cylindrical coordinates
if cyl == 1
%%%%%%%%%%%%%%%%%%%%%%%%%%%%%%%%%%%%%%%%%%%%%%%%%%%%%%%%%%%%%%%%%%%
%Thickness
    figure; hold on;
    for l=1:length(layername);
        thand(l)=plot(r_dia, thick_dia{l}(:,plotangle));
        thand(l).Color=cmp(l,:);
    end
    thand(l+1)=plot(r_dia, thick_tot_dia(:,plotangle));
    thand(l+1).Color=cmp(l+1,:);
    legend(thand, [layername, 'Total'], 'Interpreter', 'none',
    'location', 'Best');

    %Comparison to experimental data
    %{
    load([XRRpath 'yourfilename.mat'], 'sampleposition', 'd', '
    d_err')
    texphand=errorbar((sampleposition -38.1), d, d_err, 'k*'); %
    Sample pos x=0 is at -38 for CoFeZr
    legend([thand, texphand], [layername, 'Total', 'Measured'],
     'Interpreter', 'none', 'location', 'Best', 'FontSize', 12)
    ;
    %}

    set(gcf, 'PaperPosition', [0 0 17.2 17.2/1.618]);
```

```
set(gcf, 'PaperSize', [17.2  17.2/1.618]);
set(gca, 'LineWidth', 1, 'FontSize', 14);
set(thand, 'LineWidth', 2);
box on;
xlabel('Radius_(mm)');
ylabel(['Thickness_(' char(197) ')']);
title(['Positive_radius_at_\beta_=_', num2str(beta(
plotangle)), '\circ._', elements{1}, '_target_at_-45\circ'
]);
saveas(gcf,[samplename, '_thickness_at_' num2str(beta(
plotangle),3) '.fig']);
saveas(gcf,[samplename, '_thickness_at_' num2str(beta(
plotangle),3)], 'pdf');

%%%%%%%%%%%%%%%%%%%%%%%%%%%%%%%%%%%%%%%%%%%%%%%%%%%%%%%%%%%%%%%%%%%%%%%%%%%%
%Composition
figure; hold on;
m=1;
for l=1:length(layername);
    for k=1:4;
        if power(l,k) %Only plot if this target is used
            chand(m)=plot(r_dia, conc_dia{l}(:, plotangle,k)
);
            chand(m).Color=cmp(k,:);
            %chand(l).Color=cmp(l,:);
            chand(m).LineStyle=plotlinestyle{mod(l,numel(
plotlinestyle))+1};
            legendnames{m}=[layername{l} ':_' elements{k}];
            m=m+1;
        end
    end
end
legend([chand], [legendnames], 'Interpreter', 'none', '
location', 'Best', 'FontSize', 12);

%Comparison to RBS data
%CoFeZr
%{
expdata=load([rbspath 'yourfilename.mat'], 'new_conc', '
realsampleposition', 'elements');
cexphand=plot(expdata.realsampleposition-38.1, expdata.
new_conc(:,1:3), '*', 'MarkerSize', 10);
cexphand(1).Color=cmp(1,:);
cexphand(2).Color=cmp(3,:);
cexphand(3).Color=cmp(4,:);
legend([chand, cexphand'], [legendnames, 'Meas._Fe', 'Meas.
_Co', 'Meas._Zr'], 'Interpreter', 'none', 'location', 'Best
');
%}

set(gcf, 'PaperPosition', [0 0 17.2  17.2/1.618]);
```

```matlab
    set(gcf, 'PaperSize', [17.2 17.2/1.618]);
    set(gca, 'LineWidth', 1, 'FontSize', 14);
    set(chand, 'LineWidth', 2);
    box on;
    xlabel('Radius_(mm)');
    ylabel('Composition_(at.%)');
    title(['Positive_radius_at_\beta_=_', num2str(beta(
    plotangle)), '\circ._', elements{1}, '_target_at_-45\circ'
    ]);
    saveas(gcf,[samplename, '_composition_at_' num2str(beta(
    plotangle),3) '.fig']);
    saveas(gcf,[samplename, '_composition_at_' num2str(beta(
    plotangle),3)], 'pdf');
end

%%
%%{
%Composition 3D surface plot for one layer
%%%%%%%%%%%%%%%%%%%%%%%%%%%%%%%%%%%%%%%%%%%%%%%%%%%%%%%%%%%%%
%Change number if you want to plot another layer
layertoplot=1;

figure; hold on;
m=1;
for l=layertoplot;
    for k=1:4;
        if power(l,k) %Only plot if this target is used
        c3Dhand(m)=surf(Opx(:,:,l), Opy(:,:,l), conc{l}(:,:,k))
    ;
        legendnames3D{m}=[layername{l} ':_' elements{k}];
        m=m+1;
        end
    end
    ang=0:0.01:2*pi;
    hand=plot3(manip_offset(l,1)+r0*cos(ang), manip_offset(l,2)+
    r0*sin(ang), ones(length(ang)), 'k', 'LineWidth', 2);
end

set(gcf, 'PaperPosition', [0 0 17.2 17.2/1.618]);
set(gxf, 'PaperSize', [17.2 17.2/1.618]);
set(gca, 'LineWidth', 1, 'FontSize', 14);
box on;
view(-45, 10);
xlabel('{\itx}_(mm)');
ylabel('{\ity}_(mm)');
zlabel('Composition_(at.%)');
legend([c3Dhand], [legendnames3D], 'Interpreter', 'none', '
    location', 'Best');
if cyl == 1
    saveas(gcf,[samplename, '_composition_3D_cyl.fig']);
    saveas(gcf,[samplename, '_composition_3D_cyl'], 'pdf');
```

```
else
    saveas(gcf,[samplename, '_composition_3D_lin.fig']);
    saveas(gcf,[samplename, '_composition_3D_lin'], 'pdf');
end
%}
%%
%%{
%Contour plot in sample coordinates, of one layer, one element
%%%%%%%%%%%%%%%%%%%%%%%%%%%%%%%%%%%%%%%%%%%%%%%%%%%%%%%%%%%%%%%%%%%%%%
if cyl == 1 %Only implemented for cyl calculations
%Change to other number if you want to plot another layer
    layertoplot=2;
%Change to other number if you want to plot another element
    elementoplot=4;
%Change for other number of contours
    noocontours=20;

figure; hold on;
l=layertoplot;
k=elementoplot;
[conthandC, conthandH]=contour(Opxsam(:,:,l), Opysam(:,:,l),
    100*conc{l}(:,:,k), noocontours, 'ShowText', 'on');
xlim([-38,38]);
ylim([-38,38]);
set(gcf, 'PaperPosition', [0 0 17.2 0.9*17.2]);
set(gcf, 'PaperSize', [17.2 0.9*17.2]);
set(gca, 'LineWidth', 1, 'FontSize', 14);
box on;
xlabel('{\itx}_{sample}_(mm)');
ylabel('{\ity}_{sample}_(mm)');
title(['Composition_of_' elements{k}, '_(at.%)']);
saveas(gcf,[samplename, '_' elements{k} '_compo_cont.fig']);
saveas(gcf,[samplename, '_' elements{k} '_compo_cont'], 'pdf');
end
%}
```

magnetron_settings.m

```
%File with settings for a specific setup of the sputtering
    chamber
%The calculations and definitions of variables are done
    according to
%PhD thesis of Andreas Frisk, 2016,
%"The Importance of Controlling Composition to Tailor the
    Properties of Magnetic Thin Films"

%Information about magnetrons and elements
%%%%%%%%%%%%%%%%%%%%%%%%%%%%%%%%%%%%%%%%%%%%%%%%%%%%%%%%%%%%%%%%%%%%%%
```

120

```matlab
function [elements, atomic_density, phi_meas_at, n]=
    magnetron_settings(setup)
switch setup
    case 'TbCo'
%%%%%%%%%%%%%%%%%%%%%%%%%%%%%%%%%%%%%%%%%%%%%%%%%%%%%%%%%%%%%%%%%%%%%%%%
        elements={'Tb', 'AlZr', 'Co', 'Fe'};
        %Measured deposition rate, at the focus point
        %first column power dependent part [AA/s/W],
        %second column constant offset part [AA/s]
        phi_meas=[0.0208,  0.0517; %Magnetron 1 Tb
                  0.0107,  0.0083; %Magnetron 2 AlZr
                  0.0101, -0.0167; %Magnetron 3 Co
                  0.0062,  0];     %Magnetron 4 Fe

        density=[8.23,  %Density of Tb [g/cm3]
                 1,     %Density of AlZr
                 8.90,  %Density of Co
                 7.874];%Density of Fe

        atomic_weight=[158.925,  %atomic weight of Tb [g/mole]
                       1,        %atomic weight of AlZr
                       58.933,   %atomic weight of Co
                       55.845]; %atomic weight of Fe
        avogrado=6.0221*10^23;
        atomic_density=avogrado*(10^-8)^3*density./
   atomic_weight; %[atoms/AA^3]
        phi_meas_at=phi_meas.*repmat(atomic_density,1,2); %[
   atoms/(s*AA^2)]

        %Parameter describing the angular distribution of the
        %magnetron flux for each magnetron,
        %larger number = more narrow distribution
        n=[2,  %Magnetron 1 Tb
           2,  %Magnetron 2 AlZr
           2,  %Magnetron 3 Co
           2]; %Magnetron 4 Fe
%%%%%%%%%%%%%%%%%%%%%%%%%%%%%%%%%%%%%%%%%%%%%%%%%%%%%%%%%%%%%%%%%%%%%%%%

    case 'CoFeZr'
%%%%%%%%%%%%%%%%%%%%%%%%%%%%%%%%%%%%%%%%%%%%%%%%%%%%%%%%%%%%%%%%%%%%%%%%
        elements={'Fe', 'Al', 'Co', 'Zr'};
        %Measured deposition rate, at the focus point
        %first column power dependent part [AA/s/W],
        %second column constant offset part [AA/s]
        phi_meas=[0.0051,  0.0837; %Magnetron 1 Fe
                  0.0081,  0.0741; %Magnetron 2 Al
                  0.0063,  0.1676; %Magnetron 3 Co
                  0.0109, -0.0141]; %Magnetron 4 Zr

        density=[7.874, %Density of Fe [g/cm3]
                 2.7,   %Density of Al
```

```
                    8.90,    %Density of Co
                    6.511]; %Density of Zr

        atomic_weight=[55.845,   %atomic weight of Fe [g/mole]
                       26.982,   %atomic weight of Al
                       58.933,   %atomic weight of Co
                       91.224]; %atomic weight of Zr
        avogrado=6.0221*10^23;
        atomic_density=avogrado*(10^-8)^3*density./
    atomic_weight; %[atoms/AA^3]
        phi_meas_at=phi_meas.*repmat(atomic_density,1,2); %[
    atoms/(s*AA^2)]

        %Parameter describing the angular distribution of the
        %magnetron flux for each magnetron,
        %larger number = more narrow distribution
        n=[2,    %Magnetron 1 Fe
           2,    %Magnetron 2 Al
           2,    %Magnetron 3 Co
           2];   %Magnetron 4 Zr
%%%%%%%%%%%%%%%%%%%%%%%%%%%%%%%%%%%%%%%%%%%%%%%%%%%%%%%%%%%%%

%More setups can be added as new cases in similar way

end
end
```

sample_settings.m

```
%File with settings used for a specific sample

%The calculations and definitions of variables are done
    according to
%PhD thesis of Andreas Frisk, 2016,
%"The Importance of Controlling Composition to Tailor the
    Properties of Magnetic Thin Films"

%%%%%%%%%%%%%%%%%%%%%%%%%%%%%%%%%%%%%%%%%%%%%%%%%%%%%%%%%%%%%
function [layername, t_sputter, power, rotation, manip_offset]=
    sample_settings(samplename)

%Sputtering parameters Powers and times
%%%%%%%%%%%%%%%%%%%%%%%%%%%%%%%%%%%%%%%%%%%%%%%%%%%%%%%%%%%%%
%For each layer l:
%power(l,:)=[Magnetron1, Magnetron2, Magnetron3, Magnetron4] (
    in Watt)
%t_sputter(l)= Deposition time in secons of layer n
%rotation(l)=1, rotation during deposition of layer n
%rotation(l)=0, no rotation during deposition of layer n
```

```matlab
%manip_offset=[x, y, z]; Offset of the manipulator from the
    center (in mm)
switch samplename
%%%%%%%%%%%%%%%%%%%%%%%%%%%%%%%%%%%%%%%%%%%%%%%%%%%%%%%%%%%%%%%%%%%
    case 'Co45Fe45Zr10'
        %1st layer
        %Al70Zr30 Bufferlayer
        layername{1}='AlZr_buff';
        t_sputter(1)=100;
        power(1,:)=[0, 70, 0, 20];
        rotation(1)=1;
        manip_offset(1,:)=[0, 0, 0];
        %Power magnetron2 Al 70W
        %Power magnetron4 Zr 20W

        %2nd layer
        %CoFeZr layer
        layername{2}='CoFeZr';
        t_sputter(2)=887;
        power(2,:)=[41, 0, 31, 5];
        rotation(2)=0;
        manip_offset(2,:)=[0, 0, 0];
        %Power magnetron1 Fe 41W
        %Power magnetron3 Co 31W
        %Power magnetron4 Zr 5W

        %3rd layer
        %Al70Zr30 cap layer
        layername{3}='AlZr_cap';
        t_sputter(3)=38;
        power(3,:)=[0, 70, 0, 20];
        rotation(3)=1;
        manip_offset(3,:)=[0, 0, 0];
        %Power magnetron2 Al 70W
        %Power magnetron4 Zr 20W
%%%%%%%%%%%%%%%%%%%%%%%%%%%%%%%%%%%%%%%%%%%%%%%%%%%%%%%%%%%%%%%%%%%
%%%%%%%%%%%%%%%%%%%%%%%%%%%%%%%%%%%%%%%%%%%%%%%%%%%%%%%%%%%%%%%%%%%
    case 'Co63Fe27Zr10'
        %1st layer
        %Al70Zr30 Bufferlayer
        layername{1}='AlZr_buff';
        t_sputter(1)=100;
        power(1,:)=[0, 70, 0, 20];
        rotation(1)=1;
        manip_offset(1,:)=[0, 0, 0];
        %Power magnetron2 Al 70W
        %Power magnetron4 Zr 20W

        %2nd layer
        %CoFeZr layer
        layername{2}='CoFeZr';
```

```
        t_sputter(2)=887;
        power(2,:)=[24, 0, 43, 5];
        rotation(2)=0;
        manip_offset(2,:)=[0, 0, 0];
        %Power magnetron1 Fe 24W
        %Power magnetron3 Co 43W
        %Power magnetron4 Zr 5W


        %3rd layer
        %Al70Zr30 cap layer
        layername{3}='AlZr_cap';
        t_sputter(3)=38;
        power(3,:)=[0, 70, 0, 20];
        rotation(3)=1;
        manip_offset(3,:)=[0, 0, 0];
        %Power magnetron2 Al 70W
        %Power magnetron4 Zr 20W
%%%%%%%%%%%%%%%%%%%%%%%%%%%%%%%%%%%%%%%%%%%%%%%%%%%%%%%%%%%%%%%
%uncerttest can be used to calculate the positional
% uncertainty of a combinatorial layer
% here with 7.5mm wide strip and
% +/-5mm positional uncertainty along the gradient
%%%%%%%%%%%%%%%%%%%%%%%%%%%%%%%%%%%%%%%%%%%%%%%%%%%%%%%%%%%%%%%
    case 'uncerttest'
        positions={ [0, 0, 0];
                    [7.5*cosd(135-90), 7.5*sind(135-90), 0];
                    [7.5*cosd(135+90), 7.5*sind(135+90), 0];
                    [5*cosd(135), 5*sind(135), 0];
                    [5*cosd(135-180), 5*sind(135-180), 0]};
        layername= {'center', 'perp+', 'perp-', 'para+', 'para-
    '};

        for k=1:length(positions)
        %CoFeZr layer
        %layername{k}='CoFeZr';
        t_sputter(k)=797;
        power(k,:)=[41, 0, 31, 10];
        rotation(k)=0;
        manip_offset(k,:)=positions{k};
        %Power magnetron1 Fe 41W
        %Power magnetron3 Co 31W
        %Power magnetron4 Zr 5W
        end


%%%%%%%%%%%%%%%%%%%%%%%%%%%%%%%%%%%%%%%%%%%%%%%%%%%%%%%%%%%%%%%

%More samples can be added as new cases in similar way

end
end
```

rate4magnetron.m

```
%%%%%%%%%%%%%%%%%%%%%%%%%%%%%%%%%%%%%%%%%%%%%%%%%%%%%%%%%%%%%%
%rate4magnetrons calculates the rate phi from magnetron
%number i at a points Op in the chamber
%If Op is a matrix with where each row is a set
%of coordinates, then rate4magnetron returns a matrix with the
%same number of rows where the first column is the power
%dependent part and the second is the constant part of the rate

%If Op is a cell-array where each cell is a vector with
%coordinates then
%phi is a cellarray with two elements the first is the power
%dependent part and the second is the constant part of
%the rate, where each element is a matrix of the same size
%as Op

%phi_0 is the measured calibarition deposition rates of
%the targets, in the middle of the sample in the middle
%of the chamber (at the focus point),
%first cloumn is the power dependent rate factor,
%second column is constant offset rate factor.
%n is a factor describing the angular spread for the magnetron

%The calculations and definitions of variables are done
    according to
%PhD thesis of Andreas Frisk, 2016,
%"The Importance of Controlling Composition to Tailor the
    Properties of Magnetic Thin Films"

function phi=rate4magnetron(i, n, Op, phi_0)

d=175.138; %Distance target to focus point (in mm)
alpha=38.81; %Angle from sample plane to magnetrons (in deg)
xy=d*sind(alpha)/sqrt(2);
z_M=d*cosd(alpha);
M=[ xy, -xy, -z_M;  %postition of magnetron 1
   -xy, -xy, -z_M;  %postition of magnetron 2
   -xy,  xy, -z_M;  %postition of magnetron 3
    xy,  xy, -z_M]; %postition of magnetron 4

F=[0,0,0]; %Focus point is origin
z_0=[0,0,z_M]; %Z position of magnetrons

r_0=F-M(i,:); %Vector from magnetron i to origin
r_0_norm=norm(r_0);
z_0_norm=norm(z_0);

if iscell(Op)
    %Depostion rate of magnetron at points, column 1 power
    dependentpart col2 constant part
```

```matlab
    phi={zeros(size(Op)),zeros(size(Op))};
    for  l=1:size(Op,1)
        for  k=1:size(Op,2);
            r_p=Op{l,k}-M(i,:);
            r_p_norm=norm(r_p);
            z=[0,  0,  r_p(3)];
            z_norm=norm(z);
            scalefact_nom=(r_0_norm^(3-n(i)))*z_0_norm*(r_p*z')
   *((r_0*r_p')^n(i));
            scalefact_denom=(r_p_norm^(3+n(i)))*z_norm*(r_0*z_0
   ');
            scalefact=scalefact_nom/scalefact_denom;
            phi{1}(l,k)=phi_0(i,1)*scalefact; %[Power dependent
    part, Constant part]
            phi{2}(l,k)=phi_0(i,2)*scalefact; %[Power dependent
    part, Constant part]
        end
    end
elseif ismatrix(Op)
    r_p=zeros(size(Op,1),3); %Vectors from magnetron to each
    point
    phi=zeros(size(Op,1),2);  %Depostion rate of magnetron at
    points, column 1 power dependentpart col2 constant part
    for  k=1:size(Op,1);
        r_p(k,:)=Op(k,:)-M(i,:);
        r_p_norm(k)=norm(r_p(k,:));
        z(k,:)=[0,  0,  r_p(k,3)];
        z_norm(k)=norm(z(k,:));
        scalefact_nom=(r_0_norm^(3-n(i)))*z_0_norm*(r_p(k,:)*z(
   k,:)')*((r_0*r_p(k,:)')^n(i));
        scalefact_denom=(r_p_norm(k)^(3+n(i)))*z_norm(k)*(r_0*
   z_0');
        scalefact=scalefact_nom/scalefact_denom;
        phi(k,:)=phi_0(i,:)*scalefact; %[Power dependent part,
   Constant part]
    end
end

end
```

Acta Universitatis Upsaliensis

Digital Comprehensive Summaries of Uppsala Dissertations
from the Faculty of Science and Technology 1445

Editor: The Dean of the Faculty of Science and Technology

ACTA
UNIVERSITATIS
UPSALIENSIS
UPPSALA
2016